Dissertation

A Search for Lorentz and CPT Violation in the Neutrino Sector of the Standard Model Extension Using the Near Detectors of the Tokai to Kamioka Neutrino Oscillation Experiment

Submitted by

Gary Alexander Clifton

Department of Physics

In partial fulfillment of the requirements

For the Degree of Doctor of Philosophy

Colorado State University

Fort Collins, Colorado

Spring 2016

Doctoral Committee:

Advisor: Walter Toki

Bruce Berger
Richard Eykholt
Alexander Hulpke

Abstract

A Search for Lorentz and CPT Violation in the Neutrino Sector of the Standard Model Extension Using the Near Detectors of the Tokai to Kamioka Neutrino Oscillation Experiment

The Tokai to Kamioka (T2K) neutrino experiment is designed to search for electron neutrino appearance oscillations and muon neutrino disappearance oscillations. While the main physics goals of T2K fall into conventional physics, T2K may be used to search for more exotic physics. One exotic physics analysis that can be performed is a search for Lorentz and CPT symmetry violation (LV and CPTV) through short baseline neutrino oscillations. The theoretical framework which describes these phenomena is the Standard Model Extension (SME).

Due to its off-axis nature, T2K has two near detectors. A search for LV and CPTV is performed in each detector. The search utilizes charged-current inclusive (CC inclusive) neutrino events to search for sidereal variations in the neutrino event rate at each detector. Two methods are developed; the first being a Fast Fourier Transform method to perform a hypothesis test of the data with a set of 10,000 toy Monte-Carlo simulations that do not have any LV signal in them. The second is a binned likelihood fit.

Using three data sets, both analysis methods are consistent with no sidereal variations. One set of data is used to calculate upper limits on combinations of the SME coefficients while the other two are used to constrain the SME coefficients directly. Despite not seeing any indication of LV in the T2K near detectors, the upper limits provided are useful for the theoretical field to continue improving theories which include LV and CPTV.

Acknowledgements

I want to first thank Walter Toki for taking me in as his graduate student and allowing me to perform this non-standard analysis. Additionally, I want to thank him for his cooperation and guidance he has provided me through these years of graduate school. This analysis and the work on the P0D has provided me the opportunity to experience cultures from around the world. The many trips to Japan were always a pleasure despite tight work schedules, finicky detectors, and sometimes plain old failures.

To Alan Kostelecky and Jorge Diaz. The both of you were kind enough to answer my questions about the Standard Model Extension and its predictions for neutrinos. Despite being located in Indiana (and even in Germany for Jorge), the two of you were quick to respond to my inquiries and were always delightful. The numerous LV workshops and conferences I attended at IU were always a fun experience. Bloomington has quite the charm and I enjoyed every minute there.

I want to thank Dan Ruterbories and Erez Reinherz-Aronis who took a particular interest in my analysis. Your help was extremely valuable to me. To Dan, I enjoyed our many conversations together at William Oliver's. To Erez, please continue to work as hard as you do while also keeping in mind the important things in life. Also, send my love to Caroline, Odem, and Geffin.

To my Colorado friends (especially Jason Liu, Ben Gookin, and Cheri Hall), thank you for helping me learn that there is more to life than working all day every day. The many hikes, meals, camping trips, brewery tours, salsa dancing lessons, and laughs we had together during grad school taught me balance, openness, and how to cut loose. I am a better person as a whole because of these experiences.

Last, but certainly not least, I want to send a huge thank you to my family and to my best friends. I moved halfway across the country for school and each of you still maintained an interest in my life. To my friends, it's incredible that we are still such great friends and have grown closer over the years since high school. I am proud to call you my squad and always look forward to whatever shenanigans we decide to partake in. Gary and Susan Clifton, thank you for your love, patience, and understanding even during the holidays when I was unable to come home to Tennessee. Graduate school is a hectic time and it is without a doubt that the two of you anchored me when I was completely lost. Thank you for being awesome parents. Megan Shurina, Daniel Shurina, and Amelia Mae Shurina, it was wonderful to live with you and watch little Amelia grow up. Thank you for that. Megan and Daniel, please continue to expose Amelia Mae to awesome soul and R&B artists. I will take care of the death metal! Amelia Mae, if you are reading this and want to talk to Uncle Alex about his analysis over a beer, you just let me know.

Table of Contents

List of Tables

List of Figures

CHAPTER 1

Introduction to Dissertation

This dissertation is divided into nine chapters. Chapter 2 provides a short history of neutrinos. Theoretical foundations for conventional mass-driven neutrino oscillations and neutrino oscillations in the Standard Model Extension (SME) are derived in chapter 3. The oscillation probabilities in the SME are the underlying theoretical formulas used in searching for Lorentz violation (LV) in the T2K near detectors are provided in chapter 4.

Chapter 5 begins with a detailed description of the T2K neutrino beam, the near detector site, and the far detector site. Next, in chapter 6, the neutrino selection methods for each near detector are described in detail. Following this chapter, systematic uncertainty studies are performed to see how they affect the LV analysis in chapter 7. The details of the T2K LV search are described in the chapter 9. The search consists of using a Fast Fourier Transform method on both near detector samples and using a binned likelihood fit method on the INGRID sample.

The last chapter, chapter 9, reports the results of the each method for each detector sample. A summary of the analysis and the results is provided followed by a brief discussion of future searches. Finally, a conclusion of the entire dissertation is provided.

CHAPTER 2

A Short History of the Neutrino

In 1914, James Chadwick discovered that the electrons emerging from beta decay had a continuous range of energy instead of being single valued [3]. This behavior violated one of the principal ideas in all of physics: energy conservation. Niels Bohr hypothesized that energy may not be conserved in beta decay in order to explain this behavior. Not many physicists at the time (or even today) were willing to give up energy conservation so quickly. One physicist, Wolfgang Pauli, hypothesized that energy conservation was still valid in beta decays and the discrepancy in the electron energy spectrum may be described by another particle. According to Pauli, this hypothesized particle was nearly massless if not entirely and electrically neutral. On December 4, 1930, Pauli wrote a letter to attendees of a nuclear physics conference in Tubingen first hypothesizing the particle [4]. At the time, he referred to it as the neutron. Pauli wrote "I agree that my remedy may seem incredible ...", referring to the properties of the neutrino being nearly massless and electrically neutral. Pauli hypothesized the neutrino in order to explain the continuous energy spectrum of beta decay. He is noted to have said "I have done something no theorist should ever do. I have created a particle that will never be able to be detected." Pauli's neutron would escape from the beta decay, taking away some of the energy from the electron and thus preserving energy conservation. Many physicists at the time were not willing to accept Pauli's neutron as it ran counter to physicists belief that the atom was only composed of electrons and protons.

After Chadwick had discovered the nucleon (the particle we call the neutron today), Pauli stopped using the word "neutron" to describe his hypothetical particle. To differentiate between Chadwick's neutron and Pauli's neutron, Pauli adopted the suggested name of

"neutrino" from Enrico Fermi which means, in Italian, "little neutral one." Enrico Fermi was very intrigued by the neutrino and began to study it in detail.

Fermi decided to take the idea of the neutrino seriously and began developing his theory of beta decay. From his theory, Fermi was able to calculate the energy spectrum of the electrons in beta decay [3] and these calculations agreed with experimental results. Despite these successes, the physics community was still reluctant to believe the neutrino was real. This was evident when a paper written by Fermi titled "Tentative theory of beta rays" was rejected by the journal *Nature* on the basis that it contained "speculations too remote from reality to be of interest to the reader" [3].

Despite the lack of support for the neutrino, Bruno Pontecorvo went on to first propose a decay chain in order to detect the neutrino in an experiment. The decay chain [4]:

$$\nu + {}^{37}\mathrm{Cl} \rightarrow e^{-} + {}^{37}\mathrm{Ar} \tag{2.1}$$

was first used in 1954 to build a detector that could detect neutrinos in this decay chain. Davis built a 4000 liter detector made of carbon tetrachloride [3]. The carbon tetrachloride provided the chlorine atoms needed in the decay chain. An argon atom created in a neutrino interaction would radiate away and ionize the gas producing an electrical signal which could be detected. Davis placed his detector near a small reactor core and waited for enough argon atoms to accumulate. Davis found no signal as his data was consistent with the interactions incurring from cosmic rays in his detector. He was also unable to tell the difference in his data for when the reactor was on and when it was off [3]. Davis decided to build a larger detector and move it to the newer Savannah River reactor in hopes of better obtaining a signal. However, Davis was unable to provide evidence of the neutrino with his larger

detector. It would ultimately be two other physicists, Fred Reines and Clyde Cowan, to provide the first ever evidence of the neutrino.

Reines and Cowan built a detector 12 meters underground and 11 meters from the reactor core at Savannah River. If a neutrino (or antineutrino as we now know) interacts with a proton, an inverse-beta decay reaction can occur. The detector was designed to detect two bursts of gamma rays separated by 5 microseconds. The first burst would occur from a produce positron annihilating with the detector material. The second burst would occur from a delayed capture of a neutron. In 1956, Reines and Cowan found evidence of neutrinos interacting via inverse-beta decay providing the first experimental evidence ever of the neutrino. However, later on, the Reines and Cowan experiment agreed with the one neutrino hypothesis which will be shown later to be incorrect. Despite this, Pauli's neutrino was, in fact, real and both Reines and Cowan received their case of champagne first wagered by Pauli to anyone who could detect the neutrino. Reines was awarded the Nobel Prize in 1995 for his work in neutrino physics.

With the neutrino discovered, the phenomena of parity violation to Fermi's theory of beta decay needed some mathematical revision but the basic ideas remained unchanged [3]. Fermi's theory showed that neutrinos were more likely to interact the higher their energy was. However, this theory implied that interactions could happen with a probability greater than 100% which is illogical. A muon will decay into an electron and two neutrinos by exchanging a W boson. The theory assumed that these two neutrinos were the same. If the neutrinos were indeed the same, then it would be possible for the muon to decay into an electron and a photon. However, in the large data sets of muon decay, this decay channel was never observed experimentally. This suggested the idea that the neutrinos were not the same and gave rise to neutrino flavors; one neutrino associated with the muon and one

neutrino associated with the electron. In 1962, Leon Lederman, Melvin Schwartz, and Jack Steinberger, showed that more than one type of neutrino exists by detecting interactions with the muon neutrino.

The three physicists used an intense beam of protons incident on a beryllium target. A number of pions are produced in this interaction and rapidly decay into muons and neutrinos. A large steel barrier was used to filter out the muons and allowed the neutrinos to pass through downstream where ten tons of aluminum was placed. Over a period of ten days, they detected 51 neutrinos. Every single one of these interactions with the aluminum produced a muon.; none of them produced an electron. It was the first time that a team of scientists had provided experimental evidence that muon neutrinos and electron neutrinos have their own identities [3].

Detection of the neutrino was tantalizing news in the physics community. However, a particle is not the end of the story. If the particle truly exists, then it behaves a certain way depending on its properties. It is these properties that must then be measured in order to believe if what has been detected truly is the particle that was sought after. In the next section, the famous anomalous behavior of the neutrino will be discussed.

2.1. Neutrino Anomalies

Hans Bethe's theory of the *pp* reaction in the sun predicted that the sun should be producing an abundance of neutrinos. To detect these neutrinos, Ray Davis built a 4000 liter detector consisting of cleaning fluid (i.e. chlorine) and placed this detector 6 meters under the ground in order to shield it from any cosmic ray interactions that may be similar to the neutrino signal. However, this detector was unsuccessful in detecting any solar neutrinos largely because the cosmic ray induced backgrounds occurred too often to be able to detect

any signal. It was necessary to place the detector much deeper underground. The detector was moved to the Homestake mine in South Dakota and was increased in size to 400,000 liters of cleaning fluid. A theorist named John Bahcall joined Davis in his search to detect solar neutrinos. Bahcall made careful calculations based of the design of the detector and the Standard Solar Model to predict how many solar neutrinos should be seen. He quoted his calculations in Solar Neutrino Units (SNUs), which were units used to simplify the dialogue when talking about neutrino capture rates on chlorine-37 for neutrinos produced in the sun. One SNU is $10^{-36}s^{-1}$. Bahcall calculated that 7.5 $\pm$3 SNUs would be seen in their detector. However, only 3 SNUs were actually found in the detector.

The disagreement between expectation and observation prompted Davis to drastically improve the detector and the analysis techniques used to detect neutrinos. Despite all the upgrades and cross checks, a decade after their first result was released there was still major tension between what was predicted from the calculations and what was observed. Bahcall stood by his careful calculations and Davis was able to convince a large majority of the physics community that he had nearly perfected his detector. In 1978, Bahcall predicted that they would see 7.5SNU $\pm$1.5 while Davis found 2.2 $\pm$ 0.4 SNUs. This decade of disagreement became known as the solar neutrino anomaly.

The Kamiokande experiment was originally designed to detect proton decay. However, the proton half life is no less than 1.29×10^{34} years, and thus Kamiokande became essentially obsolete for detecting proton decay. They did realize, however, that they were well suited for detecting solar neutrinos. The Kamiokande experiment was a large water Cherenkov detector whose walls were lines with photo-multiplier tubes (PMTs). When a particle, passing through a medium other than vacuum, travels faster than the speed of light in that medium, this produces a ring of light that can be detected with PMTs. As

the energy of the resulting lepton from a solar neutrino interaction on a water molecule is larger than the Cherenkov threshold, Kamiokande could be used to detect solar neutrinos From 1987 to 1995, Kamiokande detected solar neutrinos. In order to enhance the detection of neutrinos, Kamiokande greatly improved their detection capabilities and dedicated themselves to studying neutrinos occurring from interactions in the Earth's atmosphere. With Kamiokande it was possible to know if neutrinos came from interactions occurring from overhead of Japan or if they had travelled through the Earth and arrived at the bottom of the detector. Kamiokande found that there was an unexplained deficit in the ν_μ flux from these atmospheric neutrinos. Also, Kamiokande found the ν_μ flux coming through the Earth was larger than coming from overhead. This became known as the atmospheric neutrino anomaly.

With evidence from several experiments that neutrinos were not behaving as predicted, it became that neutrinos exhibit some new behavior that must be understood in order to solve these anomalies. Strangely enough, the answer had been hypothesized in 1962; some 16 years before the solar neutrino anomaly was first discovered.

2.2. The Birth of Neutrino Oscillations

In 1962, after finding out there was a difference between the ν_μ and ν_e flavors, Pontecorvo suggested that neutrinos may be able to change flavors in flight. This hypothesis was also independently developed by three Japanese theorists: Maki, Nakagawa, and Sakata. It was this suggestion of flavor change (called neutrino oscillations) that was the first attempt to explain the solar neutrino anomaly. If the ν_e that were created in the sun changed their flavor in flight into, say, a ν_μ, then these oscillated neutrinos would pass undetected through Davis' detector and could thus explain the deficit found in Davis' detector. In order for this

oscillation to occur it was explicit in the theory that neutrinos had to have a non-zero mass. However, a non-zero neutrino mass contradicted the predictions of neutrinos in the Standard Model. The Standard Model required neutrinos to be massless particles and thus, neutrino oscillations were largely ignored.

SuperK tested their data for neutrino oscillations. In a remarkable effort, in 1998 SuperK's data agreed extraordinarily well with the oscillation hypothesis.

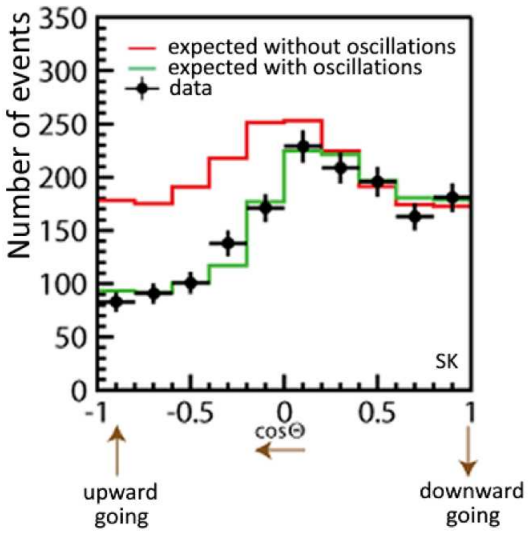

FIGURE 2.1. SuperK data showing the number of neutrino events as a function of cosine of the zenith angle. The SuperK data shows strong agreement with neutrino oscillations.

As for the solar neutrino anomaly, it wasn't until 2003 when the Sudbury Neutrino Observatory (SNO) announced it was 99.999% confident that their data were consistent with neutrino oscillations. For this major discovery, the leaders of the SuperK and SNO experiments, Prof. Kajita and Prof. McDonald, received the 2015 Nobel Prizes in Physics.

With the observation of neutrino oscillations, the solar and atmospheric neutrino anomalies had been solved. Neutrino oscillations provided the first evidence of physics beyond the Standard Model predictions. With this understanding of neutrino oscillations, it is natural to begin working out the quantitative details. This will be done in the next chapter.

CHAPTER 3

Conventional Neutrino Oscillations

This chapter derives the conventional mass-driven neutrino oscillation theory. The neutrino flavor eigenstates are written in terms of the neutrino mass eigenstates and related with a unitary mixing matrix. The mixing matrix is parameterized using three mixing angles and a complex phase factor that may contribute to CP violation. The probability of flavor oscillations is shown and current limits on the different mixing angles and CP phase are provided.

3.1. Neutrino Oscillation Formula

To begin, assume that there exist an arbitrary number of n orthonormal eigenstates. The n flavor eigenstates $|\nu_\alpha\rangle$ with $\langle\nu_\beta|\nu_\alpha\rangle = \delta_{\alpha\beta}$ are connected to the n Hamiltonian eigenstates $|\nu_i\rangle$ with $\langle\nu_i|\nu_j\rangle = \delta_{ij}$ by a unitary mixing matrix U:

$$|\nu_\alpha\rangle = \sum_i U^*_{\alpha i}|\nu_i\rangle \tag{3.1}$$

For non-interacting neutrinos (i.e. in vacuum), the Hamiltonian eigenstates are the mass eigenstates and the mixing matrix is then equated to the PMNS matrix named after Pontecorvo, Maki, Nagasaki, and Sakata. The PMNS matrix may be parameterized with three mixing angles $(\theta_{12}, \theta_{23}, \theta_{13})$ and one complex phase factor that is believed to control CP violation (δ_{CP}). The elements of the PMNS matrix are then, for three flavors,:

$$U^*_{\alpha i} = \begin{pmatrix} 1 & 0 & 0 \\ 0 & c_{23} & s_{23} \\ 0 & -s_{23} & c_{23} \end{pmatrix} \begin{pmatrix} c_{13} & 0 & s_{13}e^{-i\delta_{CP}} \\ 0 & 1 & 0 \\ -s_{13}e^{i\delta_{CP}} & 0 & c_{13} \end{pmatrix} \begin{pmatrix} c_{12} & s_{12} & 0 \\ -s_{12} & c_{12} & 0 \\ 0 & 0 & 1 \end{pmatrix} \tag{3.2}$$

where

$$c_{ij} = \cos\theta_{ij} \tag{3.3}$$

$$s_{ij} = \sin\theta_{ij} \tag{3.4}$$

The flavor states can then be written as:

$$\begin{pmatrix} \nu_e \\ \nu_\mu \\ \nu_\tau \end{pmatrix} = \begin{pmatrix} c_{12}c_{13} & s_{12}c_{13} & s_{13}e^{-i\delta} \\ -s_{23}s_{13}e^{i\delta}c_{12} - s_{12}c_{23} & -s_{23}s_{13}e^{i\delta}s_{12} + c_{12}c_{23} & c_{13}s_{23} \\ -c_{23}s_{13}e^{i\delta}c_{12} + s_{12}s_{23} & -c_{23}s_{13}e^{i\delta}s_{12} - c_{12}s_{23} & c_{13}c_{23} \end{pmatrix} \begin{pmatrix} \nu_1 \\ \nu_2 \\ \nu_3 \end{pmatrix} \tag{3.5}$$

The time evolution of a particular flavor state is given by:

$$|\nu_\alpha(t)\rangle = \sum_i U^*_{\alpha i} e^{-iE_i t} |\nu_i\rangle \tag{3.6}$$

where E_i is the i^{th} energy of the mass eigenstate $|\nu_i\rangle$. The transition amplitude from a flavor eigenstate α to another flavor eigenstate β for a given time t can be written as:

$$\begin{aligned} \langle\nu_\beta|\nu_\alpha(t)\rangle &= \left(\sum_j \langle\nu_j| U^T_{j\beta}\right)\left(\sum_i U^*_{i\alpha} e^{-iE_i t}|\nu_i\rangle\right) \\ &= \sum_i U^*_{\alpha i} e^{-iE_i t} U_{\beta i} \end{aligned} \tag{3.7}$$

The probability for a neutrino of flavor α to oscillate into another flavor β after time t can be written as:

$$P_{\nu_\alpha \to \nu_\beta}(t) = |\langle\nu_\beta|\nu_\alpha(t)\rangle|^2 = \left|\sum_{i,j} U^*_{\alpha i} U_{\beta i} U_{\alpha j} U^*_{\beta j} e^{-i(E_i - E_j)t}\right| \tag{3.8}$$

Because neutrinos are extremely relativistic, using the "equal-momentum approximation",

$$E_i = \sqrt{p^2 + m_i^2} \approx p + \frac{m_i^2}{2p} \tag{3.9}$$

Thus,

$$E_i - E_j = (p + \frac{m_i^2}{2p}) - (p + \frac{m_j^2}{2p}) = \frac{m_i^2 - m_j^2}{2p} \approx \frac{\Delta m_{ij}^2}{2E} \tag{3.10}$$

where Δm_{ij}^2 is the mass splitting of the mass eigenstates $|\nu_i\rangle$. In natural units (i.e. $c = 1$),

$$t = L \tag{3.11}$$

where L is the distance a neutrino travels from origin to detection. In terms of experimental parameters, L is called the baseline of the experiment. Now,

$$P_{\nu_\alpha \to \nu_\beta}(t) = \left| \sum_{i,j} U_{\alpha i}^* U_{\beta i} U_{\alpha j} U_{\beta j}^* e^{-i \frac{\Delta m_{ij}^2}{2E} L} \right| \tag{3.12}$$

A term of 0 can be added into 3.12 in the following manner

$$P_{\nu_\alpha \to \nu_\beta}(t) = \left| \sum_{i,j} U_{\alpha i}^* U_{\beta i} U_{\alpha j} U_{\beta j}^* e^{-i \frac{\Delta m_{ij}^2}{2E} L} \right| \tag{3.13}$$

$$= \left| \sum_{i,j} U_{\alpha i}^* U_{\beta i} U_{\alpha j} U_{\beta j}^* (e^{-i \frac{\Delta m_{ij}^2}{2E} L} - 1) + \sum_{i,j} U_{\alpha i}^* U_{\beta i} U_{\alpha j} U_{\beta j}^* \right| \tag{3.14}$$

Notice:

$$\sum_{i,j} U^*_{\alpha i} U_{\beta i} U_{\alpha j} U^*_{\beta j} = \sum_i U^*_{\alpha i} U_{\beta i} \sum_j U_{\alpha j} U^*_{\beta j} \tag{3.15}$$

$$= \delta_{\alpha\beta} \tag{3.16}$$

So, 3.12 can be written as:

$$P_{\nu_\alpha \to \nu_\beta}(t) = \left| \delta_{\alpha\beta} + \sum_{i,j} U^*_{\alpha i} U_{\beta i} U_{\alpha j} U^*_{\beta j} (e^{-i\frac{\Delta m^2_{ij}}{2E}L} - 1) \right| \tag{3.17}$$

The summation over i and j can be broken up into $i = j$, $i < j$, and $i > j$. For $i = j$, the sum evaluates to zero. Additionally, the summation over $i < j$ may be switched at the expense of a complex conjugation. Putting this all together:

(3.18)

$$P_{\nu_\alpha \to \nu_\beta}(t) = \left| \delta_{\alpha\beta} + \sum_{i>j} U^*_{\alpha i} U_{\beta i} U_{\alpha j} U^*_{\beta j} (e^{-i\frac{\Delta m^2_{ij}}{2E}L} - 1) + \sum_{i>j} U^*_{\alpha j} U_{\beta j} U_{\alpha i} U^*_{\beta i} (e^{i\frac{\Delta m^2_{ij}}{2E}L} - 1) \right|$$

For simplicity, define:

$$\Delta_{ij} \equiv \frac{\Delta m^2_{ij}}{2E} L \tag{3.19}$$

and so 3.18 becomes:

$$P_{\nu_\alpha \to \nu_\beta}(t) = \Big| \delta_{\alpha\beta} + \sum_{i>j} U^*_{\alpha i} U_{\beta i} U_{\alpha j} U^*_{\beta j} [(\cos \Delta_{ij} - 1) - i \sin \Delta_{ij}] + \sum_{i>j} U^*_{\alpha j} U_{\beta j} U_{\alpha i} U^*_{\beta i} [(\cos \Delta_{ij} - 1) + \sin \Delta_{ij}] \Big| \tag{3.20}$$

(3.21)

Let A and B represent the real and imaginary parts of $U^*_{\alpha i}U_{\beta i}U_{\alpha j}U^*_{\beta j}$. Then:

$$P = \left|\delta_{\alpha\beta} + \sum_{i>j}(A+iB)[(\cos\Delta_{ij}-1) - i\sin\Delta_{ij})] + \sum_{i>j}(A-iB)[(\cos\Delta_{ij}-1) + i\sin\Delta_{ij})]\right|$$

Combining the sums and expanding out the multiplications:

$$P_{\nu_\alpha\to\nu_\beta}(t) = \left|\delta_{\alpha\beta} + 2\sum_{i>j}[A(\cos\Delta_{ij}-1) + B\sin\Delta_{ij}]\right| \tag{3.22}$$

$$= \left|\delta_{\alpha\beta} - 4\sum_{i>j}A\sin^2(\frac{\Delta_{ij}}{2}) + 2\sum_{i>j}B\sin\Delta_{ij}]\right| \tag{3.23}$$

Thus the formula which describes neutrino oscillations is,

$$\begin{aligned} P_{\nu_\alpha\to\nu_\beta}(L) =& \delta_{\alpha\beta} - 4\sum_{i>j}\mathrm{Re}(U^*_{\alpha i}U_{\beta i}U_{\alpha j}U^*_{\beta j})\sin^2(\frac{\Delta m^2_{ij}}{4E}L) \\ &+2\sum_{i>j}\mathrm{Im}(U^*_{\alpha i}U_{\beta i}U_{\alpha j}U^*_{\beta j})\sin(\frac{\Delta m^2_{ij}}{2E}L) \end{aligned} \tag{3.24}$$

Including the factors of $\hbar$ and c, 3.24 becomes:

$$\begin{aligned} P_{\nu_\alpha\to\nu_\beta}(L) =& \delta_{\alpha\beta} - 4\sum_{i>j}\mathrm{Re}(U^*_{\alpha i}U_{\beta i}U_{\alpha j}U^*_{\beta j})\sin^2(\frac{1.27\Delta m^2_{ij}}{E}L) \\ &+2\sum_{i>j}\mathrm{Im}(U^*_{\alpha i}U_{\beta i}U_{\alpha j}U^*_{\beta j})\sin(\frac{2.54\Delta m^2_{ij}}{E}L) \end{aligned} \tag{3.25}$$

In 3.25, the units become those useful for neutrino oscillation experiments, namely:

- $\Delta m^2_{ij} \to eV^2$
- $L \to m$
- $E \to eV$

For conventional neutrino oscillations, 3.25 shows that not only do neutrinos have to have a non-zero mass but these masses must be different due to the factor of Δm^2_{ij} appearing in

the oscillation probability. The current best values for the different mixing parameters [1] are listed in Table 3.1.

TABLE 3.1. Best values for various mixing parameters in conventional neutrino oscillations assuming normal hierarchy as of 29 August, 2014 [1].

Parameter	Value
$\sin^2(\theta_{12})$	0.308 ± 0.017
$\sin^2(\theta_{23})$	$0.437^{+0.033}_{-0.023}$
$\sin^2(\theta_{13})$	$0.0234^{+0.0020}_{0.0019}$
$\frac{\delta}{\pi}$	$1.39^{+0.38}_{-0.27}$

CHAPTER 4

LV Neutrino Oscillations

This chapter provides motivating reasons to study Lorentz violation in neutrinos. Additionally, The Standard Model Extension (SME) is introduced, described, and predictions for neutrinos in the SME are outlined. Neutrinos in the SME satisfy a Dirac-like equation in which Lorentz violating operators are introduced. The conventional and SME Hamiltonians are described. Time dependent perturbation methods are using to derive the oscillation probabilities in the SME. The limit in which the baseline is much shorter than the oscillation length is applicable for the T2K near detectors and is considered. This probability expression is outlined and its features are described.

4.0.1. Motivation for searching for Lorentz violation. General Relativity and the Standard Model constitute our best description of nature and indeed both have been rigorously tested throughout history. Physicists, however, believe that General Relativity and the Standard Model are low energy limits of a more fundamental description of nature. It is expected that General Relativity and the Standard Model will merge together to form a single, fundamental theory at the Planck energy scale. Examples of these theories include quantum gravity, string theory, and loop quantum gravity. However, when a theory is written that attempts to combine General Relativity and the Standard Model, the resulting theory is not renormalizable. A way of handling this non-remormalizability is to allow for the breaking of Lorentz symmetry. This breaking is suppressed by the ratio of the electroweak and Planck scales:

$$\frac{m_W}{m_P} \sim \frac{10^2 GeV}{10^{19} GeV} \sim 10^{-17}. \tag{4.1}$$

While Lorentz symmetry breaking is highly suppressed, it is possible that low energy signals of Lorentz symmetry breaking may be detected by current experimental technologies. Any statistically significant detection of Lorentz symmetry breaking (i.e. LV) may provide physicists further insight into a quantum theory of gravity and the nature of the early universe. A theoretical framework developed to study the effects of LV in experiments is the SME [5].

4.0.2. The SME and its predictions for neutrinos. The Standard Model Extension (SME) is a general theoretical framework conceived to facilitate experimental investigations of LV and CPT violation (CPTV) [5]. It is an effective field theory that contains General Relativity, the Standard Model, and all possible Lorentz violating operators. The SME allows for the spontaneous breaking of Lorentz symmetry which produces a tensor background field that permeates throughout the universe. Neutrinos, couple to this background field with some given strength. Thus, the physics that the SME predicts becomes dependent for example, on the absolute direction of neutrino propagation. This dependency can produce a number of effects such as sidereal variations. The SME uses standard fields and thus does not introduce any new particles or new forces. It is observer invariant (i.e. invariant under observer transformations) and LV is controlled by a set of coefficients which experiments may measure. Below is a list of unique features in the SME:

- Unconventional neutrino energy dependence in oscillations: $E, E^2, \ldots$
- Corrections to neutrino dispersion relations
- Sidereal variations in oscillations with the Earth's sidereal frequency
- Annual variations in oscillations
- Neutrino-antineutrino mixing
- CPT violation

A search for sidereal variations in neutrino event rates at the T2K near detectors is performed. In general, a LV analysis may be performed at SuperK. However due to the limited statistical sample of ν_μ at SuperK from the T2K beam, a SuperK LV analysis is not being performed currently. A SuperK LV analysis has been performed using atmospheric neutrinos [6]. A description of neutrinos in the SME is discussed next.

4.0.3. Neutrinos in the SME. Neutrinos in the SME satisfy a Dirac-like equation [7]:

$$\Big(i\mathbf{\Gamma}^\mu\partial_\mu - \mathbf{M}\Big)\psi = \mathbf{0}, \tag{4.2}$$

where:

$$\mathbf{\Gamma}^\nu \equiv \gamma^\nu + c^{\mu\nu}\gamma_\mu + d^{\mu\nu}\gamma_5\gamma_\mu + e^\mu + if^\mu\gamma_5 + \frac{1}{2}g^{\alpha\beta\nu}\sigma_{\alpha\beta} + \ldots \tag{4.3}$$

contains the usual part (γ^ν) in addition to the different SME coefficients that control LV. Also:

$$\mathbf{M} \equiv m + im_5\gamma_5 + a^\mu\gamma_\mu + b^\mu\gamma_5\gamma_\mu + \frac{1}{2}H^{\alpha\beta}\sigma_{\alpha\beta} + \ldots \tag{4.4}$$

is the usual mass term in addition to the different SME coefficients. The indices on the coefficients are space-time indices. Coefficients with an odd number of indices are CPT odd while coefficients with an even number of indices are CPT even. Additionally,

$$\sigma^{\alpha\beta} = \frac{i}{2}[\gamma^\alpha, \gamma^\beta] \tag{4.5}$$

LV and CPTV in left-handed neutrino and their anti-neutrino oscillations may be characterized by a 6×6 effective Hamiltonian [8]:

$$(h_{eff})_{AB} = (h_0)_{AB} + (\delta h)_{AB}, \tag{4.6}$$

where $(h_0)_{AB}$ describes the conventional Lorentz invariant mass-driven neutrino oscillations and $(\delta h)_{AB}$ includes LV effects. The uppercase indices span all active neutrino and anti-neutrino flavors: $A, B = e, \mu, \tau, \bar{e}, \bar{\mu}, \bar{\tau}$. The focus of this analysis will be on left-handed neutrino flavors $a, b, \ldots = e, \mu, \tau$. Additionally, "neutrino" from here on out will mean left-handed neutrinos unless otherwise stated.

Using standard assumptions, h_0 introduces no mixing between neutrinos and antineutrinos and is, thus, block diagonal:

$$h_0 = \begin{pmatrix} (h_0)_{ab} & 0 \\ 0 & (h_0)_{\bar{a}\bar{b}} \end{pmatrix} = \frac{1}{2E} \begin{pmatrix} \Delta m^2_{ab} & 0 \\ 0 & \Delta m^2_{\bar{a}\bar{b}} \end{pmatrix} \tag{4.7}$$

where E is the neutrino energy, $a, b \cdots = e, \mu, \tau$ indicate neutrinos, $\bar{a}, \bar{b} \cdots = \bar{e}, \bar{\mu}, \bar{\tau}$ indicate antineutrinos, and $\Delta m^2_{ab} = m^2_a - m^2_b$ is the mass splitting between neutrinos of flavor a and b. The two 3×3 matrices are related by:

$$\delta m^2_{\bar{a}\bar{b}} = \delta m^{2*}_{ab} \tag{4.8}$$

from the CPT theorem.

The Lorentz-violating portion, δh, can be written as:

$$\delta h = \begin{pmatrix} \delta h_{ab} & \delta h_{a\bar{b}} \\ \delta h_{\bar{a}b} & \delta h_{\bar{a}\bar{b}} \end{pmatrix} \tag{4.9}$$

For Lorentz-violating operators which are of renormalizable dimension, the upper-left block can be written as [8]:

$$\delta h_{ab} = \frac{1}{E}\left[(a_L)^{\alpha} p_{\alpha} - (c_L)^{\alpha\beta} p_{\alpha} p_{\beta}\right]_{ab}, \tag{4.10}$$

where E is the neutrino energy, $(a_L)^{\alpha}_{ab}$ and $(c_L)^{\alpha\beta}_{ab}$ are Hermitian 3×3 complex matrices associated with the LV operators, and $p_{\alpha} \simeq E(1; -\hat{p})$ is the neutrino four-momentum. The four-momentum introduces energy dependence E as well as neutrino propagation directional dependence. $(a_L)^{\alpha}_{ab}$ and $(c_L)^{\alpha\beta}_{ab}$ have mass dimensions of 1 and 0 respectively.

Similarly, the lower-right diagonal block produces mixing between antineutrinos:

$$\delta h_{\bar{a}\bar{b}} = \frac{1}{E}\left[(a_R)^{\alpha} p_{\alpha} - (c_R)^{\alpha\beta} p_{\alpha} p_{\beta}\right]_{\bar{a}\bar{b}} \tag{4.11}$$

$$= \frac{1}{E}\left[-(a_L)^{\alpha} p_{\alpha} - (c_L)^{\alpha\beta} p_{\alpha} p_{\beta}\right]^{*}_{ab} \tag{4.12}$$

The off-diagonal 3×3 blocks of δh give rise to neutrino-antineutrino mixing. This is an unconventional effect and does not appear in the conventional Dirac Hamiltonian. These blocks can be written as:

$$\delta h_{a\bar{b}} = -i\sqrt{2}(\sigma_{+})_{\alpha}[\tilde{g}^{\alpha\beta} p_{\beta} - \tilde{H}^{\alpha}]_{a\bar{b}}, \tag{4.13}$$

$$\delta h_{\bar{a}b} = i\sqrt{2}(\sigma_{+})^{*}_{\alpha}[\tilde{g}^{\alpha\beta} p_{\beta} - \tilde{H}^{\alpha}]_{\bar{a}b} \tag{4.14}$$

$$i\sqrt{2}(\sigma_{+})^{*}_{\alpha}[\tilde{g}^{\alpha\beta} p_{\beta} - \tilde{H}^{\alpha}]_{a\bar{b}} \tag{4.15}$$

The complex coefficients for Lorentz violation in 4.0.3 obey the following relations:

$$\tilde{g}^{\alpha\beta}_{a\bar{b}} = \tilde{g}^{\alpha\beta}_{b\bar{a}} = \tilde{g}^{\alpha\beta *}_{\bar{b}a} \tag{4.16}$$

$$\tilde{H}^{\alpha}_{a\bar{b}} = -\tilde{H}^{\alpha}_{b\bar{a}} = \tilde{H}^{\alpha *}_{\bar{b}a} \tag{4.17}$$

The complex 4-vector $(\sigma_+)_\alpha = (0, -\vec{\sigma}_+)$ represents the helicity state. The local beam direction, $\hat{e}_r$, and other unit vectors associated with local spherical coordinates can be written as:

$$\hat{e}_r = (\sin\theta\cos\phi, \sin\phi, \cos\theta) \tag{4.18}$$

$$\hat{e}_\theta = (\cos\theta\cos\phi, \cos\theta\sin\phi, -\sin\theta) \tag{4.19}$$

$$\hat{e}_\phi = (-\sin\phi, \cos\phi, 0) \tag{4.20}$$

The 3-vector $\hat{\sigma}_+$ can be written as:

$$\hat{\sigma}_+ = \frac{1}{\sqrt{2}}(\hat{e}_\theta + i\hat{e}_\phi) \tag{4.21}$$

Since $(\delta h)_{ab}$ is inherently small, time dependent perturbation techniques may be used to expand the neutrino oscillation amplitudes, $S^{(j)}_{ab}$, about $(\delta h)_{ab}$. The oscillation probabilities are:

$$P_{\nu_b \to \nu_a} = \left| S^{(0)}_{ab} + S^{(1)}_{ab} + S^{(2)}_{ab} + \dots \right|^2. \tag{4.22}$$

The oscillation amplitudes are written out to second order in LV coefficients below [8]:

$$S^{(0)}_{ab} = \sum_{a'} U^*_{a'a} U_{a'b} e^{-iE_{a'}t} \tag{4.23}$$

$$S^{(1)}_{ab}(t) = -it \sum_{cd} \left(\mathcal{M}^{(1)}_{ab}\right)_{cd} \delta h_{cd} \tag{4.24}$$

$$S^{(2)}_{ab}(t) = -\frac{1}{2} t^2 \sum_{cdef} \left(\mathcal{M}^{(2)}_{ab}\right)_{cdef} \delta h_{cd} \delta h_{ef} \tag{4.25}$$

The conventional oscillation amplitude is recovered in 4.23. In 4.24, the experiment-dependent factor $\left(\mathcal{M}^{(1)}_{ab}\right)_{cd}(t)$ is:

$$\left(\mathcal{M}^{(1)}_{ab}\right)_{cd}(t) = \sum_{a'b'} \tau^{(1)}_{a'b'}(t) U^*_{a'a} U_{a'c} U^*_{b'd} U_{b'b}, \tag{4.26}$$

where the primed indices represent the diagonal mass basis. $U_{\alpha\beta,(\alpha'\beta')}$ is a 6×6 matrix whose 3×3 sub-blocks contain the PMNS matrices for neutrinos and antineutrinos.

$$\tau^{(1)}_{a'b'}(t) = \begin{cases} e^{-iE_{b'}t} : & E_{a'} = E_{b'} \\ \\ \frac{exp(-iE_{a'}t) - exp(-iE_{b'}t)}{-i\Delta_{a'b'}t} : & \text{otherwise,} \end{cases} \tag{4.27}$$

with

$$\Delta_{\alpha'\beta'} = E_{\alpha'} - E_{\beta'}. \tag{4.28}$$

In 4.25, the experiment-dependent factor $\left(\mathcal{M}^{(2)}_{ab}\right)_{cd}(t)$ is:

$$\left(\mathcal{M}^{(2)}_{ab}\right)_{cd}(t) = \sum_{a'b'c'} \tau^{(2)}_{a'b'c'}(t) U^*_{a'a} U_{a'c} U^*_{c'd} U_{c'e} U^*_{b'f} U_{b'b} \tag{4.29}$$

and:

$$\tau^{(2)}_{a'b'c'}(t) = \begin{cases} e^{-iE_{b'}t} : & E_{a'} = E_{b'} = E_{c'} \\ \\ 2\frac{\tau^{(1)}_{a'b'} - \tau^{(1)}_{c'b'}}{-i\Delta_{a'c'}t} = 2\frac{\tau^{(1)}_{a'c'} - \tau^{(1)}_{a'b'}}{-i\Delta_{c'b'}t} : & \text{otherwise} \end{cases} \tag{4.30}$$

Writing explicitly the probability terms out to second order in $(\delta h)_{ab}$:

$$P^{(0)}_{\nu_b \to \nu_a} = |S^{(0)}_{ab}|^2 \tag{4.31}$$

$$P^{(1)}_{\nu_b \to \nu_a} = 2Re\left(\left(S^{(0)}_{ab}\right)^* S^{(1)}_{ab}\right) \tag{4.32}$$

$$P^{(2)}_{\nu_b \to \nu_a} = 2Re\left(\left(S^{(0)}_{ab}\right)^* S^{(2)}_{ab}\right) + |S^{(1)}_{ab}|^2 \tag{4.33}$$

The conventional massive neutrino oscillation probabilities are recovered in 4.31. It is only at second order in the probability expression 4.33 that the oscillation amplitude is not coupled to the conventional oscillation amplitude. For baselines L that are much shorter than the neutrino oscillation lengths, the conventional oscillation amplitude vanishes. At second order in $(\delta h)_{ab}$, the first non-zero probability of oscillation occurs for the short baseline limit. Thus, neutrino oscillations which occur at short baselines compared to their oscillation lengths may be due entirely to LV effects.

4.0.4. Short baseline oscillation probability expression. The T2K LV analysis utilizes the minimal SME, which contains all renormalizable LV operators of dimension two [8]. Oscillations between the three neutrino flavors is given by the following Hamiltonian [9]

$$(h_{eff})_{ab} = \frac{1}{E}\left[(a_L)^\alpha p_\alpha - (c_L)^{\alpha\beta} p_\alpha p_\beta\right]_{ab}, \tag{4.34}$$

where E is the neutrino energy, $(a_L)^{\alpha}_{ab}$ and $(c_L)^{\alpha\beta}_{ab}$ are associated with the LV operators, and $p_\alpha \simeq E(1; -\hat{p})$ is the neutrino four-momentum. The four-momentum introduces energy dependence E as well as neutrino propagation directional dependence. The SME Coefficients, $(a_L)^{\alpha}_{ab}$ and $(c_L)^{\alpha\beta}_{ab}$, have mass dimensions of 1 and 0 respectively. The oscillation amplitudes may be expanded in powers of $(h_{eff})_{ab}$ as a good approximation:

$$S(L) \simeq 1 - \frac{i(h_{eff})_{ab}L}{\hbar c} - \frac{(h_{eff})^2_{ab}L^2}{2(\hbar c)^2} + \cdots \tag{4.35}$$

At leading order in the short baseline approximation, the probability of a ν_a type neutrino oscillating into a ν_b type neutrino is given by [9]:

$$P_{\nu_b \to \nu_a} \simeq \begin{cases} 1 - \sum_{c, c \neq a} P_{\nu_a \to \nu_c} : & a = b \\ \\ |(h_{eff})_{ab}|^2 \frac{L^2}{(\hbar c)^2} : & a \neq b \end{cases} \tag{4.36}$$

When reporting results, it is necessary to specify a frame of reference. For convenience and from convention, the Sun-centered frame is chosen as the inertial frame, although in principle any inertial frame may be chosen. The Z axis of this frame is directed north and parallel to the rotational axis of the Earth. The X axis points from the Sun towards the vernal equinox. The Y axis completes a right-handed coordinate system. A schematic is given in Figure 4.1. For neutrino oscillation experiments fixed on Earth, like T2K, the rotation of the Earth causes the neutrino propagation direction $\hat{p}$ to change with respect to the Sun-centered coordinate system. This rotation causes the components of $\hat{p}$ to vary with the sidereal frequency of the Earth ($\omega_\oplus = \frac{2\pi}{23^h 56^m 4.0916^s}$) when $\hat{p}$ does not point along the Earth's rotational axis. To emphasize the importance of rotations, a spherical harmonic

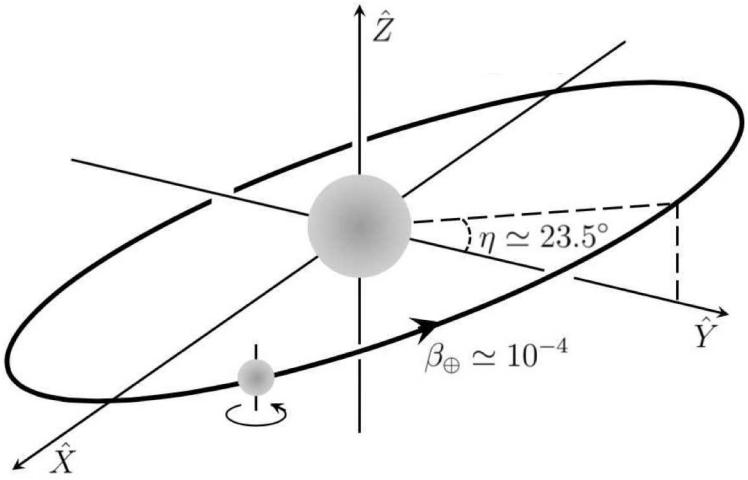

FIGURE 4.1. Schematic of Sun-centered coordinate system used in SME framework

decomposition of the Lorentz violating coefficients can be performed as described in [10]. Once the decomposition has been performed, the oscillation probability expression becomes:

$$P_{\nu_b \to \nu_a} = \frac{L^2}{(\hbar c)^2} \Big| (\mathcal{C})_{ab} + (\mathcal{A}_s)_{ab} \sin(\omega_\oplus T_\oplus) + (\mathcal{A}_c)_{ab} \cos(\omega_\oplus T_\oplus) + (\mathcal{B}_s)_{ab} \sin(2\omega_\oplus T_\oplus) + (\mathcal{B}_c)_{ab} \cos(2\omega_\oplus T_\oplus) \Big|^2. \tag{4.37}$$

In 4.37, the oscillation probability expression depends on the *Local Sidereal Time* of the neutrino event ($T_\oplus$). Thus, the smoking gun of LV in neutrino oscillation experiments is a sidereal time dependence in the neutrino event rate at the near detector. The expression also involves the sidereal frequency of the Earth ($\omega_\oplus$) and the combinations of the $(a_L)^\alpha_{ab}, (c_L)^{\alpha\beta}_{ab}$ SME coefficients $((\mathcal{C})_{ab}, (\mathcal{A}_s)_{ab}, (\mathcal{A}_c)_{ab}, (\mathcal{B}_s)_{ab}, (\mathcal{B}_c)_{ab})$. These combinations are written out

explicitly [9]:

$$(\mathcal{C})_{ab} = (\mathcal{C})^{(0)}_{ab} + E(\mathcal{C})^{(1)}_{ab} \tag{4.38}$$

$$(\mathcal{A}_s)_{ab} = (\mathcal{A}_s)^{(0)}_{ab} + E(\mathcal{A}_s)^{(1)}_{ab} \tag{4.39}$$

$$(\mathcal{A}_c)_{ab} = (\mathcal{A}_c)^{(0)}_{ab} + E(\mathcal{A}_c)^{(1)}_{ab} \tag{4.40}$$

$$(\mathcal{B}_s)_{ab} = E(\mathcal{B}_s)^{(1)}_{ab} \tag{4.41}$$

$$(\mathcal{B}_c)_{ab} = E(\mathcal{B}_c)^{(1)}_{ab} \tag{4.42}$$

where E is the neutrino energy. The baseline-energy dependence in 4.37 goes as $(LE)^2$. These combinations may be further decomposed into expressions in terms of the components of a directional factor vector $(\hat{N}^X, \hat{N}^Y, \hat{N}^Z)$ containing information about the beam-direction with respect to Earth, and the SME coefficients $(a_L)^{\alpha}_{ab}$ and $(c_L)^{\alpha\beta}_{ab}$:

$$(\mathcal{C})^{(0)}_{ab} = (a_L)^T_{ab} - \hat{N}^Z (a_L)^Z_{ab} \tag{4.43}$$

$$(\mathcal{C})^{(1)}_{ab} = -\frac{1}{2}(3 - \hat{N}^Z\hat{N}^Z)(c_L)^{TT}_{ab} + 2\hat{N}^Z(c_L)^{TZ}_{ab} + \frac{1}{2}(1 - 3\hat{N}^Z\hat{N}^Z)(c_L)^{ZZ}_{ab} \tag{4.44}$$

$$(\mathcal{A}_s)^{(0)}_{ab} = \hat{N}^Y (a_L)^X_{ab} - \hat{N}^X (a_L)^Y_{ab} \tag{4.45}$$

$$(\mathcal{A}_s)^{(1)}_{ab} = -2\hat{N}^Y (c_L)^{TX}_{ab} + 2\hat{N}^X (c_L)^{TY}_{ab} + 2\hat{N}^Y\hat{N}^Z (c_L)^{XZ}_{ab} - 2\hat{N}^X\hat{N}^Z (c_L)^{YZ}_{ab} \tag{4.46}$$

$$(\mathcal{A}_c)^{(0)}_{ab} = -\hat{N}^X (a_L)^X_{ab} - \hat{N}^Y (a_L)^Y_{ab} \tag{4.47}$$

$$(\mathcal{A}_c)^{(1)}_{ab} = 2\hat{N}^X (c_L)^{TX}_{ab} + 2\hat{N}^Y (c_L)^{TY}_{ab} - 2\hat{N}^X\hat{N}^Z (c_L)^{XZ}_{ab} - 2\hat{N}^Y\hat{N}^Z (c_L)^{YZ}_{ab} \tag{4.48}$$

$$(\mathcal{B}_s)^{(1)}_{ab} = \hat{N}^X \hat{N}^Y [(c_L)^{XX}_{ab} - (c_L)^{YY}_{ab}] - [\hat{N}^X \hat{N}^X - \hat{N}^Y \hat{N}^Y](c_L)^{XY}_{ab} \tag{4.49}$$

$$(\mathcal{B}_c)^{(1)}_{ab} = -\frac{1}{2}(\hat{N}^X \hat{N}^X - \hat{N}^Y \hat{N}^Y)[(c_L)^{XX}_{ab} - (c_L)^{YY}_{ab}] - 2\hat{N}^X \hat{N}^Y (c_L)^{XY}_{ab} \tag{4.50}$$

The derivation of these expressions may be found in references [8] and [9]. The superscripts (T, X, Y, Z) on the SME coefficients are space-time indices in the sun-centered inertial frame and the L subscript indicates left handed neutrinos. $\hat{N}^X, \hat{N}^Y, \hat{N}^Z$ represent the neutrino propagation direction in the Sun-centered frame at local time $T_\oplus = 0$. This analysis will attempt to measure the different combinations of the SME coefficients, $(\mathcal{C})_{ab}, (\mathcal{A}_s)_{ab}, (\mathcal{A}_c)_{ab}$, $(\mathcal{B}_s)_{ab}, (\mathcal{B}_c)_{ab}$.

In the lab frame (x-y-z coordinate system of Figure 4.2), letting θ be the angle at the detector between the beam and the vertical upward direction, ϕ be the angle between the beam and south measured towards the east, and χ be the colatitude of the detector, the components of the propagation direction vector are [9]:

$$\begin{pmatrix} \hat{N}^X \\ \hat{N}^Y \\ \hat{N}^Z \end{pmatrix} = \begin{pmatrix} \cos\chi \sin\theta \cos\phi + \sin\chi \cos\theta \\ \sin\theta \sin\phi \\ -\sin\chi \sin\theta \cos\phi + \cos\chi \cos\theta \end{pmatrix} \tag{4.51}$$

Figure 4.2 is a schematic of the different angles in the lab frame:

The angles for the two T2K near detectors, INGRID and ND280, are described in Table 4.1. and the components of the detector geographical vector for INGRID are shown in

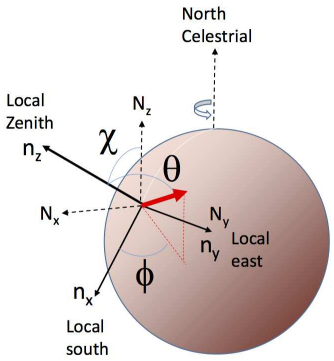

FIGURE 4.2. A schematic of the different angles and directional vectors used in the SME. The angle χ shown in the lab frame. This angle describes the colatitude of the detector. The angle θ shown in the lab frame. This angle is the angle at the detector between the beam and the vertical upward direction. The angle ϕ shown in the lab frame. This angle is the angle between beam and south as measured towards east.

Equation 4.52.

$$\begin{pmatrix} \hat{N}^X \\ \hat{N}^Y \\ \hat{N}^Z \end{pmatrix} = \begin{pmatrix} -0.0477251 \\ -0.997971 \\ -0.00116171 \end{pmatrix} \tag{4.52}$$

The components of the detector geographical vector for ND280 are shown in Equation 4.53.

$$\begin{pmatrix} \hat{N}^X \\ \hat{N}^Y \\ \hat{N}^Z \end{pmatrix} = \begin{pmatrix} -0.028716 \\ -0.999528 \\ 0.00174031 \end{pmatrix} \tag{4.53}$$

In Figures 4.3 - 4.5 show graphics showing the location of each one of T2Ks detectors on a map.

TABLE 4.1. INGRID and ND280 lab frame angles (x-y-z coordinate system in Figure 2) given in degrees.

Detector	θ	ϕ	χ
INGRID	93.637	270.319	53.55087
ND280	91.695	269.525	53.55085

FIGURE 4.3. A map of the near detectors at T2K. The red pin is ND280 and the purple pin is INGRID

FIGURE 4.4. A map of the far detector at T2K. The red pin is SK.

FIGURE 4.5. A map showing the the beam line for T2K. The purple pin is located on INGRID and the red pin is located on SK.

Figure 4.6 shows, in color, the survival probability for a ν_μ beam, as a function of sidereal time and energy. Maximally, the LV effect is $\sim 1\%$. The set of SME coefficients used

to generate this Figure corresponds to the current upper limits on the Standard Model Extension coefficients [11], and is listed in Table 4.2.

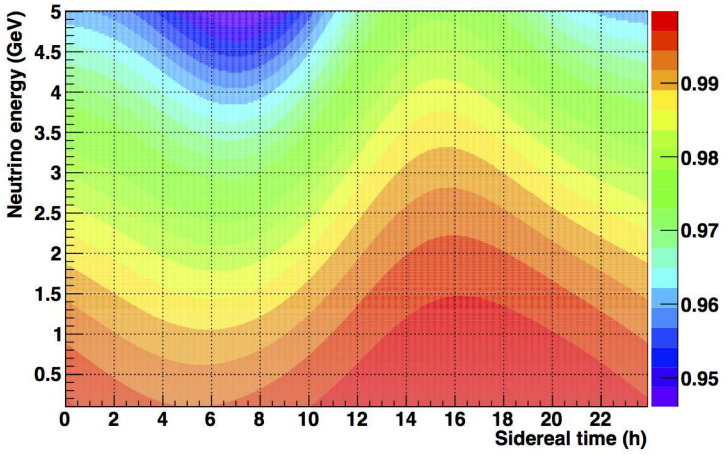

FIGURE 4.6. ν_μ survival probability (z-axis) as a function of the sidereal time and neutrino energy in the INGRID detector. Survival probability values are indicated in color. One observes an increase in both the sidereal time independent and sidereal time dependent variations with the neutrino energy.

TABLE 4.2. Standard Model Extension coefficients related to $\nu_\mu \rightarrow \nu_e$ oscillation used to produce the signal shown in Figure 4.6. Each coefficient has indices $a = e$ and $b = \mu$. These indices have been dropped from each entry for brevity

	$\times 10^{-20}$		$\times 10^{-20}$
a_L^T	4.2 GeV	a_L^X	0.16 GeV
a_L^Y	2.2 GeV	a_L^Z	4.2 GeV
c_L^{TT}	9.6	c_L^{TX}	0.009
c_L^{TY}	0.009	c_L^{TZ}	6.0
c_L^{XT}	0.009	c_L^{XX}	0.46
c_L^{XY}	0.22	c_L^{XZ}	0.11
c_L^{YT}	0.009	c_L^{YX}	0.22
c_L^{YY}	0.45	c_L^{YZ}	0.11
c_L^{ZT}	6.0	c_L^{ZX}	0.11
c_L^{ZY}	0.11	c_L^{ZZ}	34

One can see an enhancement of the oscillation probability with the neutrino energy, and the impact it has on both sidereal time independent and sidereal time dependent oscillations. Figure 4.6 shows how Lorentz violation is expected to impact the neutrino oscillation as a

function of the sidereal time, at the mean INGRID neutrino energy $E_\nu = 2.7$ GeV. Again, one can see both the time independent effect and the sidereal time oscillation. With the choice of SME coefficients described earlier, the effect we will probe is a 1% effect. In the study presented here, only a search for Lorentz violation for an average neutrino energy is performed.

CHAPTER 5

The Tokai to Kamioka Neutrino Oscillation Experiment

The Tokai to Kamioka (T2K) experiment is a long baseline neutrino oscillation experiment in Japan. The physics goals of T2K include:

(1) Measuring the mixing angle θ_{13} and δ_{CP} of the PMNS matrix by detecting ν_e appearance in a ν_μ beam.

(2) Making precision measurements of Δm^2_{23} and $\sin^2(2\theta_{23})$ through ν_μ disappearance.

T2K utilizes an off-axis neutrino beam for optimal detection of ν_e appearance at a peak neutrino energy of 0.6GeV with a baseline of 295km at the far detector. The off-axis nature of T2K produces a narrow band energy beam which falls within an oscillation maximum in addition to reducing the backgrounds associated with higher energy neutrinos. The experiment consists of a neutrino beam produced at the JPARC facility in Tokai, Japan, near detector site, and a far detector site. The beam is pointed 2.5° off-axis with respect to the far detector. An on-axis near detector, called the interactive neutrino grid (INGRID), monitors the beam stability and intensity while the off-axis near detector, called the near detector at 280m (ND280), is used to study neutrino interactions for different nuclear targets as well as study neutrino kinematics. Both near detectors are located at 280m from the graphite target used to create the T2K neutrino beam. ND280 consists of a suite of different sub-detectors. The far detector is the Super-Kamiokande water Cherenkov detector (SK). It is a 50kT detector that utilizes photo multiplier tubes (PMTs) to detect Cherenkov rings from different neutrino interactions. Each portion of T2K, from the beam creation to the far detector, will be described in detail below.

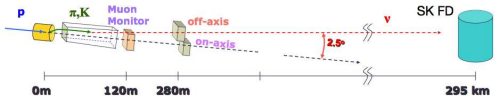

Figure 5.1. Schematic of the T2K experimental setup.

5.1.1. J-PARC. The creation of the T2K neutrino beam begins at the Japan Proton Accelerator Research Complex (J-PARC) in Tokai, Japan. At J-PARC, three accelerators are used to produce the neutrino beam for T2K [12]:

(1) Linear Accelerator (LINAC)

(2) Rapid-Cycling Synchrotron (RCS)

(3) Main Ring (MR)

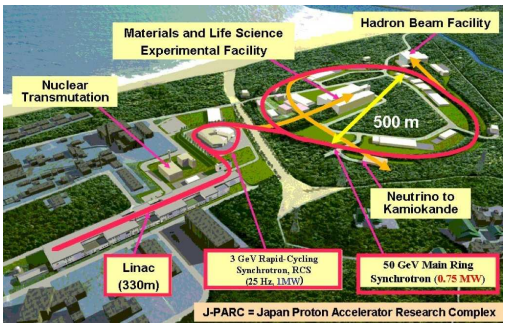

Figure 5.2. A diagram showing the layout of the J-PARC experimental facilities.

The LINAC accelerates a H^- beam spill up to 400 MeV. This H^- beam enters into the RCS where it is charged stripped using charge-stripping foils in order to create a H^+ beam (or proton beam). The proton beam is then accelerated up to 3GeV in the RCS with a cycle frequency of about 25Hz. Two bunches per cycle are produced and about 5% [12] of these bunches are supplied to the MR. Once the beam enters the MR, it is accelerated up to 30GeV in eight bunches. Two extraction modes, fast and slow, exist in the MR for extracting the proton bunches. The fast extraction mode is used for the T2K beam. In the

fast extraction mode, the circulating protons are extracted in a single turn using five kicker magnets. A summary of the MR parameters is provided in Table 5.1.

TABLE 5.1. Summary of the J-PARC Main Ring parameters.

Circumference	1567 m
Beam power	750 kW
Beam kinetic energy	30 GeV
Beam intensity	3×10^{14} protons/spill
Spill cycle	0.5 Hz
Number of bunches	8/spill
RF frequency	1.67 - 1.72 MHz
Spill width	5 μsec

5.1.2. PRIMARY AND SECONDARY BEAMLINE. The neutrino beamline consists of a primary and secondary beamline. The extracted protons in the primary beamline are extracted and directed into the secondary beamline. The protons in the secondary beamline are incident on a graphite target to produce pions which produce the neutrinos that ultimatley make up the T2K neutrino beam.

The primary beamline consists of three sections:

(1) The preparation section

(2) The arc section

(3) The focusing section

The preparation section tunes the extracted protons with eleven normal conducting magnets in order to prepare the beam for the arc section. In the arc section, the beam is bent toward Kamioka at an angle of 80.6° using fourteen superconducting magnets. In addition to these fourteen magnets, three pairs of superconducting magnets in the vertical and horizontal are used to steer the proton beam. Finally, in the focusing section, ten normal conducting

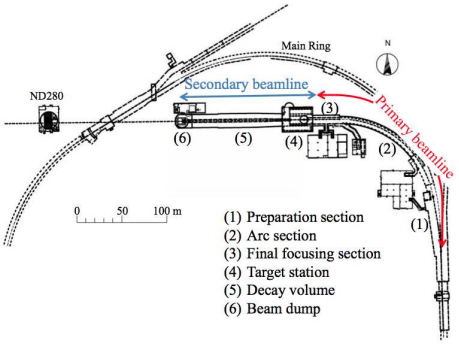

FIGURE 5.3. A diagram showing the components of the primary and secondary proton beam lines at J-PARC.

magnets focus the beam on to the graphite target and also direct the beam downwards into the Earth by 3.637° with respect to horizontal [12]. In each section of the primary beamline, a set of beam monitors is setup in order to produce a stable, high intensity beam to guarantee a stable neutrino beam.

The secondary beamline is located just after the focusing section of the primary beamline. The secondary beamline also consists of three sections:

(1) The target station

(2) The decay volume

(3) The beam dump

The target station contains a collimator to protect the magnetic horns used to steer the beam from the focusing section of the primary beamline, an optical transition radiation monitor (OTR) to monitor the proton beam profile directly upstream of the graphite target, the graphite target which is used to create secondary pions, and three magnetic horns which charge select the pions and focus them into the decay volume. The decay volume is a 96m long steel tunnel where the pions decay into mostly muons and ν_μ. To increase the purity of the neutrino content in the, now, neutrino beam a beam dump is introduced after the decay volume. The beam dump consists of a 3.174m long, 1.94m wide, and 4.69m high core that is

filled with 75 tons of graphite [12]. All hadrons and muons below 5GeV are stopped in the beam dump while the neutrinos travel through the beam dump towards the near detector site.

5.2. The Near Detector Site

The T2K near detector site consists of two near detectors:

(1) The Interactive Neutrino Grid (INGRID)

(2) The Off-axis near detector at 280m (ND280)

Both near detectors are located at a distance of 280m from the target station with INGRID lying on-axis with respect to the beamline and ND280 lying off-axis at 2.5° with respect to the beamline. ND280 is enclosed in the UA-1 dipole magnet while INGRID is not.

5.2.1. INGRID. INGRID was designed to directly measure the beam intensity and direction by utilizing neutrino interactions on iron [13]. INGRID lies on axis at 280m from the graphite target and is centered on the neutrino beam [12]. INGRID is arranged in a cross configuration with 14 identical modules to detect neutrino interactions from the beam. In addition to these 14 modules, two shoulder modules exist to check the axial symmetry of the neutrino beam. Each module consists of alternating layers of scintillator and iron plates. In each module, there are 11 scintillator tracking planes that consist of 24 horizontal and 24 vertical scintillator bars glued together. Each scintillator bar contains a wavelength shifting (WLS) fiber that connects to a Hamamatsu Multi-Pixel Photon Counter (MPPC). Between consecutive scintillator tracking planes are iron plates that serve as a target for neutrino interactions. The total iron mass available in INGRID for neutrino interactions in each module is 7.1 tons.

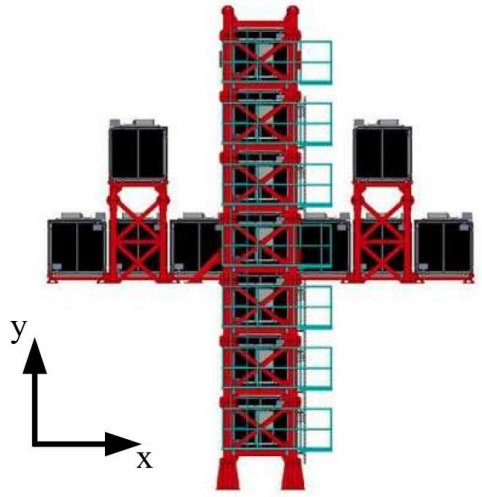

FIGURE 5.4. A diagram showing the layout of INGRID.

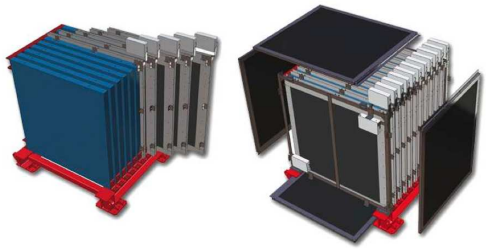

FIGURE 5.5. A diagram showing the layout of an INGRID module.

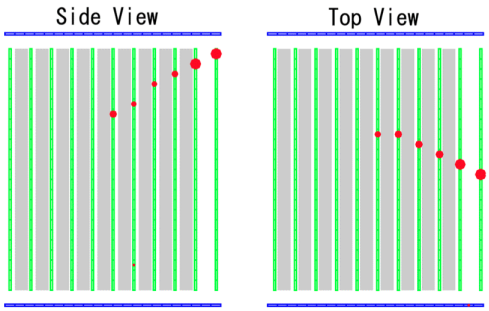

FIGURE 5.6. An event display showing a ν_μ interaction in an INGRID module.

5.2.2. ND280. ND280 was designed to perform several measurements [12]:

(1) Measure the neutrino flux and energy spectrum from the beam

(2) Measure the inherent ν_e contamination of the beam

(3) Measure neutrino event rates

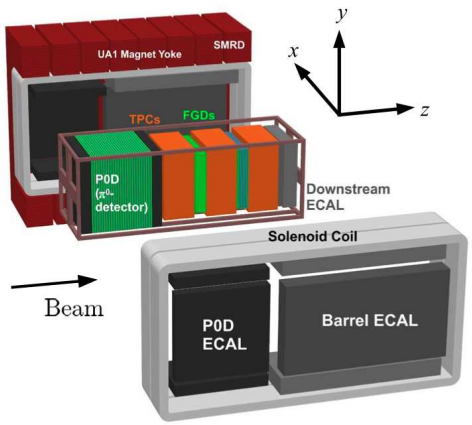

FIGURE 5.7. A blowout diagram of ND280 showing the different sub-detectors.

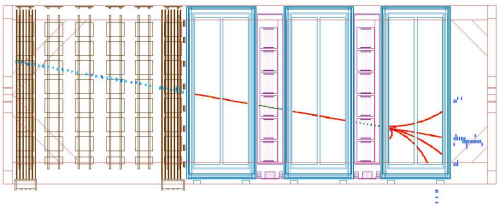

FIGURE 5.8. An event display showing a ν_μ event in ND280.

The neutrino flux and energy spectrum are measured at ND280 to determine the expected ν_μ flux and energy spectrum at Super-K with and without oscillations. As the main physics goal of T2K is to observe ν_e appearance at Super-K, the inherent ν_e contamination in the beam must be measured and constrained as this is a significant background for T2K at Super-K. Finally, ND280 must measure the different ν_μ interactions in order to precisely predict the backgrounds at Super-K. ND280 is a composite detector and consists of a suite of sub-detectors. Each sub-detector will be discussed below.

5.2.2.1. π^0 *Detector.* The π^0 detector, or P0D, was constructed to measure the following neutral current interaction on a water target:

$$\nu_\mu + N \rightarrow \nu_\mu + N + \pi^0 + X \tag{5.1}$$

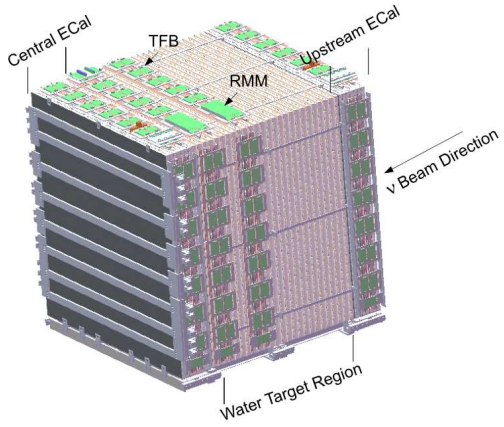

FIGURE 5.9. A diagram showing the electronics and segments of the P0D.

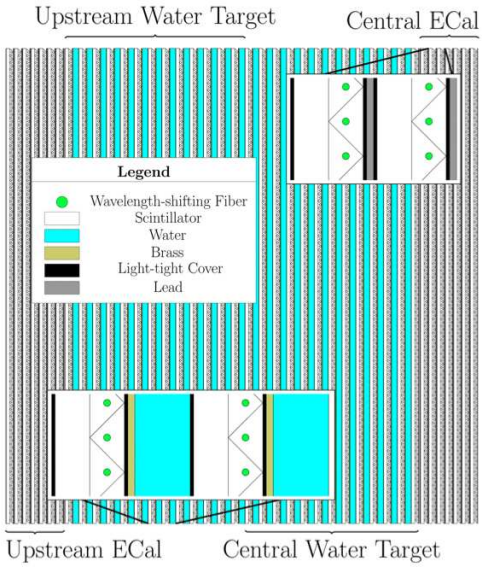

FIGURE 5.10. A schematic showing the different regions of the P0D.

using the same neutrino flux that is observed at Super-K. This process can be a serious background in T2K's main effort to measure $\nu_\mu \rightarrow \nu_e$ oscillations. The P0D consists of layers of scintillator, brass, lead, and water bags which provide a target for measuring neutrino cross sections. The water bags can be configured in a "water-in" or "water-out" mode to facilitate a subtraction method when calculating the neutrino cross section on water. The scintillator bars are finely segmented to reconstruct charged particle tracks such as muons and pions in addition to electromagnetic showers from electrons or photons produced from

π^0. Each scintillator bar contains a WLS fiber and is attached to an MPPC for readout. The anatomy of the P0D consists of an upstream electromagnetic calorimeter (ECal), upstream water target, central water target, and central ECal [14]. The upstream and downstream ECal consists of alternating layers of scintillator bars and lead. The upstream and central water targets consist of a scintillator layer, brass sheet, and water bag. The remaining portions of ND280 consist of three time projection chambers and two fine grain detectors which ultimately make up the Tracker region of ND280.

5.2.2.2. *Time Projection Chambers.* Downstream of the P0D are three time projection chambers (TPCs). The TPCs measure the charge, momentum, and particle types of the different charged particles that are produced in neutrino interactions below a few GeV[15]. Each TPC consists of an inner and outter box. The inner box contains an argon gas mixture for charged particles to ionize during their interactions in the TPCs. The ionized electrons travel towards a readout plane where they are multiplied and analyzed by micromegas detectors. The pattern of signal hits in the pad along with arrival times are used to produce 3D images of the particle tracks inside a TPC. The outter box contains a CO_2 atmosphere which provides electrical insulation between the inner box and ground while also keeping atmospheric oxygen from entering the inner box.

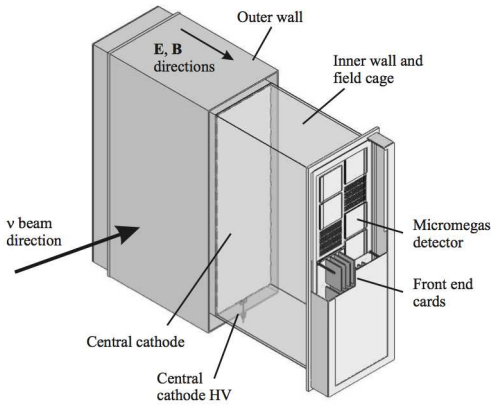

FIGURE 5.11. A schematic of a single TPC used in ND280.

5.2.2.3. *Fine Grained Detectors.* In addition to the P0D, two Fine Grained Detectors (FGD) were installed to provide a target for studying neutrino interactions in addition to tracking charged particles. Each FGD consists of finely segmented scintillator bars arranged in X and Y planes. Each scintillator bar contains a WLS fiber that connects to an MPPC. The first FGD contains 30 layers of scintillator with each layer containing 192 bars [12]. One module in an FGD consists of an X layer glued to a Y layer. The second FGD contains seven XY scintillator modules that are filled with water. The water acts as a target for studying neutrino interactions by comparing the interaction rates in FGD1 (without water) and FGD2 (with water). Similarly, cross section measurements on carbon may be studied in a similar fashion as water with both FGDs.

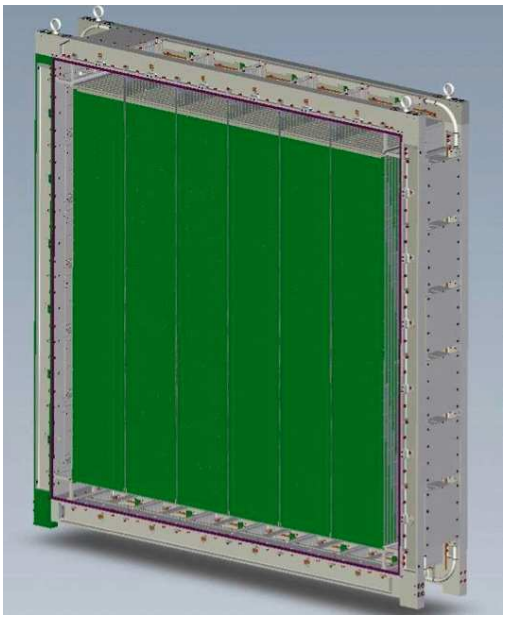

FIGURE 5.12. A diagram showing a single FGD used in ND280.

5.2.2.4. *Electromagnetic Calorimeters.* The electromagnetic calorimeters (ECals) of ND280 are sampling calorimeters located inside the magnet yokes and enclose the various subdetectors of ND280 (P0D, TPCs, FGDs). A total of thirteen ECals are used in ND280, six for the tracker, six for the P0D, and one at the very downstream end of the tracker. The

ECals serve to measure the energy and direction of charged particles that exit the sides of the ND280 subdetectors in order to identify particle types. Each ECal module consists of alternating layers of scintillator bars and lead sheets. A similar WLS as used in the INGRID modules is also used in the ECal scintillator bars. Each WLS is read out to an MPPC.

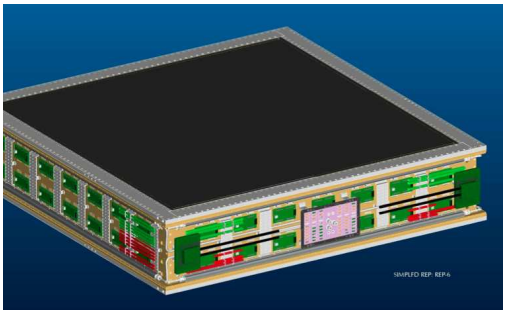

FIGURE 5.13. A diagram of the ECal used in ND280.

5.2.2.5. *Side Muon Range Detector.* The Side Muon Range Detector (SMRD) system is located between the air gaps in each magnet yoke. The SMRD serves three main purposes:

(1) To detect high angle muons that escape ND280 with respect to the beam line and measure their momentum.

(2) To trigger on cosmic ray muons that enter ND280.

(3) To identify beam interactions with the surrounding pit wall and iron in the magnet.

In each magnet yoke, there are sixteen individual steel plates that make up the yoke and thus there are fifteen air gaps per magnet yoke. The SMRD scintillator planes are located in each one of these air gaps on each magnet yoke. A total of 440 scintillator slabs exist in the magnet. Each scintillator slab consists of a WLS that, unlike the rest of ND280 subdetectors, is arranged in a serpentine configuration [16].

FIGURE 5.14. A photo showing the serpentine configuration of the WLS used in the SMRD.

The serpentine configuration allows for near uniform response of the WLS across the scintillator slab while also minimizing the number of MPPCs needed for a more standard straight line configuration.

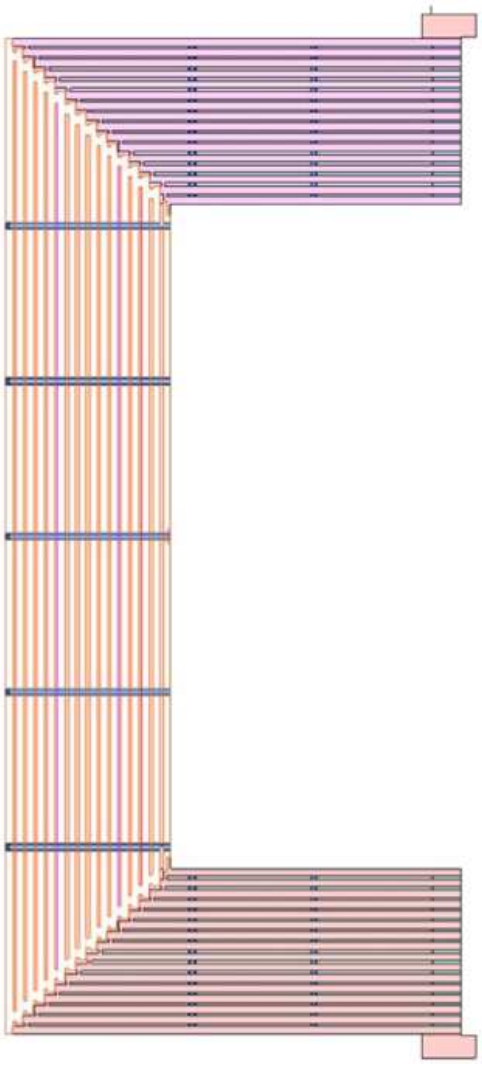

FIGURE 5.15. A diagram showing the construction of the SMRD.

5.3. THE FAR DETECTOR SITE

The far detector site for the T2K experiment is the Super-Kamiokande (Super-K) water Cherenkov detector and its monitoring facilities. Super-K is located 295 km west of the T2K target. It was built inside of Mt. Ikenoyama in Kamioka, Japan.

5.3.1. Super Kamiokande detector. Super-K is large cylindrical water Cherenkov detector that serves as the far detector for T2K. For T2K, Super-K's main purpose is to measure the flavor oscillation of ν_μ to either ν_e or ν_τ by observing and counting charged current quasi-elastic (CCQE) events for ν_μ and ν_e. The corresponding lepton released in these interactions can produce a Cherenkov ring in the water that allows the identification of the neutrino event in Super-K. Since the muons have a relatively large mass compared to the electron, the muons in Super-K from the T2K beam stop in Super-K with minimal scattering. Those produces a rather well defined Cherenkov light cone that produces crisp ring in Super-K. Conversely, the electrons in Super-K scatter much more frequently due to their lower mass and also tend to produce electromagnetic (EM) showers. The resulting Cherenkov ring is identified as fuzzy which can be thought of as the sum of the many Cherenkov rings produces by the EM shower.

The composition of Super-K consists of an inner detector (ID) and outer detector (OD). The ID is filled with 50 kton of ultra-pure water and its walls are lined with 11,129 Photo Multiplied Tubes (PMTs). The ID stands at 36.2 m high with a 33.8 m diameter. Each PMT in the ID faces inside the ID in order to detect the different Cherenkov rings as discussed above. The OD consists of 1,885 outward facing PMTs that serve as a veto for neutrino interactions coming from sources other than the T2K beam. In total, the height of Super-K is 42 m and the diameter is 39 m.

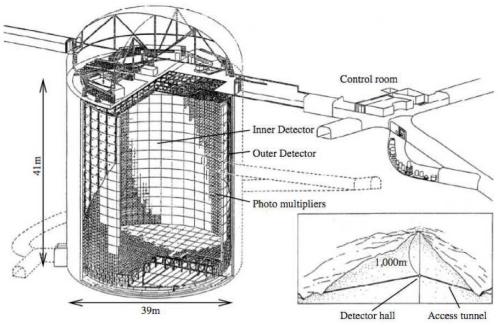

FIGURE 5.16. A diagram of the far detector site including the Super-K detector of T2K.

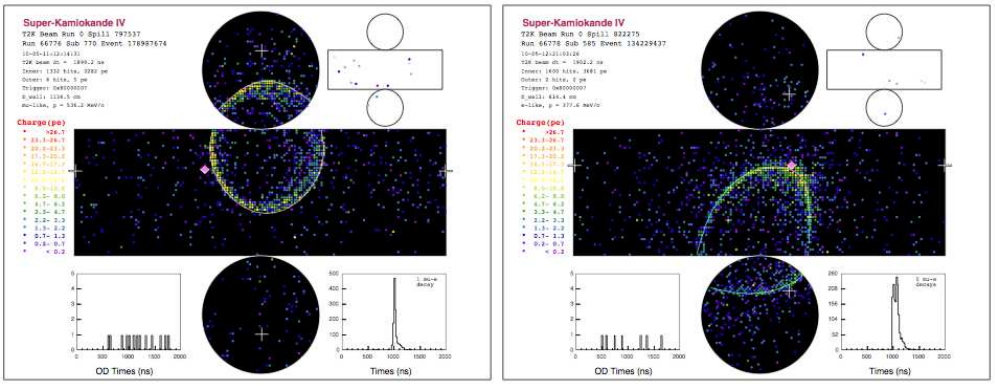

FIGURE 5.17. Event displays in Super-K during T2K running. The left display shows a ν_μ event while the right shows a ν_e event in Super-K.

CHAPTER 6

Neutrino Selection Methods for INGRID and ND280

The neutrino selection methods for INGRID and ND280 are described in detail in this chapter. Both detectors utilize Charged-Current Inclusive neutrino events to make up that detector's data set. The INGRID selection is described first and utilizes four variables in a likelihood function to construct a ν_μ selection/ ν_e rejection requirement. The final INGRID sample and the selections systematic uncertainties are summarized. The ND280 selection is described next. This selection uses events that originate in the P0D water target fiducial volume and have a negative track reconstructed in TPC1. Track matching criteria are defined and determined to match the two pieces. The final ND280 sample and the selections' systematic uncertainties are summarized.

6.1. ν_μ selection in INGRID

The INGRID ν_μ selection utilizes four variables. These four variables were chosen to distinguish tracks produced by electromagnetic showers from tracks produced by muons:

(1) Average track width

(2) Track length

(3) Root mean square of the track $\frac{dE}{dx}$

(4) Number of hits close to the interaction point

A likelihood function utilizing these variables is constructed to develop a ν_μ selection/ν_e rejection requirement best optimized for this analysis.

6.1.1. AVERAGE TRACK WIDTH. Electromagnetic (EM) showers generally have a transverse width that is larger than muon tracks due to bremsstrahlung and pair production. The average transverse width for the scattering of electrons increases with material density and depends on material type. The Molière Radius, R_M [1] defines the properties of an EM shower in a material. The Molière Radius represents a radius of a cylinder that contains 90% of the shower energy and is independent of the initial particle energy. A cylinder with radius $2R_M$ contains 99% of the shower energy. As the INGRID segments are made up of iron, the Molière radius of iron is $R_M = 1.719$ cm. Thus, a diameter of $4R_M = 6.8$ cm contains 99% of the energy from an EM shower in iron. As the INGRID scintillator granularity is 5 cm, the average EM shower transverse width is expected to be incident on more than one scintillator bar.

Figure 6.1 shows the profile of an EM shower in INGRID and confirms this expectation: The average transverse width is used instead of information about individual planes because

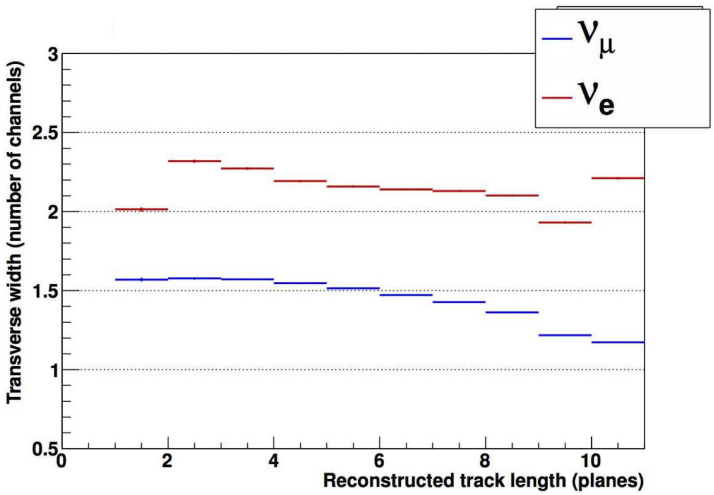

FIGURE 6.1. Average width of the electromagnetic shower in the transverse direction (given in number of 5 cm scintillators), as a function of the distance from the vertex (number of tracking planes crossed from MC. The red histogram is for electrons coming from ν_e interactions, the blue histogram for muons coming from ν_μ interactions.

EM shower processes leave many small hits in the scintillator which may cause the hit to not pass the 2.5 p.e. threshold due to an uncertainty (mostly from the energy deposit simulation of INGRID scintillator bars). Figure 6.2 shows the average transverse width distributions for muon tracks and EM showers.

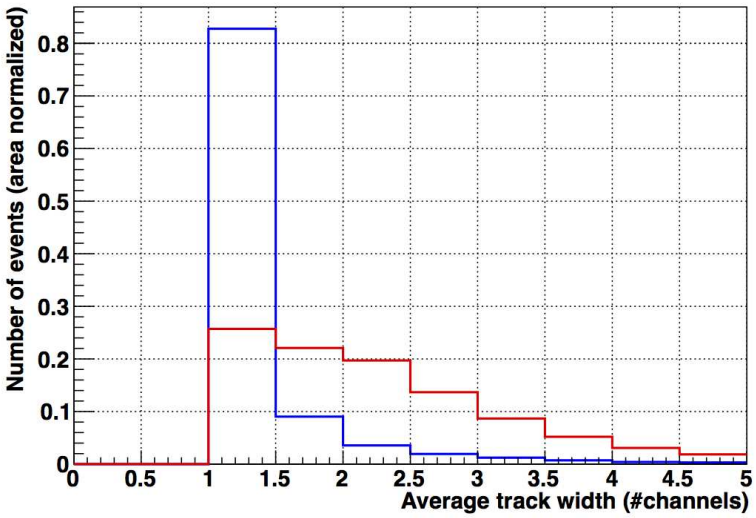

FIGURE 6.2. Transverse width of the track averaged over all tracking planes from MC. The red histogram is for electrons coming from ν_e interactions, the blue histogram for muons coming from ν_μ interactions. Muon tracks are generally not spread over more than one scintillator, whereas electromagnetic showers are spread over several ones.

6.1.2. TRACK LENGTH (I.E. LONGITUDINAL DEPTH). Generally, the electron shower track longitudinal depth is smaller than a muon track due to electron scattering and transverse energy loss. The term "track length" will be used instead of "longitudinal depth" for reconstructed quantities. Figure 6.3 shows the distribution of track lengths. A 20 cm average difference between the two can be observed.

6.1.3. DISPERSION OF THE CHARGE DEPOSITION: ROOT MEAN SQUARE OF $\frac{dE}{dx}$. A muon passing through INGRID acts as a minimum ionizing particle and has a uniform $\frac{dE}{dx}$. On the other hand, the various particles at various energies produced in an EM shower,

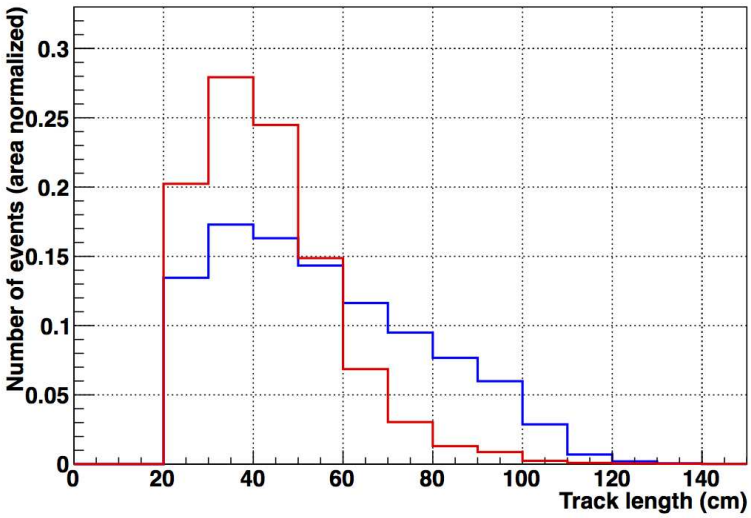

FIGURE 6.3. Track length comparison for electromagnetic showers (red) and muon tracks (blue) from MC.

the $\frac{dE}{dx}$ is expected to change among the hits of the EM shower. The root mean square (RMS) of the $\frac{dE}{dx}$ was chosen for all hits in each track to exploit these differences between EM showers and muon tracks. Figure 6.4 shows the distributions of the $\frac{dE}{dx}$ RMS for muon and electron tracks. It is seen that EM showers have a higher RMS than muon tracks. Only hits separated from the vertex by two or more planes are considered as the uncertainty on energy deposition near the vertex is high due to cross-section model uncertainties.

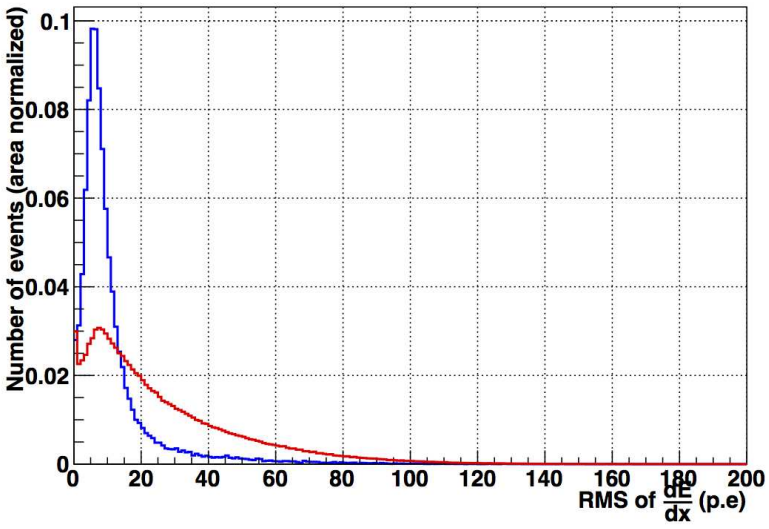

FIGURE 6.4. Root mean square MC distributions for electromagnetic showers (red) and muon tracks (blue). The region around the vertex, defined by a width of ± 2 planes around the reconstructed vertex, and a transverse distance of ± 3 scintillators (15 cm), is excluded from this RMS calculation.

6.1.4. HITS NEAR VERTEX. The large amount of particles produced in an EM shower is used to discriminate between muon tracks ad EM showers. However, the number of hits around a vertex may be highly correlated with the RMS of the RMS of the $\frac{dE}{dx}$. Because of this, only hits that have not been used in the RMS of the $\frac{dE}{dx}$ are used. In contrast to the $\frac{dE}{dx}$ the number of hits is much more robust to cross-section model variations. Figure 6.5 shows the comparison between EM showers and muon tracks and confirms the higher number of hits for EM showers.

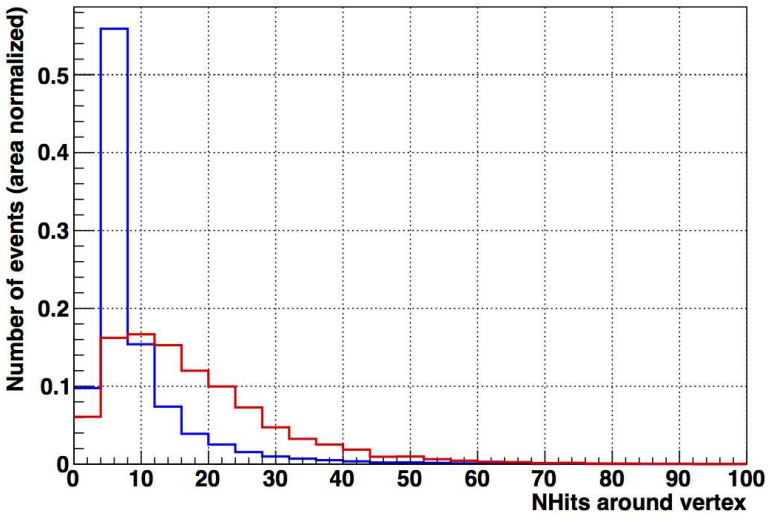

FIGURE 6.5. Distribution of number of hits around the vertex for both electromagnetic showers (red) and muon tracks (blue) from MC. The region around the vertex is defined as ±2 planes around the reconstructed vertex, and a longitudinal distance of 3 scintillators (15 cm).

6.1.5. INGRID SIGNAL SAMPLE AND SYSTEMATIC ERRORS SUMMARY. The ν_μ sample in INGRID is defined as the set of neutrino candidates that are reconstructed with the INGRID original selection and that pass the ν_μ confidence level criterion μ_{CL}. The likelihood is constructed by multiplying the conditional probability of being a muon given the neutrino candidate has different values of the four variables. For a candidate track with track width w, track length l, hit charge distribution q_{RMS}, and number of hits around the vertex n_V, the likelihood is defined as:

(6.1)

$$\mathcal{L}_{\nu_\mu} = P(\nu_\mu|[w, l, q_{RMS}, n_V])$$

(6.2)

$$= \frac{P(w|\nu_\mu) \cdot P(l|\nu_\mu) \cdot P(q_{RMS}|\nu_\mu) \cdot P(n_V|\nu_\mu)}{P(w|\nu_\mu) \cdot P(l|\nu_\mu) \cdot P(q_{RMS}|\nu_\mu) \cdot P(n_V|\nu_\mu) + P(w|\nu_e) \cdot P(l|\nu_e) \cdot P(q_{RMS}|\nu_e) \cdot P(n_V|\nu_e)}$$

$P(w|\nu_\mu)$, $P(l|\nu_\mu)$, $P(q_{RMS}|\nu_\mu)$, and $P(n_V|\nu_\mu)$ are the conditional probabilities of a ν_μ event to have track width w (Figure 6.2), track length l (Figure 6.3), hit charge distribution q_{RMS} (Figure 6.4), and number of hits around the vertex n_V(Figure 6.5). The distribution of this likelihood is shown in Figure 6.6

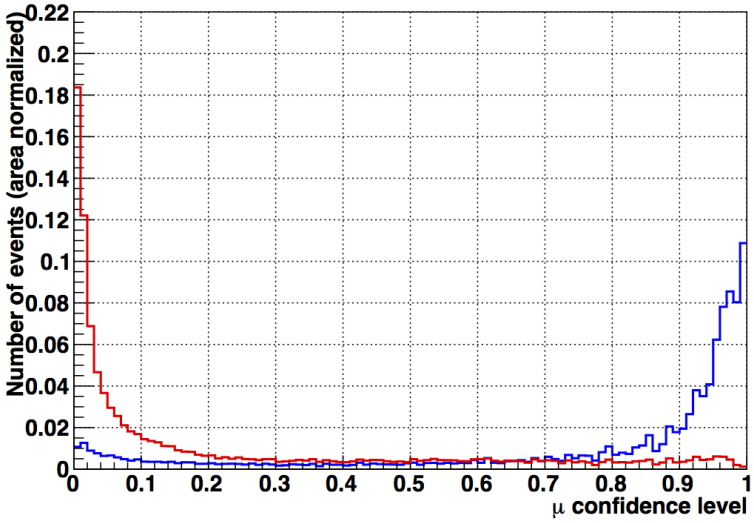

FIGURE 6.6. ν_μ likelihood distributions for ν_μ (blue) and ν_e (red). The confidence level (μ_{CL}) is based on a likelihood ratio obtained from the 4 variables presented before: track length, average transverse width, RMS of the $\frac{dE}{dx}$ and number of hits near the vertex.

A ν_e rejection requirement is used to determine the confidence level μ_{CL}. The optimization of the ν_e rejection requirement is driven only by:

- the need to be able to detect a 3σ deviation from a no-LV signal. In order to be conservative, a 5σ deviation from a no-LV signal was assumed, which induces a larger Lorentz violation effect and, therefore, a larger contamination from electron neutrinos.
- the requirement that the number of reconstructed electron neutrinos be smaller than the muon neutrino statistical error.

In the following, σ_μ (σ_e) is the interaction cross section for ν_μ (ν_e) and ϵ_μ (ϵ_e) is the reconstruction efficiency. The reconstruction efficiency is defined as the probability for a ν_μ induced (ν_e induced) event to be reconstructed and kept as a ν_μ event in the analysis. Letting ν_a^{LV} and ν_a^{Rec} be the number of incident neutrinos after LV oscillation and reconstructed neutrino events of flavor a respectively:

$$\nu_\mu^{\mathrm{Rec}} = \nu_\mu^{\mathrm{LV}} \sigma_\mu \epsilon_\mu \tag{6.3}$$

and

$$\nu_e^{\mathrm{Rec}} = \nu_e^{\mathrm{LV}} \sigma_e \epsilon_e. \tag{6.4}$$

Assuming that all oscillating muon neutrinos oscillate into electron neutrinos, and the ν_μ selection efficiency is 100%, a 5σ signal corresponds to the detection of a number of oscillated muon neutrinos, $\nu_\mu^{\mathrm{Rec,o}}$, corresponding to:

$$\nu_\mu^{\mathrm{Rec,o}} \simeq 5\mathrm{Error}(\nu_\mu^{\mathrm{Rec}}) = 5\sqrt{\nu_\mu^{\mathrm{Rec}}}, \tag{6.5}$$

which, in case of 100% ν_μ reconstruction efficiency, is equivalent to:

$$\nu_\mu^{\mathrm{Int,o}} = 5\sqrt{\nu_\mu^{\mathrm{Int}}}, \tag{6.6}$$

where ν_μ^{Int} and $\nu_\mu^{\mathrm{Int,o}}$ are the number of interacting events in the INGRID fiducial volume, and the number of interacting events in the INGRID fiducial volume that have undergone oscillation, respectively. Again, with the assumption that all ν_μ oscillate into ν_e, *i.e*:

$$\nu_e^{\mathrm{LV}} = \nu_\mu^{\mathrm{LV,o}}, \tag{6.7}$$

with $\nu_i^{\mathrm{Int}} = \sigma_i \nu_i^{\mathrm{LV}}$, $i = e, \mu$ and σ_i the cross section. Assuming that the neutrino cross section of the two species are almost the same in the INGRID energy range

$$\nu_e^{\mathrm{Int}} = \nu_\mu^{\mathrm{Int,o}}, \tag{6.8}$$

Equation 6.6 can be written as:

$$\nu_e^{\mathrm{Int}} = 5\sqrt{\nu_\mu^{\mathrm{Int}}}. \tag{6.9}$$

The second requirement, that the number of reconstructed ν_e be small compared to the uncertainty on ν_μ can be expressed as:

$$\nu_e^{\mathrm{Rec}} \leq \sqrt{\nu_\mu^{\mathrm{Rec}}}. \tag{6.10}$$

Remembering that $\nu_i^{\mathrm{Rec}} = \epsilon_i^{\mathrm{Rec}} \nu_i^{\mathrm{Int}}$, $i = e, \mu$, with $\epsilon_i^{\mathrm{Rec}}$ the reconstruction efficiency of the i-th neutrino species, Equation 6.10 can be written as:

$$\epsilon_e^{\mathrm{Rec}} \nu_e^{\mathrm{Int}} \leq \sqrt{\epsilon_\mu^{\mathrm{Rec}} \nu_\mu^{\mathrm{Int}}}. \tag{6.11}$$

The requirement expressed in Equation 6.9 can therefore be written as:

$$5\,\epsilon_e^{\mathrm{Rec}} \leq \sqrt{\epsilon_\mu^{\mathrm{Rec}}}, \tag{6.12}$$

giving the requirement:

$$\frac{\epsilon_e^{\mathrm{Rec}}}{\sqrt{\epsilon_\mu^{\mathrm{Rec}}}} \leq 0.2. \tag{6.13}$$

The ν_μ confidence level, defined as the ν_μ likelihood value that matches the criterion defined in 6.13 and maximizes the ν_μ reconstruction efficiency, is $\mu_{CL} = 0.54$.

All of the INGRID data taken during T2K Runs 1 - 4 were analyzed. Table 6.1 shows the total number of events passing the selections. Using the new selection, the total number of events is 6.75×10^6.

TABLE 6.1. Number of reconstructed events in the data and MC with the INGRID standard selection and the ν_μ selection.

	Data	MC	$\frac{Data-MC}{MC}$
Standard INGRID selection	8.07×10^6 events	7.92×10^6 events	1.9%
ν_μ selection	6.75×10^6 events	6.57×10^6 events	2.7%

The systematic error associated with this selection is 5.3%. The number of ν_μ candidates shown in Table 6.1 for data and MC are in agreement within the systematic error. As this systematic error does not depend on LSP, the systematic error does not affect the LV analysis.

6.2. ν_μ SELECTION IN ND280

The ND280 LV analysis will use Charged Current inclusive events in the ν_μ disappearance oscillation mode. The selection method described below utilizes the method well described in [17]. An outline of the relevant parts for the LV analysis are provided below.

6.2.1. ν_μ SELECTION IN ND280.

The ν_μ selection method utilizes Charged Current (CC) inclusive neutrino interactions that originate in the P0D and have a negative track that is reconstructed in the first Time Projection Chamber (TPC1). Runs 1 - 4 were analyzed in [17] using production 5 ND280 software. The total number of POT corresponds to $\sim 5.6 \times 10^{20}$. This accumulation of data periods corresponds to configurations of the P0D with the water bags full and with the water bags emptied. Both configurations are used for the LV analysis.

The ν_μ selection method utilizes ν_μ tracks reconstructed by two algorithms and matched by a third algorithm. The two reconstruction algorithms are the P0D and Tracker Reconstruction algorithms. P0D Reconstruction utilizes hits measured in the scintillator bars in the P0D and combines them into either tracks or showers. The Tracker reconstruction reconstructs tracks that pass through the Tracker region of ND280. The Tracker consists of three TPCs and two Fine Grain Detectors (FGDs). The Tracker Reconstruction algorithm uses TPC tracks in the YZ projection to reconstruct tracks from hits in the FGDs. For reconstructed tracks in the XZ projection, an initial time called T0 is taken from either the matched FGD hits or one of the surrounding subdetectors (such as the P0D, barrel ECal, or P0D ECal). More information on P0D and Tracker Reconstruction can be found in T2K-TN-072 [18]. The third algorithm matches the tracks produced by the two reconstruction packages. The track matching algorithm is described briefly below.

6.2.1.1. *Tracker-to-P0D Matching Algorithm.* The track matching algorithm utilizes the outputs of the P0D and Tracker Reconstruction packages to match tracks together. These tracks, in general, are not necessarily ν_μ tracks. A separate algorithm analyzes the group of candidate tracks to check if they are ν_μ events or not. The matching algorithm takes P0D tracks that occur in the downstream portion of the P0D and matches them to Tracker tracks that occur in the most upstream portion of the Tracker (specifically TPC1). For brevity, the Tracker-to-P0D Matching algorithm is referred to as the T2P algorithm. The T2P algorithm can be described with two stages. The first stage scans the outputs of P0D and Tracker Reconstruction, the second stage generates a list of pair-candidate tracks for further analysis.

In the first stage of the T2P algorithm, the output tracks from the reconstruction packages are required to pass quality, position, and a time window check of $\pm$ 100ns of each other.

The time window check allows for rejection of tracks from different bunches. The P0D track position and quality checks are

- Last node Z-position > -1016mm or last two P0Dules. This ensures the track passes through the downstream portion of the P0D.
- A 3D track is required by only allowing tracks with position variance $(X_{var}, Y_{var}, Z_{var})$ less than 10^8mm.
- Sort the track nodes in order by Z.

The tracker track position and quality checks are::

- The first node Z-position < -700mm. This ensures the track starts in the upstream portion of TPC1.
- The track should have more than 18 nodes.
- Sort the track nodes in order by Z.

In the second stage of the T2P algorithm, all possible pair-candidate tracks are identified. The algorithm then creates a list of pair-candidates from all combinations resulting from the output of the first stage. The algorithm then collects information about each candidate pair. Two matching parameters ΔR and $\sin\Delta\theta$ are used to match the P0D and TPC pieces together. ΔR is the radial distance in the XY plane between the most downstream P0D track node and the linear projection of the Tracker track into the P0D at the same Z-position as the last P0D track node. $\Delta\theta$ is the angle between the last P0D track node direction and the Tracker track direction. Fig. 6.7 shows a schematic of these matching parameters.

Finally, the algorithm sorts out pair-candidates which did not satisfy a set of optimized matching parameter requirements. These matching parameter requirements were chosen

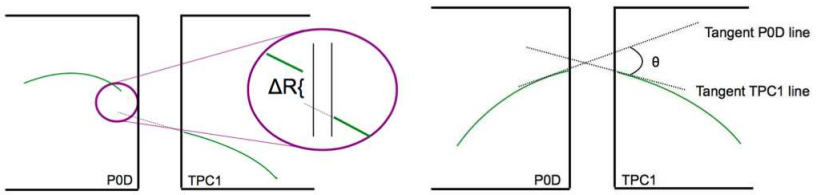

FIGURE 6.7. Diagrams of the ΔR and $\sin\Delta\theta$ matching parameters.

based off a figure of merit for a range of cut values. The figure of merit is

$$F = \frac{S}{\delta S} \tag{6.14}$$

where S is the number of signal events and δS is the corresponding error. The pair of matching parameters that maximizes F are

- $\Delta R < 76$mm
- $\sin\Delta\theta < 0.86$

These cut values are what the T2P algorithm uses for each candidate pair. The T2P algorithm ensures that any P0D or Tracker track is only used once in a bunch.

6.2.1.2. ν_μ *Event Selection.* For a neutrino interacting via the CC channels, the outgoing lepton will contain the majority of the incident neutrino momentum. To search for candidate event tracks from the pair-candidate tracks described above, the highest momentum negative T2P track in an ND280 event is sought after. The event selection flow utilizes information from different levels:

Accelerator/Near-Complex level

- The beam/accelerator flag "GoodSpillFlag" is set to the value of one. This flag signals that there were no problems with that particular spill on the beam/accelerator side.

- The near detector-complex Data-Quality flag "ND280OffFlag" is set to the value of zero. This flag signals that all the different sub-detectors of ND280 reported being on and functional with no problems.

Track level

- Apply the T2P algorithm as described above

Bunch level

- All output tracks from the T2P algorithm are sorted into predefined bunch time windows
- Only an active bunch that passes the "Tracks Veto" check is considered. The "Tracks Veto" check is designed to reject events with reconstruction failures (more detail in [17])
- Identify the muon candidate track and tag that event as a CC interaction

A track is considered to be a muon candidate if the following are satisfied:

- The candidate track charge is negative as indicated by the Tracker track charge property
- The candidate track begins in the P0D volume in order to reject external source tracks
- The candidate track momentum is the highest in the bunch

6.2.2. ND280 Signal Sample and Systematic Errors Summary. Table 6.2 breaks down the number of ν_μ events using the above procedure for water-in and water-out configurations of the P0D:

Table 6.3 - 6.4 summarizes the systematic errors for CC event analysis is provided below for the water-in and water-out configurations of the P0D:

TABLE 6.2. Neutrino events for water-in and water-out P0D configurations

Run	POT[$\times 10^{19}$]	Events
1+2+4(water-in)	23.48	28,143
2+3+4(water-out)	32.89	27,389
Total		55,527

TABLE 6.3. Systematic Error sources for Water In

Systematic Source	
P0D Tracking and Matching Efficiency	$^{+0.0045}_{-0.0045}$
Fiducial Mass	$^{+0.0062}_{-0.0062}$
Fiducial Volume	$^{+0.0030}_{-0.0073}$
Out of P0D FV	$^{+0.0041}_{-0.0041}$
Beam-Sand Interference	$^{+0.0119}_{-0.0116}$
TPC1 Tracking Efficiency	$^{+0.0016}_{-0.0016}$
Charge Mis-ID	$^{+0.0068}_{-0.0068}$
Total Det. Sys.	$^{+0.0166}_{-0.0177}$

TABLE 6.4. Systematic Error sources for Water Out

Systematic Source	
P0D Tracking and Matching Efficiency	$^{+0.0054}_{-0.0054}$
Fiducial Mass	$^{+0.0086}_{-0.0087}$
Fiducial Volume	$^{+0.0026}_{-0.0003}$
Out of P0D FV	$^{+0.0049}_{-0.0049}$
Beam-Sand Interference	$^{+0.0138}_{-0.0144}$
TPC1 Tracking Efficiency	$^{+0.0014}_{-0.0014}$
Charge Mis-ID	$^{+0.0065}_{-0.0065}$
Total Det. Sys.	$^{+0.0192}_{-0.0195}$

As these sources of systematic error are not time dependent, they do not affect the ND280 LV analysis and are thus neglected.

CHAPTER 7

Systematic Uncertainties

The systematic uncertainties that could affect this LV analysis are broken up into two categories:

(1) Time dependent detector sources

(2) Time dependent beam sources

For both detectors, the time dependent detector sources include neutrino event pile-up, MPPC dark noise, and MPPC gain variation. Each source is evaluated in both detectors using similar methods. Additionally, for both detectors, the time dependent beam sources include beam alignment over a given run and beam alignment within one run. Each source is evaluated in both detectors. Finally, a residual rate correction that corrects for non-uniform coverage of the POT in LSP is evaluated and applied to every data set. Corrections for each source are extracted and applied to each data set.

7.1. Time Dependent Detector Systematics

In both INGRID and ND280, there exist detector effects that vary in time which could introduce a spurious modulation in the ν_μ rate versus LSP, mimicking an LV signal. It is important to take these detector effects into account for each T2K near detector. The following time-dependent detector effects will be studied:

- Neutrino event pile-up
- MPPC dark noise
- MPPC gain variation

As the neutrino beam intensity increases, the likelihood of having more than one neutrino event occur in a detector increases. This is known as neutrino event pile-up. If multiple events occur in one electronic cycle, one of the two events will be missed and cause distortions in the neutrino event rate distribution which can mimic a LV signal. External conditions, such as day/night temperature variations, will cause the dark noise rate to vary in each detector. This variation affects the detection of the neutrino events and may mimic a LV signal. Finally, the charge value of the average minimum ionizing peak (MIP) changes with the T2K data taking time. This change affects the MPPC gain and, consequentially, the event reconstruction and selection. Variations in these charges values throughout a given T2K run can mimic a LV signal.

7.1.1. Neutrino event pile-up in INGRID. The INGRID reconstruction is tuned to reconstruct a single vertex in a given electronic cycle (580ns). If multiple events occur in one electronic cycle, one of the two events will be missed. As the neutrino beam intensity increases, one expects this effect to cause greater and greater distortions in the neutrino event rate distribution which can mimic an LV signal. Because of this, the beam intensity variation in LSP is studied.

Using all beam spills analyzed in this analysis, Figure 7.1 shows the POT per bunch vs LSP. A significant variation (5% maximally) above statistical error is observed which says that the event pile-up must be taken into account.

The event loss decreases linearly with beam intensity and is given by:

$$\mathrm{Nevents}_{\text{Pile-up corrected}} = \frac{\mathrm{Nevents}}{1 - \mathrm{C}_{\mathrm{loss}}\mathrm{n}_{\mathrm{ppb}}} \tag{7.1}$$

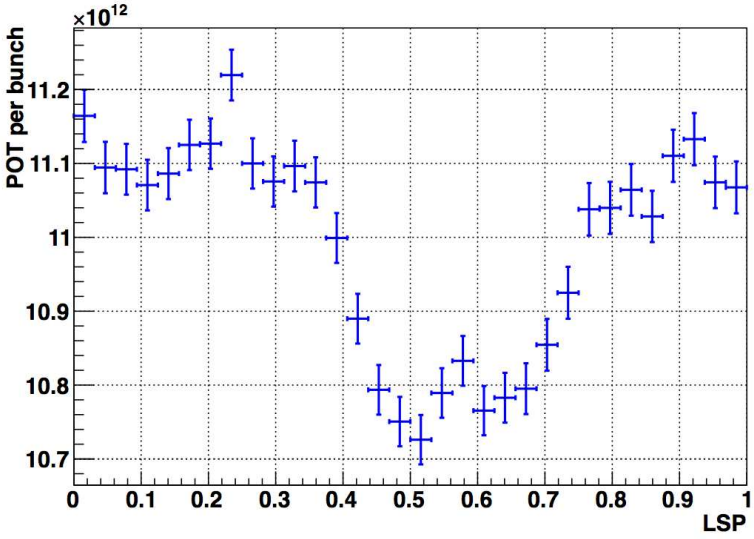

FIGURE 7.1. POT per bunch variation with LSP using T2K run 1 to run 4 data.

TABLE 7.1. Event loss constant estimated in [2] for a 250 kA horn current, using the standard INGRID selection for Run 1 to 3. The statistical error on each constant is 0.05×10^{-15}.

Horizontal modules	0	1	2	3	4	5	6
$C_{loss} \times 10^{15}$	0.87	1.06	1.13	1.22	1.32	1.22	0.92
Vertical modules	7	8	9	10	11	12	13
$C_{loss} \times 10^{15}$	0.81	1.00	1.05	1.22	1.19	1.09	0.71

where C_{loss} is the event loss constant and n_{ppb} the number of POT per bunch (i.e. the beam intensity) that is shown in Figure 7.1.

The event loss constant for 250kA horn current has already been determined for each INGRID module. These values are summarized in Table 7.1, with the INGRID module numbering shown in Figure 7.2.

For a given number of POT per bunch, the appropriate correction is applied to each neutrino event. The systematic error associated with this correction is obtained from the statistical error on the event loss variation (0.05×10^{-15}). This represents an event loss variation of $3\% - 7\%$ depending on the INGRID module. Figure 7.3 shows the correction

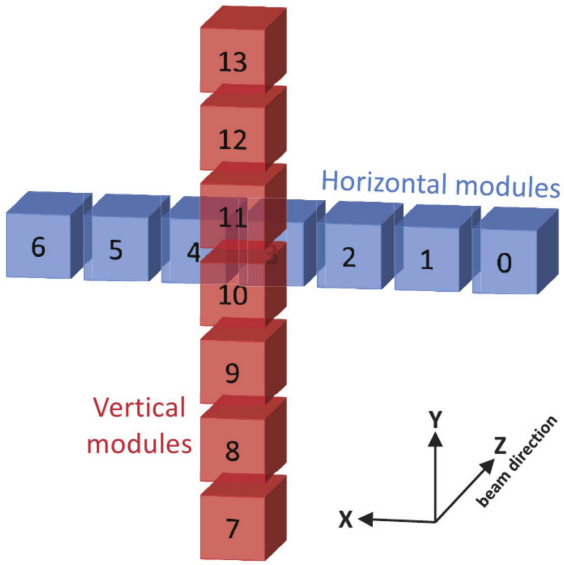

FIGURE 7.2. INGRID modules numbering.

that need be applied to the ν_μ event rate LSP distributions in addition to the $\pm 1\sigma$ variation for the INGRID central horizontal module.

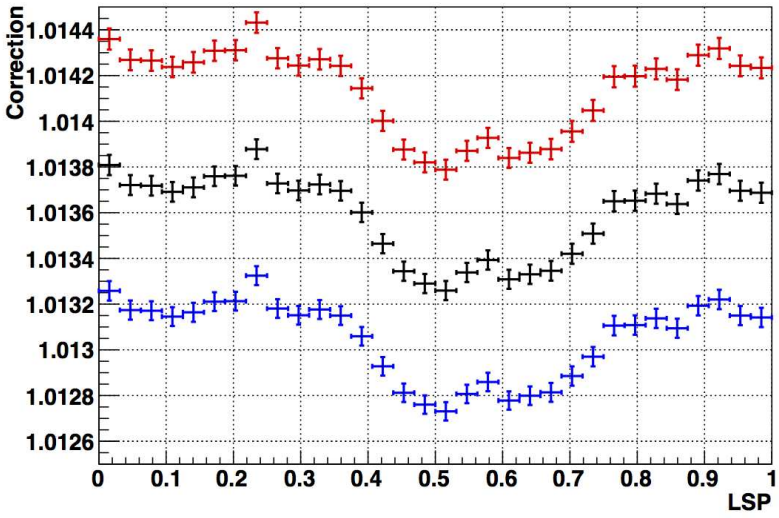

FIGURE 7.3. Correction of the number of events per POT as a function of the local sidereal phase in the INGRID horizontal central module (module 3). The associated event loss constant is $C_{loss} = 1.22 \times 10^{-15}$. The $+1\sigma$ (red) and -1σ (blue) variations correspond to variations of the event loss constant within its statistical error of 0.05×10^{-15}.

An overall correction of $\sim 1.3\%$ to the event rate is found. This correction has no impact on this study as it only effects the total rate of ν_μ candidates vs LSP in INGRID. The variation in shape of the distribution is less than 0.1%. This is 0.1% of a 1% effect which is $< 0.01\%$, thus making this error negligible when compared to the statistical error ($\sim 0.3\%$). It is assumed here that the event loss constant does not change with the ν_μ selection as compared to the standard INGRID selection, which is motivated by fact that the vertex reconstruction efficiency is little affected by the ν_μ confidence level cut.

A plot of the ν_μ rate versus LSP after the pile-up correction has been applied is shown in Figure 7.4.

7.1.2. NEUTRINO EVENT PILE-UP IN ND280. In ND280, it is assumed there is an equal probability for a neutrino interaction to occur in each beam spill. From this, the probability for a given spill to contain more than one reconstructed neutrino event is given by

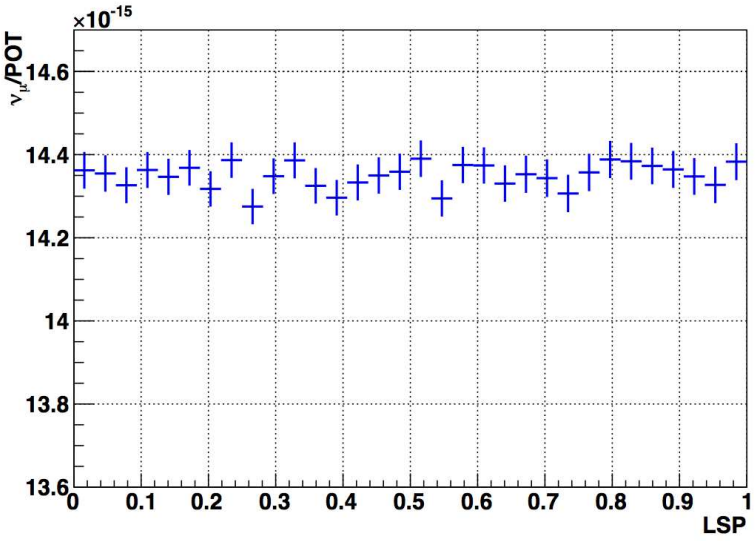

FIGURE 7.4. ν_μ rate versus LSP distribution in INGRID after pile-up corrections have been taken into account.

$$P_{\text{pile-up}} = \frac{\text{Total number of spills with} > 1 \text{ neutrino event}}{\text{Total number of spills in run}} \tag{7.2}$$

This probability was calculated for each individual run, and for the water-in and water-out configurations of the P0D. The values are provided in the Table 7.2 - 7.3. Because, for each run, the probability for pile-up is small, no correction was evaluated for ND280.

TABLE 7.2. Probability of more than one reconstructed neutrino event in ND280 Water-in sample.

	Run1 Water	Run2 Water	Run4 Water	Total Water-in
$P_{\text{pile-up}}(\%)$	0.0003	0.003	0.005	0.003

TABLE 7.3. Probability of more than one reconstructed neutrino event in ND280 Water-out sample.

	Run2 Air	Run3 Air	Run4 Air	Total Water-out
$P_{\text{pile-up}}(\%)$	0.0004	0.002	0.003	0.002

7.1.3. MPPC DARK NOISE IN INGRID. In the INGRID electronics, external conditions will cause the dark noise rate to vary. The dark noise rate will vary within a given T2K data taking period. This variation affects the detection of the neutrino events in INGRID and may mimic on LV signal in the event rate vs LSP distributions. Therefore, the effect of the dark noise rate on the INGRID LV analysis must be studied. Using Monte Carlo (MC) samples, this effect on the ν_μ detection efficiency is calculated. From this, a MC-driven correction in each LSP bin may be applied which will equalize the detection efficiency across the whole LSP phase space. As this correction only changes the overall normalization of the ν_μ event rate vs LSP, the correction will leave the shape of the distribution unaffected. However, uncertainties in the dark noise rate variation could distort the LSP distributions and thus must be studied.

The dark noise rate is estimated by using the off-beam INGRID Trip-T integration cycles. In each integration cycle, the number of hits is collected and the mean of the fitted Poisson distribution is used (Figure 7.5).

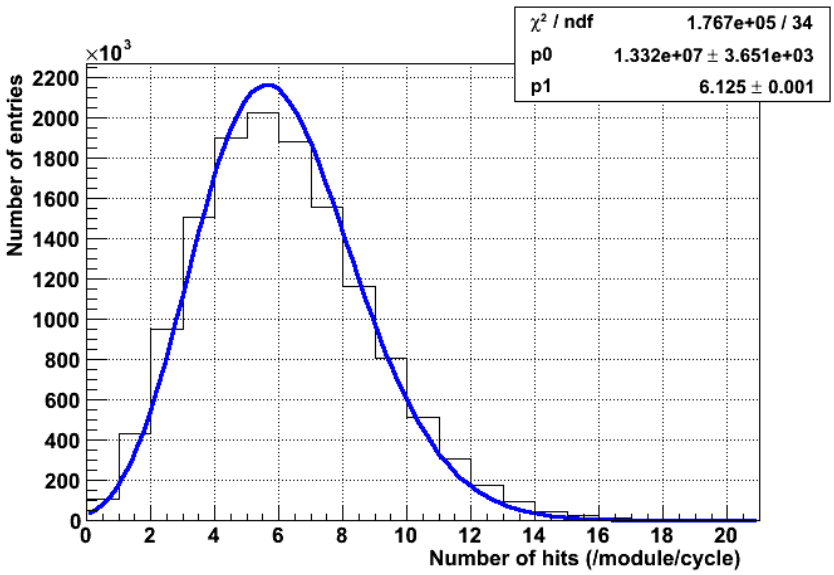

FIGURE 7.5. Distribution of the dark noise rate per INGRID module and per cycle for a given time interval. It is fitted by a Poisson distribution.

To estimate the effect on the ν_μ per POT shape variations, 21 toy MC experiments are generated with the dark noise rate varying from 0 to 10 hits for each cycle per module in steps of 0.5. Figure 7.6 shows the impact on the ν_μ efficiency. By fitting this distribution with a linear function (Equation 7.3), the variation of the efficiency with the dark noise rate is obtained.

$$\epsilon_{\nu_\mu} = a \times \text{DN rate} + b, \tag{7.3}$$

with:

$$a = -(5.59 \pm 0.06) \times 10^{-4} \text{ and } b = 0.44290 \pm 0.00003. \tag{7.4}$$

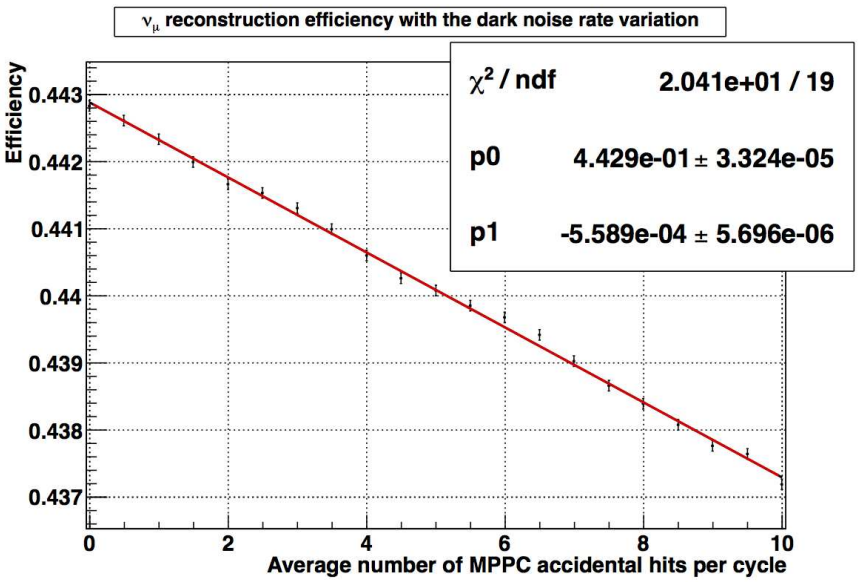

FIGURE 7.6. Variation of ν_μ selection efficiency with the dark noise rate in MC. Because of mis-reconstruction, the efficiency naturally decreases with the dark noise rate. This variation is fitted with a 1st degree polynomial and the associated equation found is $-5.6 \times 10^{-4} \times$ DN rate $+ 0.4429$.

Figure 7.7 (top) shows the dark noise rate with LSP. The correction is obtained by taking the ratio of the ν_μ efficiency in a given LSP bin, calculated from the dark noise rate in Figure 7.7 (top) and Equation 7.3, to the efficiency corresponding to a MC dark noise rate of 5.05 hits per cycle per module.

The bottom part of Figure 7.7 shows this result, together with the corresponding $\pm 1\sigma$ errors MC statistical errors on the fitted coefficients (shown in Equation 7.4).

The shape correction varies between 1.00138 and 1.00124. This gives a relative variation of ~ 0.01. From this, the MC correction has a negligible impact on the event rate vs LSP distributions. The $\pm$ 1 σ variations of the fitted coefficients shown in Figure 7.7

Given the negligible effect of the $\pm 1\sigma$ variations of the fitted coefficients, no systematic error is assigned to this correction. No module by module study has been performed as this correction is small.

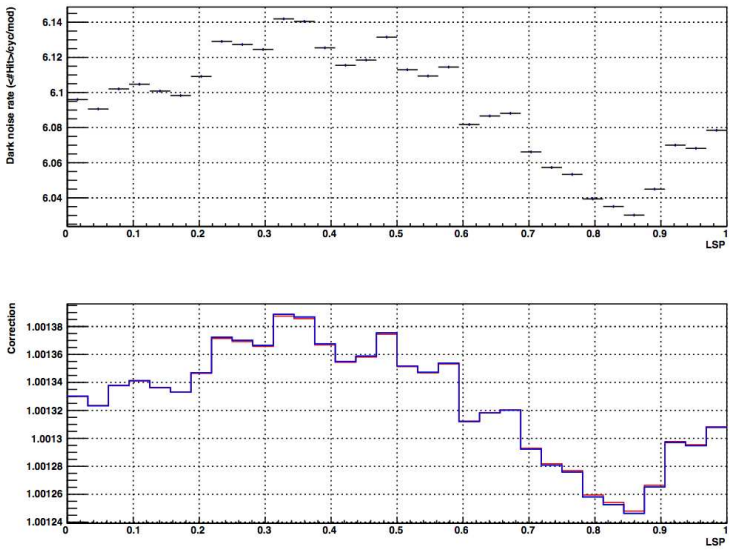

FIGURE 7.7. Variation of the dark noise rate with the local sidereal phase (top). The associated correction on the number of events is shown in the bottom figure, along with the $+1\sigma$ (red) and -1σ (blue) variations. The rate average correction is not equal to 1, since a dark noise rate of 5.05 hits per cycle per module is assumed in the MC. In order to retrieve the correct time independent number of interacting events, an average correction is therefore to be applied to the number of events (or efficiency) which is the correction averaged over LSP. Note: $+1\sigma$ represents the largest dark noise effect, in which b is overestimated by 1σ and a underestimated by 1σ. On the opposite, -1σ represents the flattest variations of the efficiency with dark noise, *e.g* b is underestimated by 1σ and a overestimated by 1σ.

Figure 7.8 shows the ν_μ rate versus LSP after the event pile-up and MPPC dark noise correction have been applied.

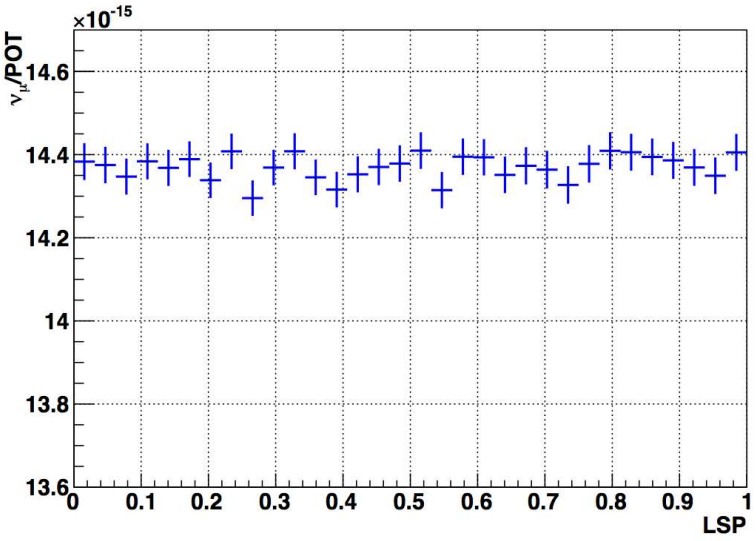

FIGURE 7.8. ν_μ rate versus LSP distribution after pile-up and MPPC dark noise corrections have been taken into account in INGRID.

7.1.4. MPPC DARK NOISE IN ND280. The selection used for ND280 matches P0D specific track pieces to TPC1 specific track pieces. From this, every TPC1 matched P0D track is a minimum of 8 P0Dules (16 nodes). The P0D Reconstruction software package has a minimum node requirement of 4 in order for the package to reconstruct a given track. As the ND280 selection utilizes this package (among others), all matched tracks in the ND280 selection pass this minimum node requirement. Now, the dark noise rate in the P0D for a given integration window is $\approx$ 70 hits. This value assumes that there is no dark noise cleaning or timing cuts, of which there are both in the P0D. It is highly unlikely that a set of hits due to dark noise will add or subtract more than one node. Assuming the dark noise rate adds or subtracts one node from a given matched track, 17 or 15 nodes are left in each matched track. This still passes the minimum node requirement in P0D Reconstruction. Thus, no tracks are lost or gained due to dark noise and this effect does not impact the ND280 LV analysis. No correction was calculated because of this.

7.1.5. MPPC Gain Variation in INGRID. The charge value of the average minimum ionizing peak (MIP) changes with the T2K data taking time. This change will impact the reconstruction, where only hits with more than 2.5 photo-electrons in a scintillator layer are used, and the ν_μ selection as the RMS of dE/dx is used in the INGRID selection. A module by module study was performed since the temperature conditions between all the modules is not uniform. To illustrate this, the MIP variation with T2K data taking period is shown in Figure 7.9 for the edge module (number zero) to the central module (number three).

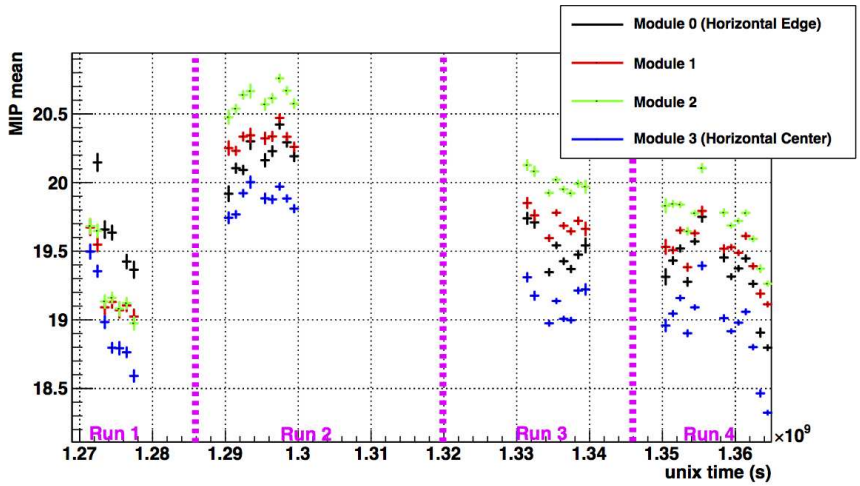

Figure 7.9. MIP distribution as a function of time in INGRID data. Different INGRID horizontal modules from number zero to three are shown, along with the different T2K run periods. The MIP is evaluated by fitting the sand muon charge distribution with a gaussian function around the muon mean charge deposition value.

Due to the time dependence of this effect on the number of neutrino events, it is important to investigate how this effect impacts the event rate versus LSP distributions. Figure 7.10 shows the MIP variation as a function of LSP for module three.

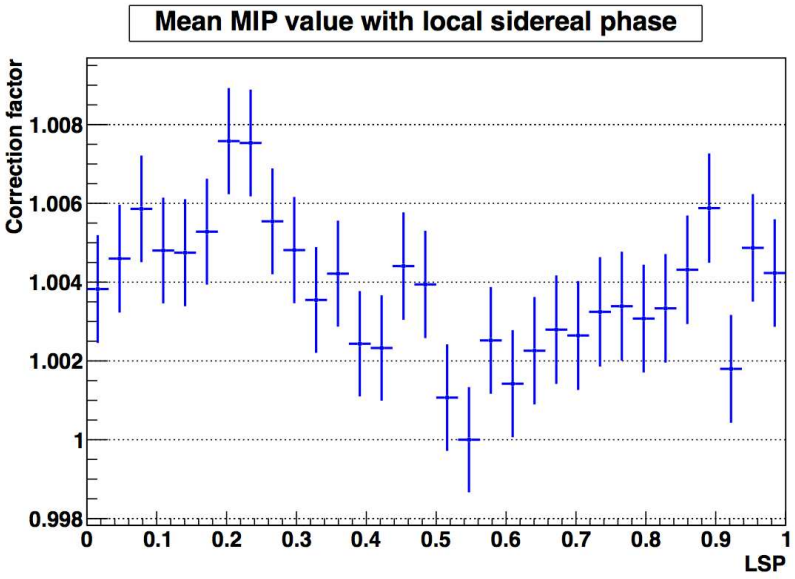

FIGURE 7.10. MIP distribution as a function of the local sidereal phase for the horizontal central module from INGRID data. The MIP value was normalized to the lowest MIP of the horizontal central module. One observes the latter is located at the end of run 4 (see Figure 7.9).

There is a significant effect above statistical error that can be observed in the sand muon sample which is used to determine the MIP variation. Data is used to determine this correction because low charge hits are not well simulated in the MC. A correction factor was determined for each module and time period from Figure 7.9. The lowest MIP value over the entire T2K running period is used as reference. Specifically, the charge of each hit is scaled by a factor that is dependent upon the module and time period F(mod., t):

$$Q_{Hit}^{cor} = Q_{Hit}/\mathrm{F(mod.,\ t)}, \tag{7.5}$$

where F(mod., t) is the MIP value for the module "mod" at time "t" divided by the MIP lowest value for module "mod" (both are shown in Figure 7.9). From 7.5 it is found that $F \geq 1$ and $Q_{Hit}^{cor} \leq Q_{Hit}$. With this, the data are reconstructed and the INGRID ν_μ selection is applied. Figure 7.11 shows the comparison with the nominal data sample (no MIP/gain

correction applied). Since a lower gain implies a lower noise level, and lower dE/dx dispersion that increases both the reconstruction and the ν_μ selection efficiencies, a higher ν_μ rate after the gain correction is applied can be observed.

The bottom part of Figure 7.11 shows the impact on the shape to be within the data statistical variation. No systematic uncertainty is therefore associated with the MIP variation.

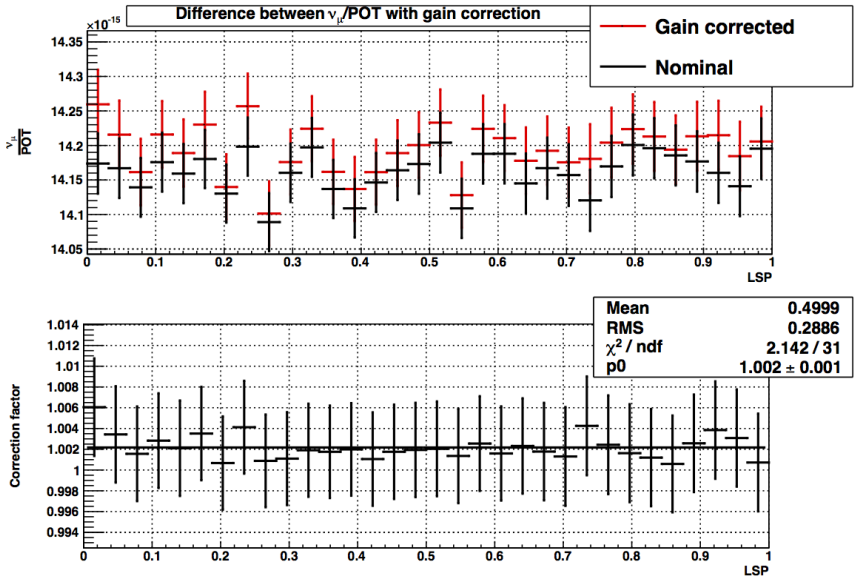

FIGURE 7.11. (Top) Comparison between the nominal distribution of the ν_μ per POT with LSP and the same distribution after applying the gain correction. A constant function is fitted to the (corrected/uncorrected) ratio which is shown on the bottom. The small $\chi^2/NDF = 0.07 \ll 1$ value indicates that this ratio is time independent.

Figure 7.12 shows the ν_μ rate versus LSP after the pile-up, MPPC dark noise and MPPC gain corrections have been applied.

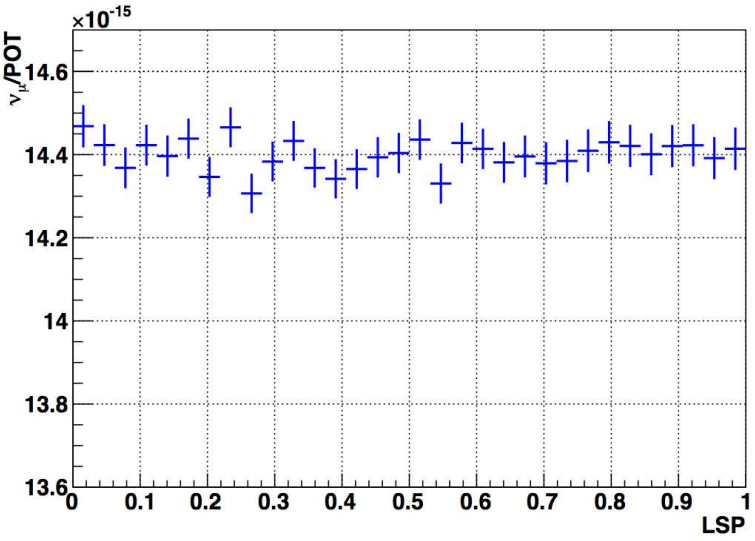

FIGURE 7.12. ν_μ rate versus LSP distribution in INGRID after pile-up, MPPC dark noise, and MPPC gain corrections have been taken into account.

7.1.6. MPPC GAIN VARIATION IN ND280. P0D Reconstruction has a minimum amount of photo-electrons (P.E.) for a given hit to be reconstructed. This minimum amount is 8 P.E. Figure 7.13 shows that the minimum track node charge for runs 1 - 4 is about 20 P.E.

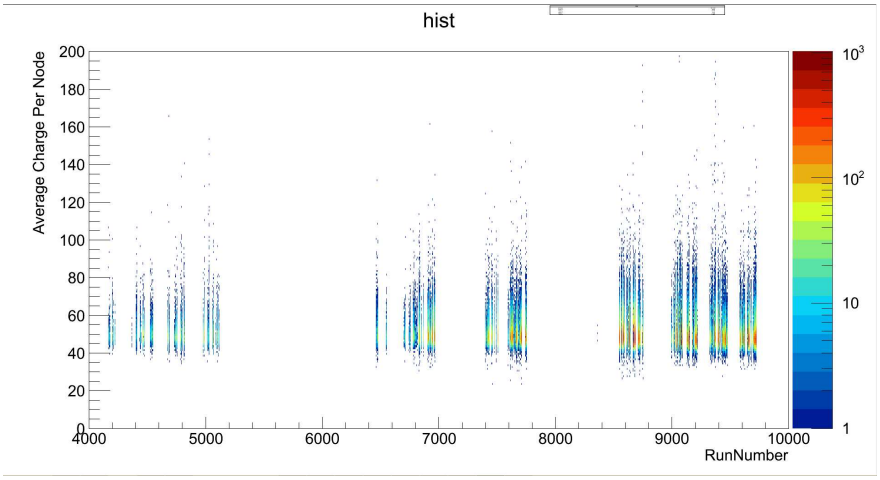

FIGURE 7.13. Amount of charge per node for a given Run Number in the P0D.

From the P0D calibration group, gain variations in the P0D for a given run across all channels amount to 1 - 2%. If a particular track were to vary maximally, the hits would still

be reconstructed by P0D Reconstruction. Thus, the MPPC gain variation in the P0D does not affect the ND280 LV analysis and no correction is calculated.

7.2. Time Dependent Beam Effects

It is possible that variations between the number of protons on target (POT) and the neutrino flux can give rise to differences which may mimic a LV effect. In particular, the proton beam alignment can vary with time and impact the neutrino flux. Because of this, the number of ν_μ per POT should be corrected to account for the real neutrino flux without any LV effects at INGRID and ND280. Here, the change in beam alignment at each detector is studied. To perform this study, data were analyzed in two ways:

- For each T2K run 1 - 4, the beam position is determined using each near detector. This reduces possible systematic errors by determining the beam position in the detector where LV effects will be studied.
- Within a given run, the statistics is too small to determine the beam position directly from the near detectors. In this case, the Muon Monitor (MuMon) is used to calculate rate corrections. Using the MuMon will mitigate, among other sources, tidal effects that are known to change the beam position.

7.2.1. Run by Run Beam Position at INGRID. On a run by run basis, the ν_μ selection is applied to each of the fourteen modules in INGRID. Using a gaussian fit on the number of neutrino interactions in each module, the beam position may be independently determined. Figure 7.14 to 7.17 shows the results of performing this procedure. The beam position varies between 3.0cm to 3.9cm horizontally and -5.5cm to 8.9cm vertically in INGRID.

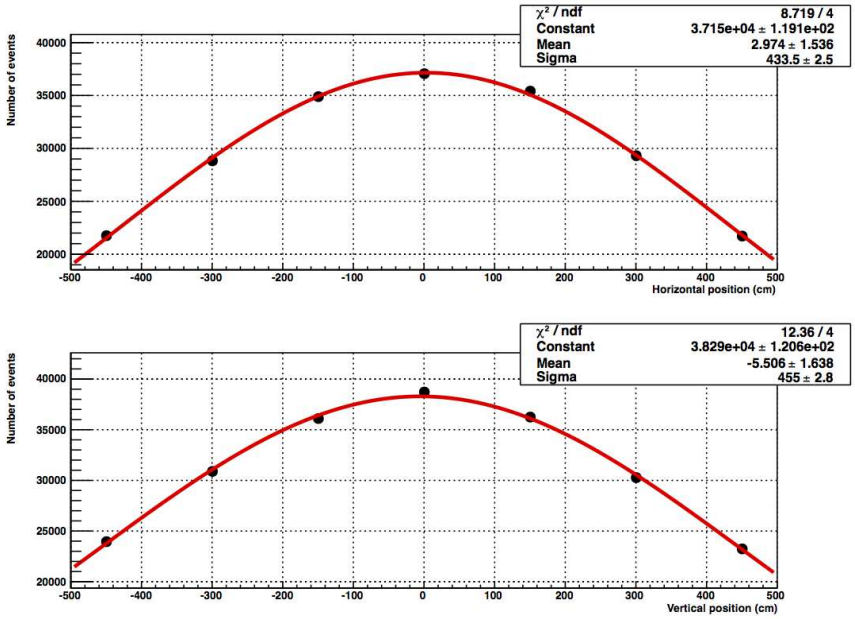

FIGURE 7.14. The ν_μ horizontal and vertical beam profiles for T2K run 1 in INGRID.

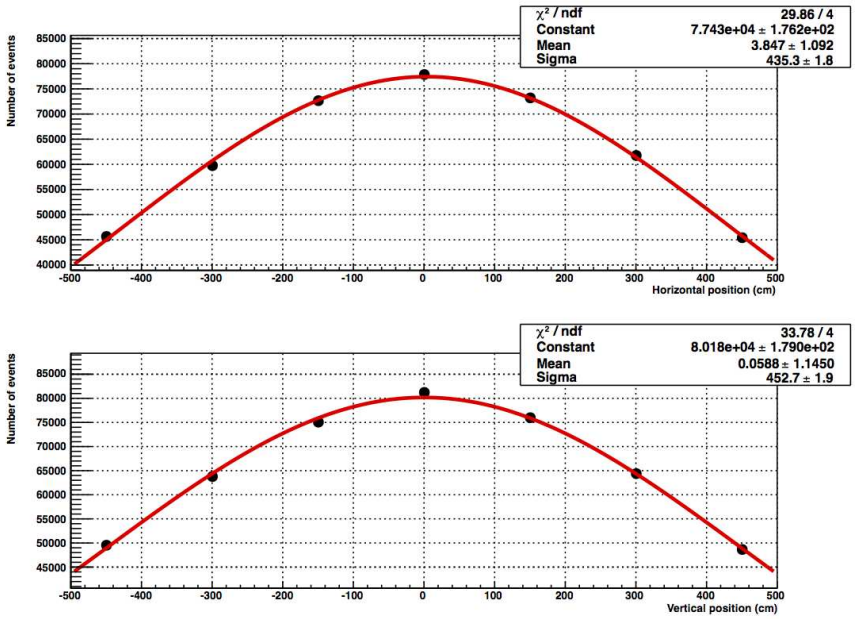

FIGURE 7.15. The ν_μ horizontal and vertical beam profiles for T2K run 2 in INGRID.

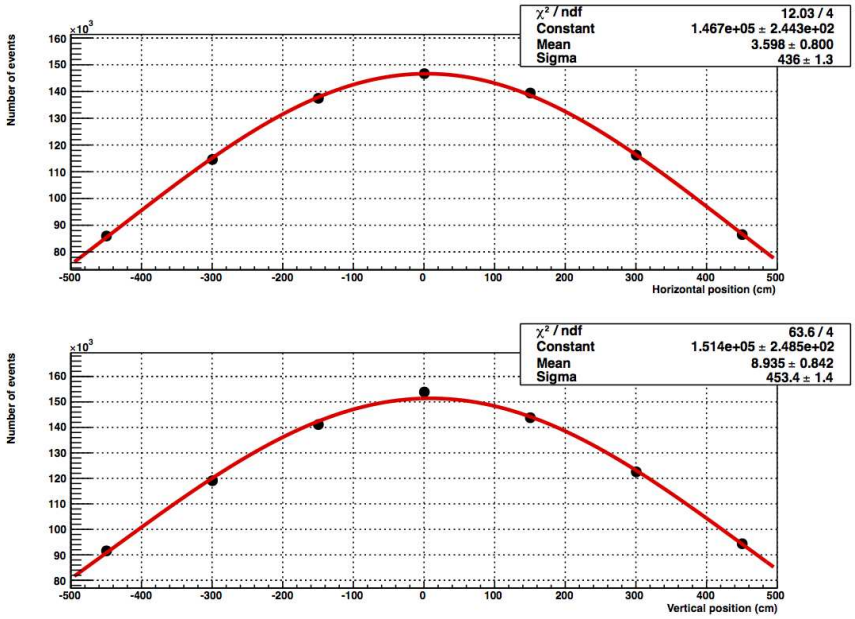

FIGURE 7.16. The ν_μ horizontal and vertical beam profiles for T2K run 3 in INGRID.

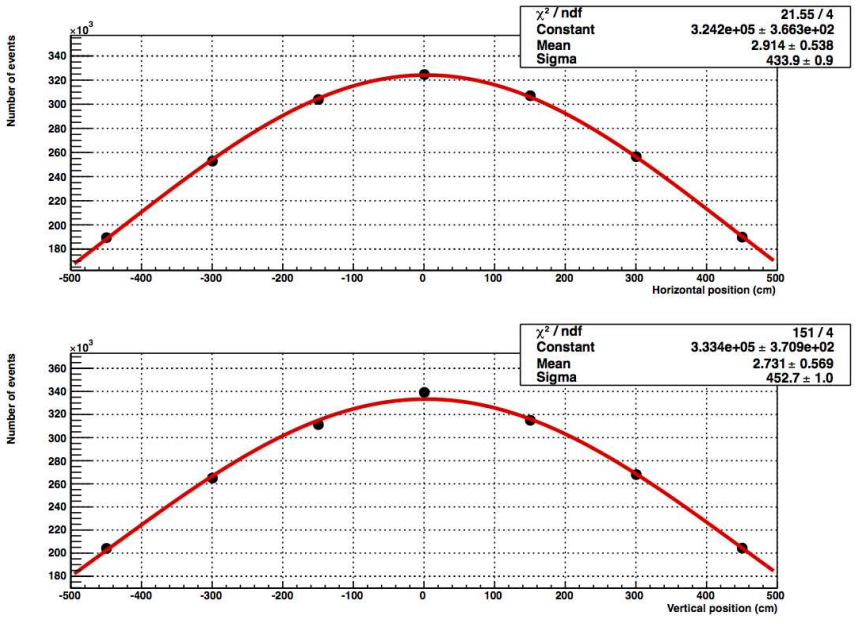

FIGURE 7.17. The ν_μ horizontal and vertical beam profiles for T2K run 4 in INGRID.

7.2.2. Run by Run Beam Position at ND280. ND280 is unable to evaluate the Run by Run beam position.

7.2.3. Beam Position Variation within One Run at INGRID. The Silicon Pixel portion of the MuMon detector was used to correct the beam position wihtin one T2K run. This portion of the detector provides the highest accuracy on the beam position [19]. The muon beam position is measured in MuMon as a function of LSP for each neutrino spill used in the LV analysis. For kinematic reasons, the muon beam center is aligned with the neutrino beam center. A geometric scaling factor is applied to extrapolate the neutrino beam center at INGRID from MuMon data:

$$\mathrm{Pos}_{X/Y}^{\mathrm{INGRID}} = \mathrm{Pos}_{X/Y}^{\mathrm{MuMon}} \times \frac{280}{115} \tag{7.6}$$

7.6 is the ratio of the INGRID and MuMon distance in meters from the target. Figure 7.18 to Figure 7.24 shows the extrapolated beam position variation in INGRID for the horizontal coordinate while Figure 7.19 to 7.25 is for the vertical coordinate.

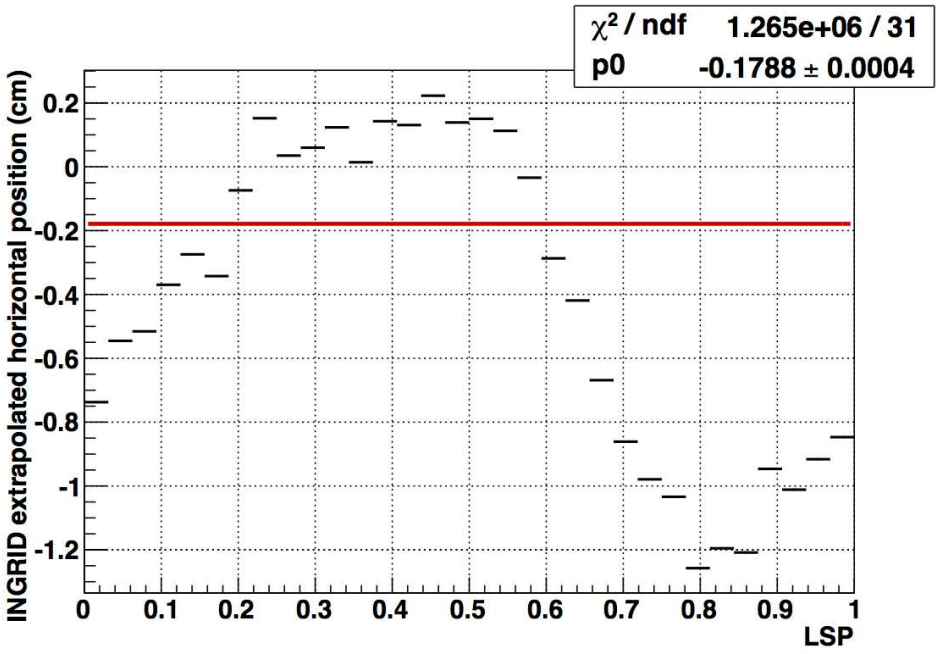

FIGURE 7.18. ν_μ beam horizontal beam positions in the Silicon pixel part of the MuMon for T2K Run 1.

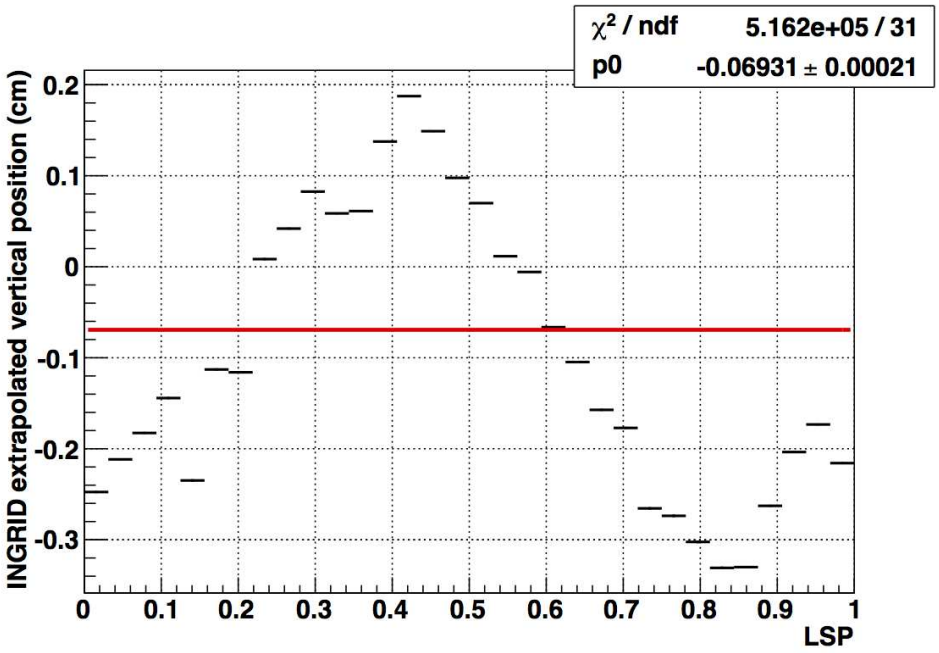

FIGURE 7.19. ν_μ beam vertical beam positions in the Silicon pixel part of the MuMon for T2K Run 1.

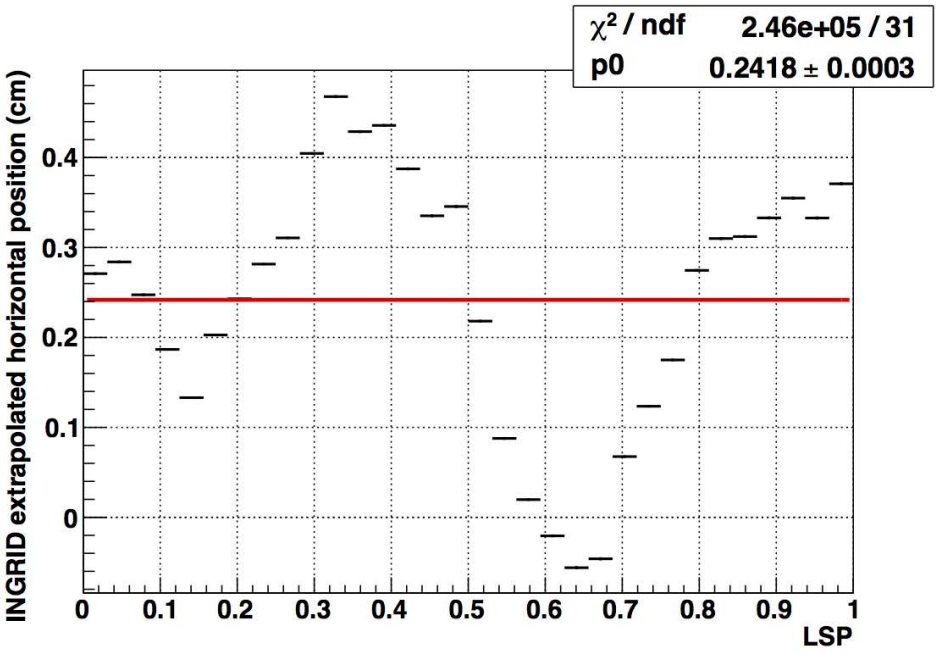

FIGURE 7.20. ν_μ beam horizontal beam positions in the Silicon pixel part of the MuMon for T2K Run 2.

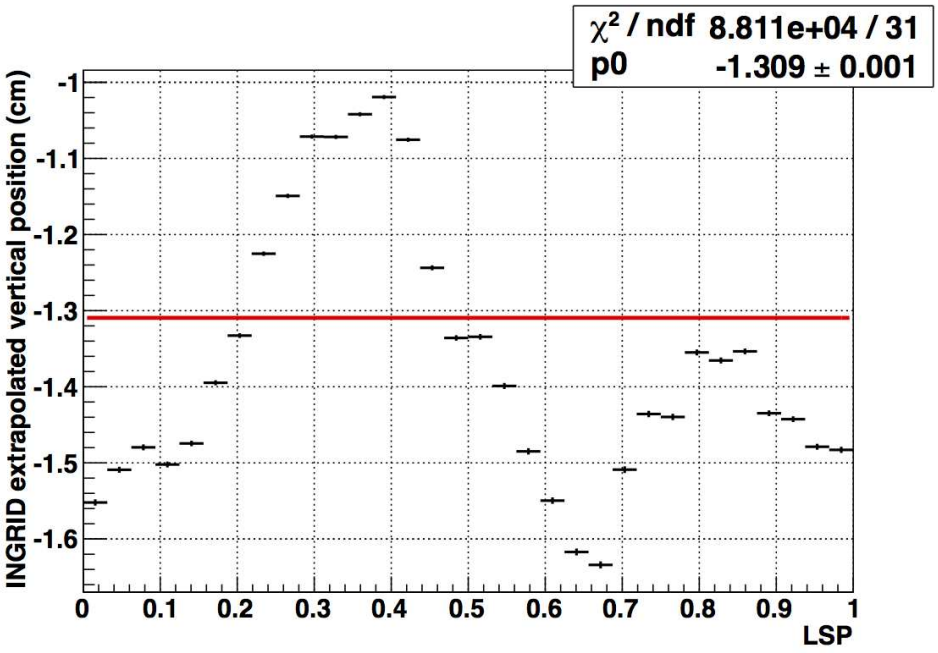

FIGURE 7.21. ν_μ beam vertical beam positions in the Silicon pixel part of the MuMon for T2K Run 2.

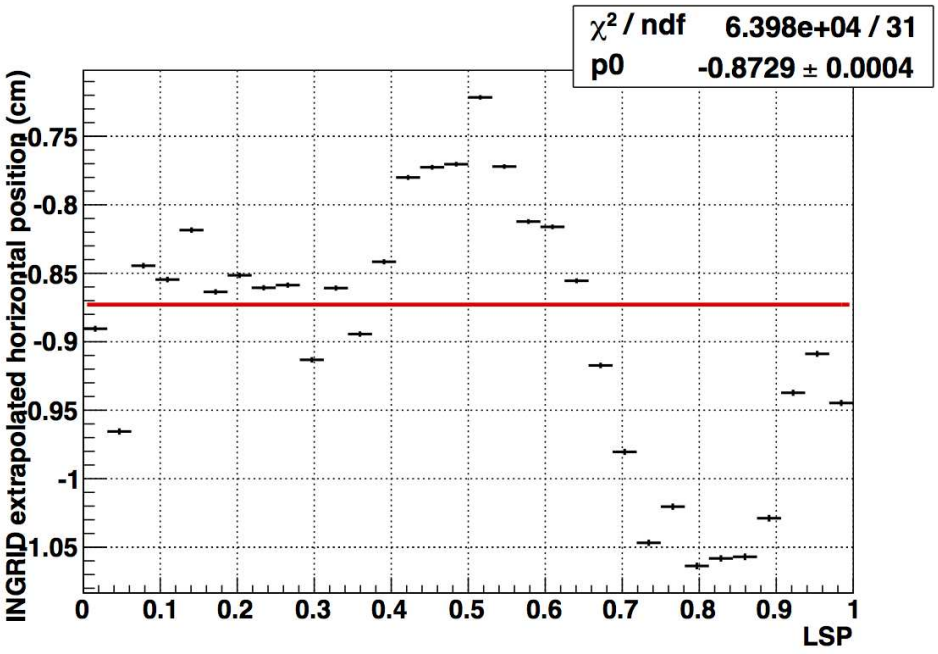

FIGURE 7.22. ν_μ beam horizontal beam positions in the Silicon pixel part of the MuMon for T2K Run 3.

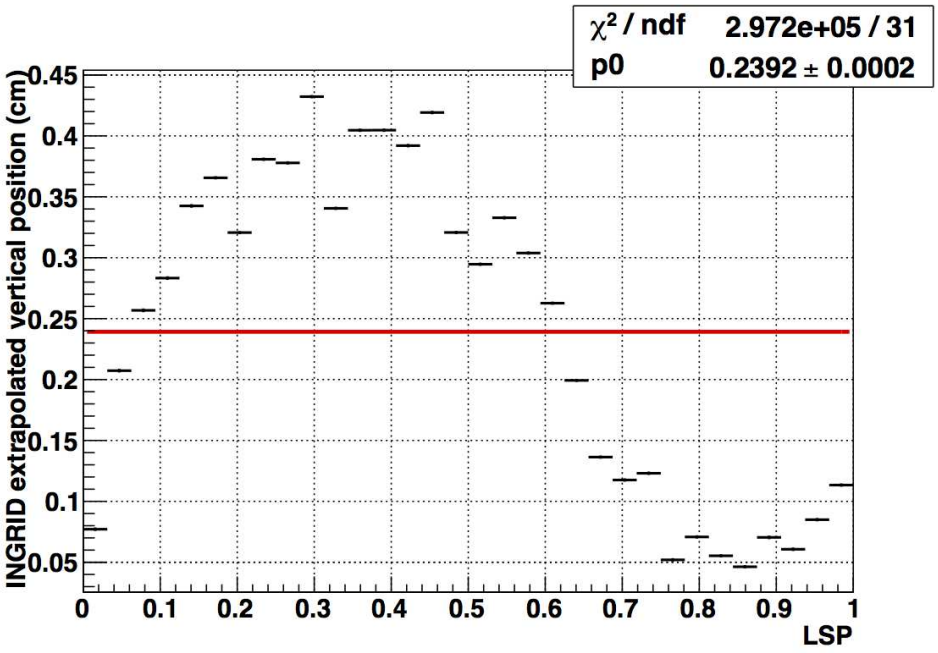

FIGURE 7.23. ν_μ beam vertical beam positions in the Silicon pixel part of the MuMon for T2K Run 3.

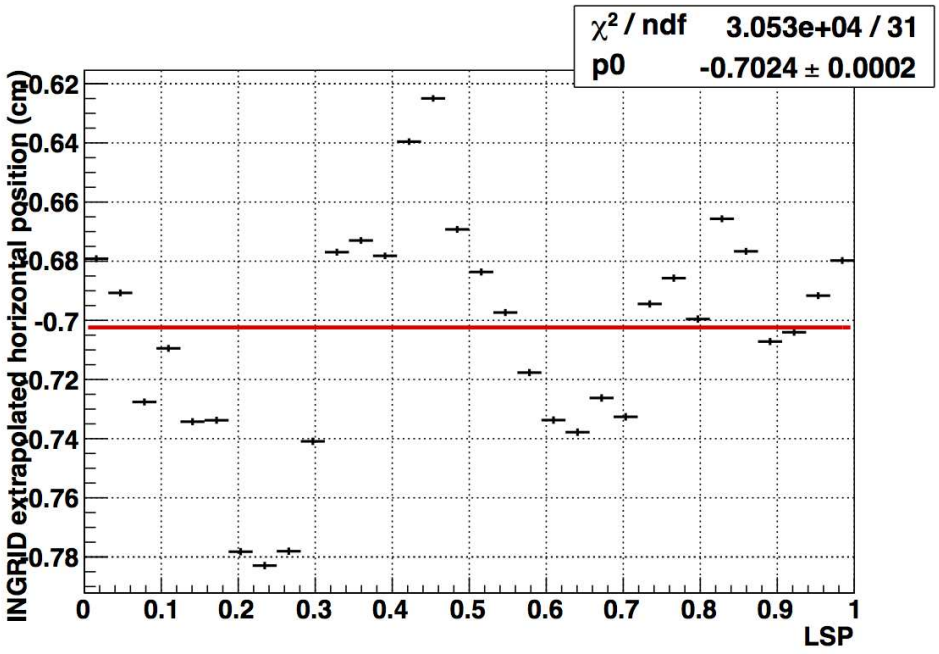

FIGURE 7.24. ν_μ beam horizontal beam positions in the Silicon pixel part of the MuMon for T2K Run 4.

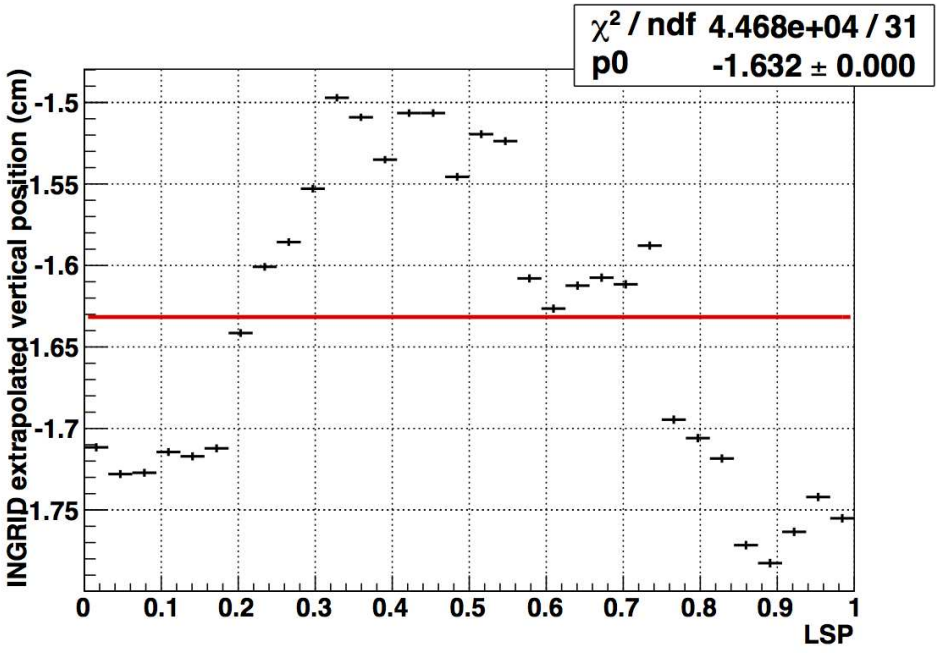

FIGURE 7.25. ν_μ beam vertical beam positions in the Silicon pixel part of the MuMon for T2K Run 4.

Different patterns can be observed from these figures. These patterns are namely due to tidal variations (Figure 7.26), changes in beam orbit after beam stops, and incomplete LSP coverage run by run.

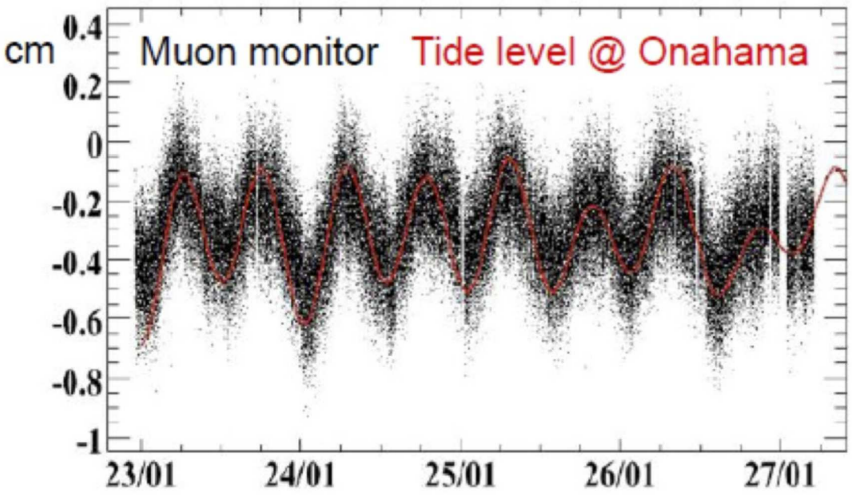

FIGURE 7.26. ν_μ beam horizontal beam position variation in the MuMon with time during a given time period of the T2K data taking. The tidal effect every ~ 6 hours can be seen.

A comparatively small variation (~ 0.2 cm) within Run 4 is observed. As Run 4 contributes to almost half of the entire statistical sample, variations in other low statistics runs will be washed out for all intents and purposes. The associated correction will take into account tidal effects that are known to distort the beam and vary its direction. Figure 7.26 shows, as a function of time, the beam position variation in the MuMon as a means to provide evidence that the MuMon is sensitive enough to observe, and therefore correct, tidal effects.

7.2.4. BEAM POSITION CORRECTION IN INGRID. MC simulation was used to study the beam center variations on the number of ν_μ candidates at INGRID. Many different

toy experiments were generated where the beam horizontal position was changed from its nominal value of 0cm to 0.2 cm, 0.8 cm, 1.5 cm, 1.9 cm, 3.0 cm, 6.0 cm, 6.4 cm, 9.0 cm. It is assumed here that:

- The event rate variation in the vertical modules is the same as in the horizontal modules only scaled by a factor of $S = \frac{\text{Horizontal beam width}}{\text{Vertical beam width}}$. The relative variations are expected to be higher in a narrower beam. Using Run 4 data, the scaling factor is taken as $S = \frac{452}{434}$.
- The event rate correction on the horizontal and vertical beam positions are independent and only affect the horizontal and vertical modules respectively. It is a reasonable assumption that the flux is almost constant in the central module as the beam width is larger than 4m.
- The beam has a left/right symmetry around its center, as well as a top/bottom one.

Figure 7.27 shows the variation of the number of events in the horizontal modules. A linear curve is used to represent the decrease in the number of events.

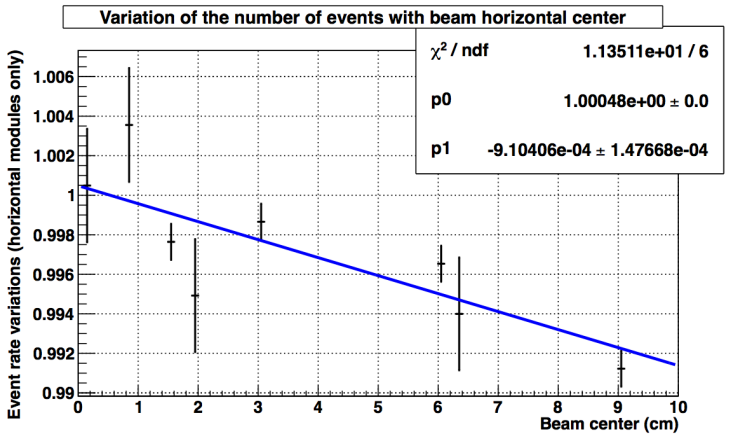

FIGURE 7.27. Number of ν_μ events with different beam horizontal center positions. A linear decrease with the beam center position difference with the INGRID center is assumed. The fitting result shows the relative variation on the number of events in the horizontal module to be $9.1 \times 10^{-4} \cdot \text{Beam center (cm)} + 1$.

On an event by event basis, the following correction is applied:

- The LSP, T2K run, and module type (horizontal or vertical) is determined
- The relative variation in event rate is extracted by reporting the beam center position shown in Figures 7.14-7.17 on Figure 7.27, and the event rate variations E_{Run} is calculated. If the event occurs within a vertical module, it is multiplied by S. The correction is the inverse of E_{Run}. Table 7.4 summarizes these corrections in the horizontal and vertical directions.
- In the same way as the above point, the correction within a single run is estimated. The LSP for a given event is calculated an the variation around the particular run position is extracted from Figure 7.18-7.24 (if the horizontal module is hit) or Figure 7.19-7.19 (vertical).

TABLE 7.4. Correction factor to apply to each event according to its run number and module (vertical or horizontal).

T2K run	Run 1	Run 2	Run 3	Run 4
Correction (horizontal)	1.006	1.000	1.008	1.002
Correction (vertical)	1.002	1.001	1.003	1.002

Figure 7.28 shows the systematic variation with the beam center. Figure 7.18-7.24 and 7.19-7.25 show a maximal variation of 1.5cm (extracted from Run 1). Figure 7.28 shows the systematic error associated with this correction and is taken to be $\sim 0.02\%$ for the horizontal modules. Summing in quadrature the systematic correction in the vertical modules ($\sim 0.6cm$ maximally), the resulting systematic uncertainty due to the beam position variation within one run is $\sim 0.03\%$ and is thus negligible.

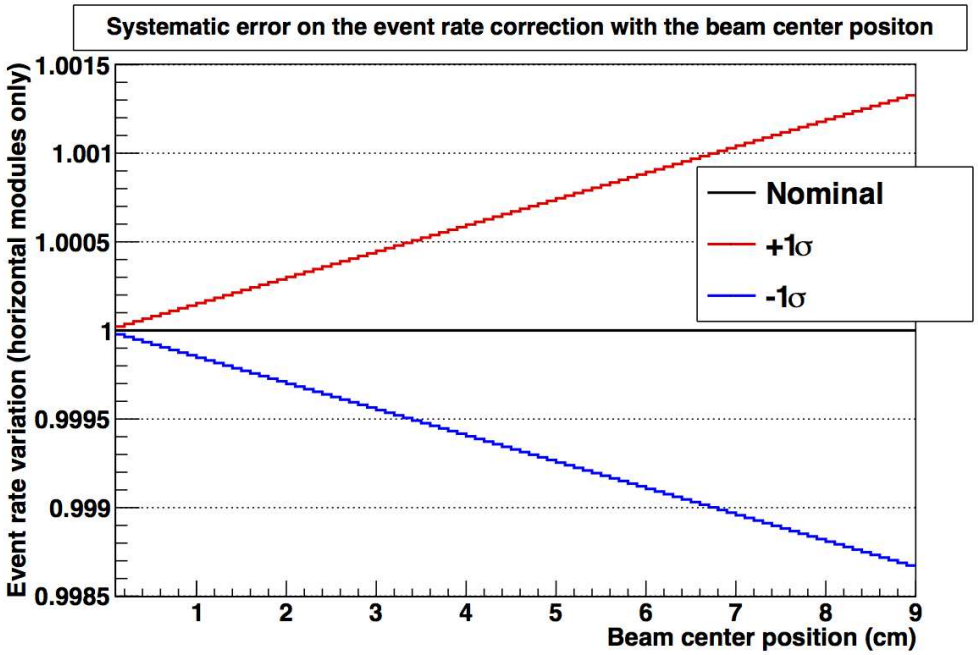

FIGURE 7.28. Systematic error associated to the correction of the number of ν_μ events with the center beam position (from the fitting error).

For the correction between different runs, the maximal difference for the correction applied comes for Run 2 and Run3. Their beam center is shown in Figure 7.14 to 7.17. Using the mean of the vertical and horizontal corrections, the total number of events in Run 3 is corrected. The total correction for Run 3 is then 1.0055 and 1.0005 for Run 2. The difference between these two total corrections is 0.005 which corresponds to a beam center variation of $\sim$ 5.5cm (using Figure 7.27). Figure 7.28 shows the systematic uncertainty and is equal to 0.08%. Considering the statistical uncertainty is $\sim$ 0.3%, this systematic error is neglected. Figure 7.29 shows the ν_μ rate versus LSP after all corrections described have been applied.

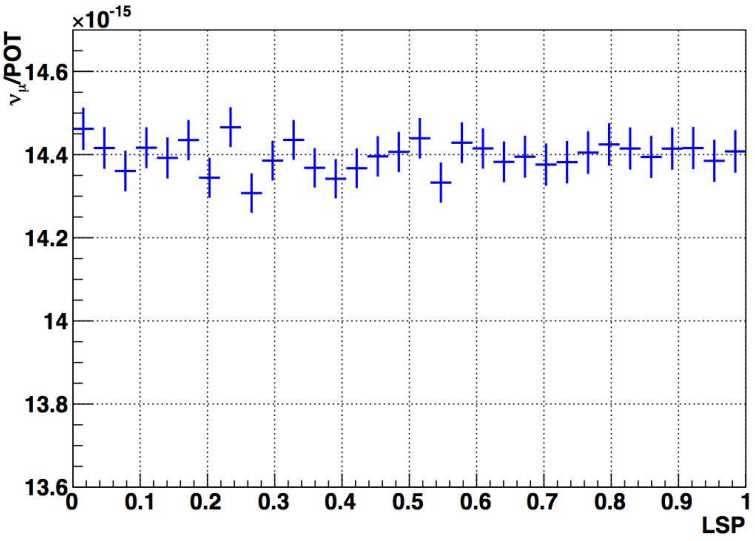

FIGURE 7.29. ν_μ rate versus LSP distribution in INGRID after pile-up, MPPC dark noise, MPPC gain, and beam position corrections have been taken into account.

7.2.5. BEAM POSITION VARIATION WITHIN ONE RUN AT ND280. The beam variation within a run in ND280 was evaluated using True Monte Carlo studies only. Figure 7.30 provides a schematic to illustrate the evaluation procedure. The evaluation procedure is as follows:

(1) For a given run, the X and Y positions of the True neutrino events are plotted in a histogram over the entire face of the P0D (green box).

(2) The fiducial volume (FV) used in the ND280 selection is known and the number of true MC events in the FV and the number of true selected MC events in the FV can be calculated (blue and purple boxes).

(3) Run 2 water shows the largest variation of ± 6mm. The FV is shifted by 6mm in a random direction.

(4) The number of true events in the shifted FV (orange box) is then calculated.

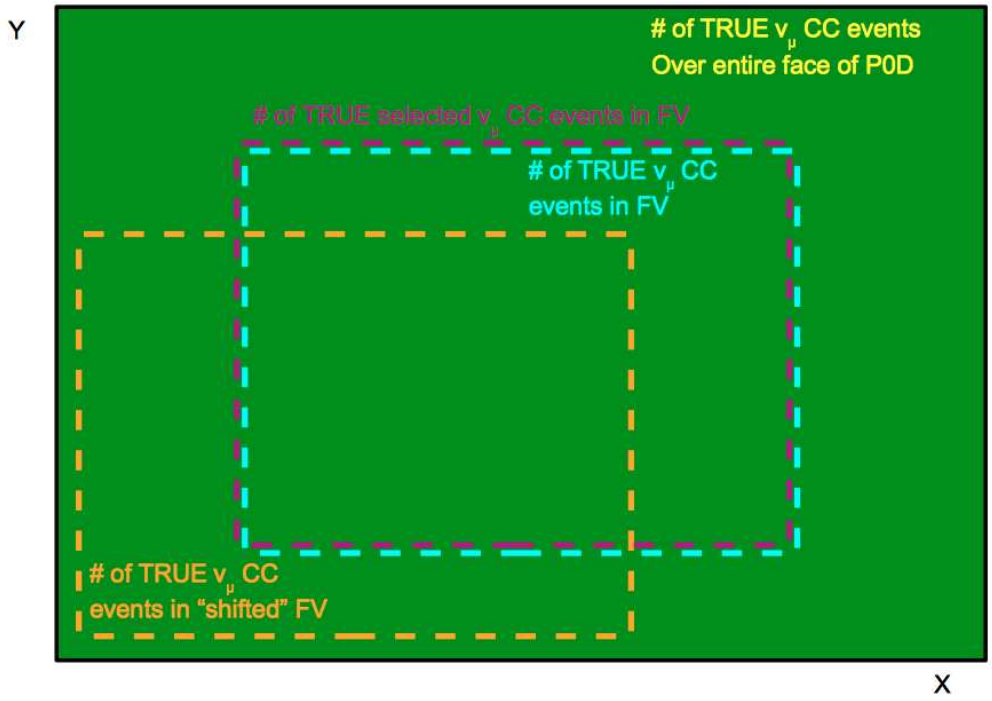

FIGURE 7.30. Schematic of method that was used to evaluate the effect of beam position variation in the P0D. The green box represents the X, Y projection of the number of true MC ν_μ CC inclusive events. The purple box represents the number of true MC selected in the Fiducial Volume while the blue box represents the number of true MC events in the Fiducial Volume. Note, the offset is only for visual purposes and in reality they are on top of each other. The orange box represents the number of True MC events for a given random shift of the Fiducial Volume.

The dimensions for the active region and the FV of the P0D are given in Table 7.5.

TABLE 7.5. The dimensions of the active region and FV of the P0D. All values are quoted in mm.

	X	Y	Z
Active Region	2103	2239	2400
FV	1600	1740	1705

From the table, a shift of 6mm in a random direction will not cause the procedure to be evaluated at the edges of the P0D. For each (i, j) bin in FV, a re-weighting factor is applied in order to calculated a re-weighted total number of events for a given shift:

(7.7)
$$R_{ij} = \frac{N_{ij}^{True,ShiftedFV}}{N_{ij}^{True,FV}}$$

where, $N_{ij}^{True,ShiftedFV}$ is the total number of true neutrino events in the i, j bin of the shifted FV (orange box) and $N_{ij}^{True,FV}$ is the total number of true neutrino events in the nominal FV (blue box). This re-weighting factor is applied to the total number of true selected neutrino events in the FV (purple box) and the summation over each i, j bin is calculated to provide a new total:

(7.8)
$$N_{Total} = \sum_{ij} R_{ij} N_{ij}^{SelectedTrue,FV}$$

A distribution of N_{Total} is created by applying 100 shifts and recalculating N_{Total}. As mentioned before, since Run 2 shows the largest variation, only Run2 water MC is analyzed.

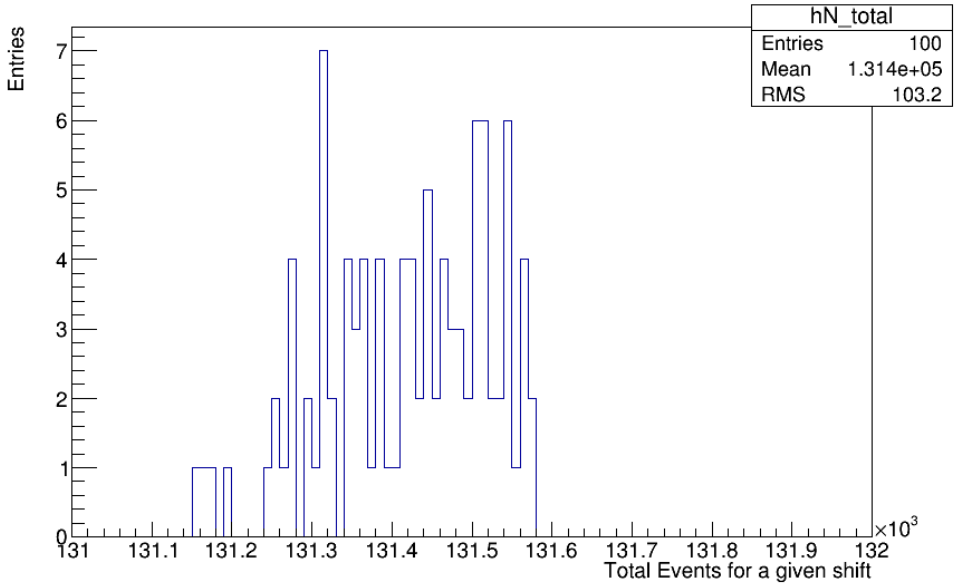

FIGURE 7.31. A histogram of N_{Total} for 100 random shifts.

A variation of 0.07% on N_{Total} is found for 100 random shifts using this procedure. Considering the statistical error for a given run is $\approx 4\%$, the beam variation effects within a given run is negligible for the ND280 LV analysis and no correction is evaluated.

7.2.6. Residual Rate Correction in INGRID. The remaining variations of the event rate where the detector and beam sources are no longer separated were studied. The Run 4 data taking period is divided up into two periods: end of 2012 (October 2012 - 31 December 2012) and the beginning of 2014 (January 2014 - May 2013). This was done because Run 4 lasted long and was stopped for the new year. Thus, possible variations in the event rate due to, among other things, different beam tuning is expected during this run.

For each of the five periods, a correction was calculated from the average event rate as changes in the beam position between runs could be a possible source of event rate variation. However, it is important not to correct differences due to LV effects. The following method is used to remove any correction with a potential LV effect from each of the five periods (which will be called runs for simplicity):

(1) The POT is plotted as a function of LSP and shown in Figure 7.32 to 7.36.

(2) The POT distributions are fitted with a constant $\langle \mathrm{POT} \rangle_{\mathrm{Run}}$. For each LSP bin i and run r the ratio with the average run POT is calculated as $d_r^i = \mathrm{POT}_r^i / \langle \mathrm{POT} \rangle_r$.

(3) The ν_μ/POT are reweighted event by event by the factor $w_r^i = 1/d_r^i$ to simulate a flat POT coverage in LSP.

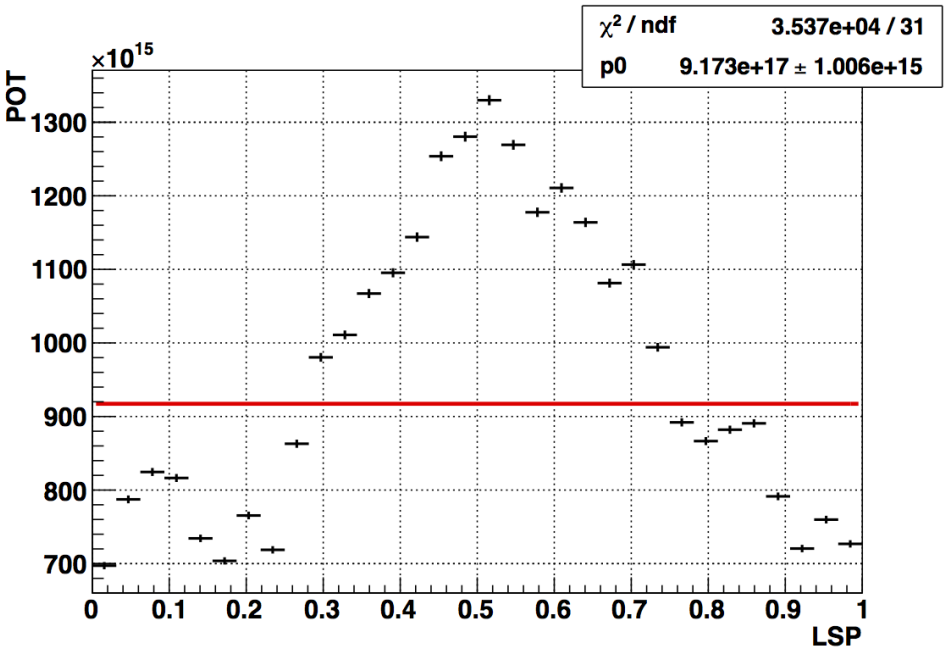

FIGURE 7.32. POT distributions versus LSP for T2K Run 1.

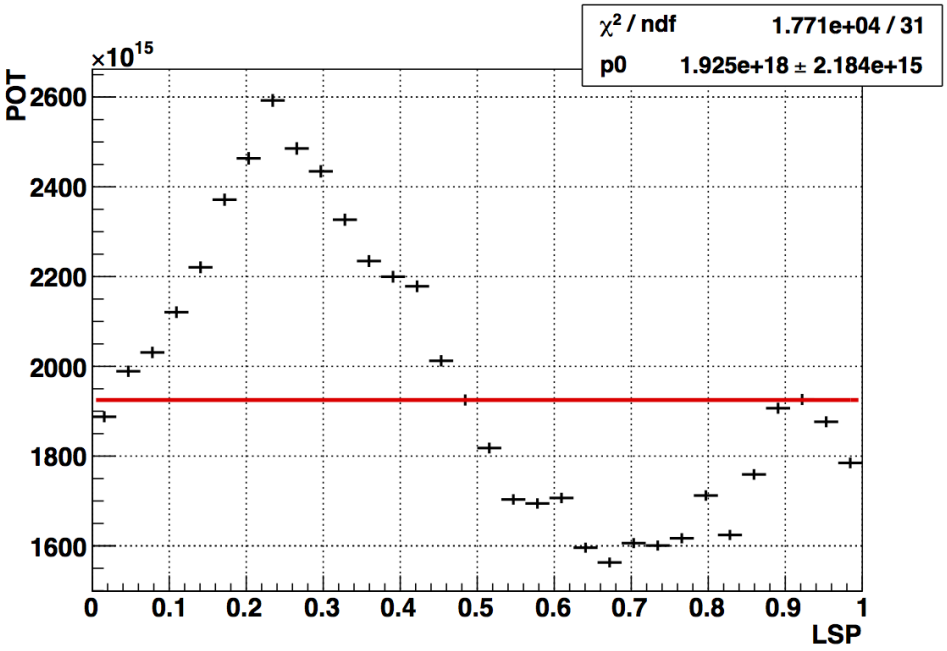

FIGURE 7.33. POT distributions versus LSP for T2K Run 2.

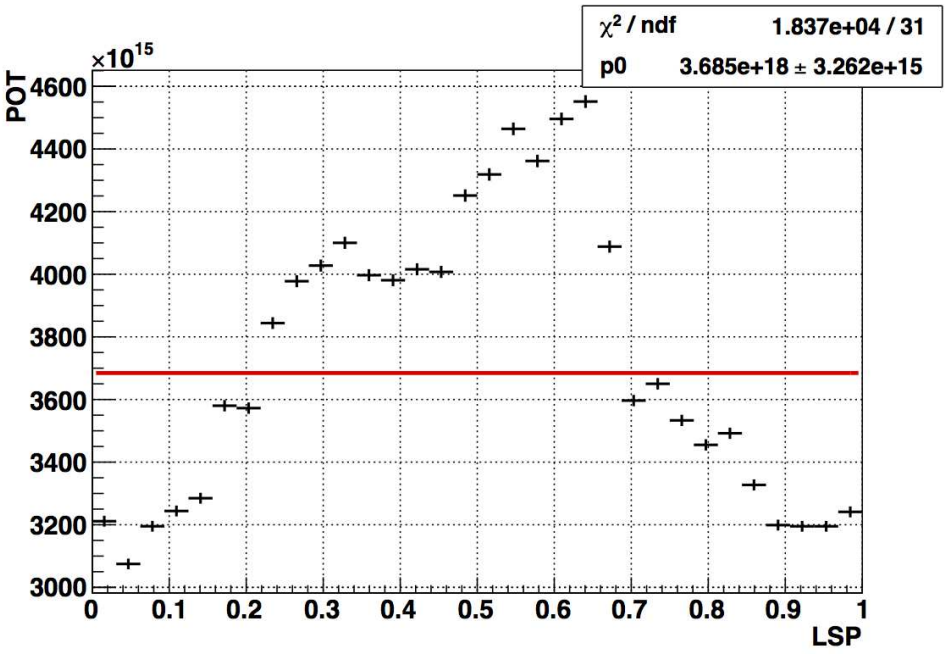

FIGURE 7.34. POT distributions versus LSP for T2K Run 3.

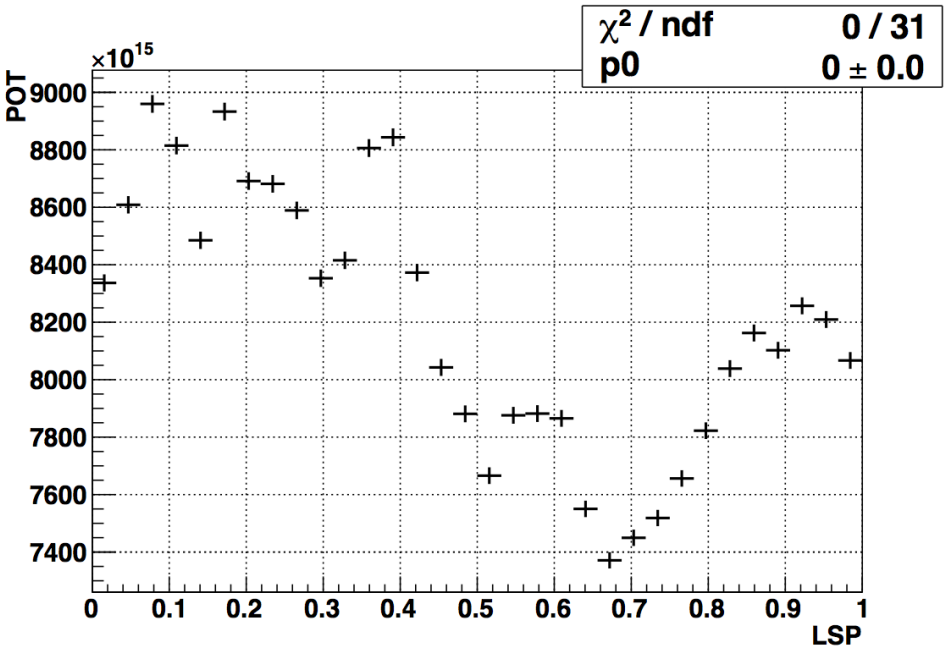

FIGURE 7.35. POT distributions versus LSP for T2K Run 4 2012.

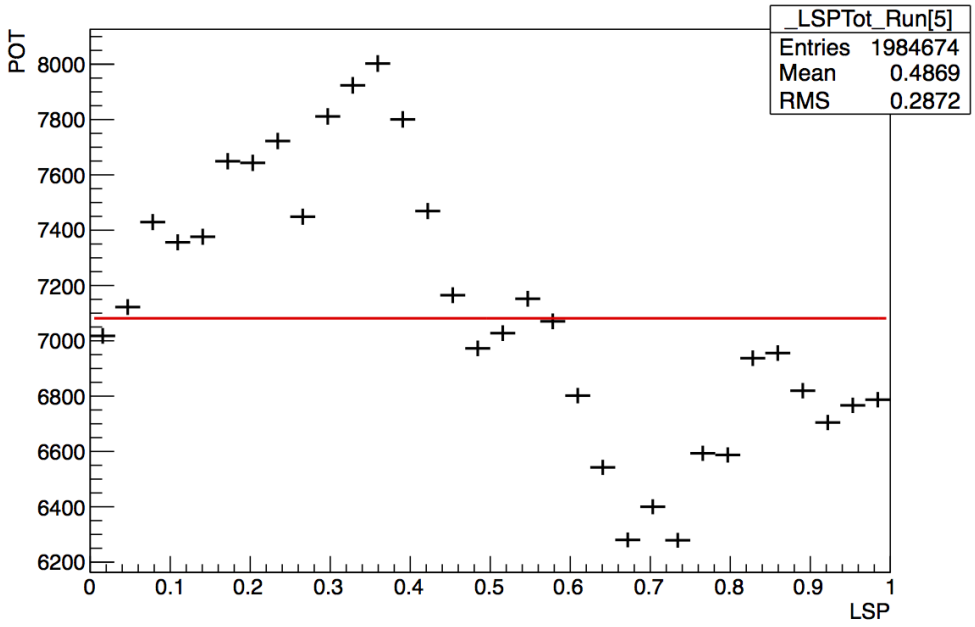

FIGURE 7.36. POT distributions versus LSP for T2K Run 4 2013.

This method produces a flat POT coverage and new event rate distributions for each run. Doing this washes out any event rate variations between runs due to different LSP coverage of the data. Figure 7.37 to Figure 7.41 show the five event rate distributions:

The correction is evaluated run by run in the following way:

(1) The event rate distribution versus LSP is fitted by a constant. This constant represents the average event rate for a given run: $\langle \frac{\nu_\mu}{POT} \rangle_{\text{Run}}$.

(2) The correction factor is taken as the ratio between a reference event rate (second part of Run 4) and the run average event rate:

$$c_{\text{Run}} = \frac{\langle \frac{\nu_\mu}{POT} \rangle_{Run42013}}{\langle \frac{\nu_\mu}{POT} \rangle_{\text{Run}}}. \tag{7.9}$$

(3) Data are reprocessed and the correction factor c_{Run} is applied event by event on the number of ν_μ.

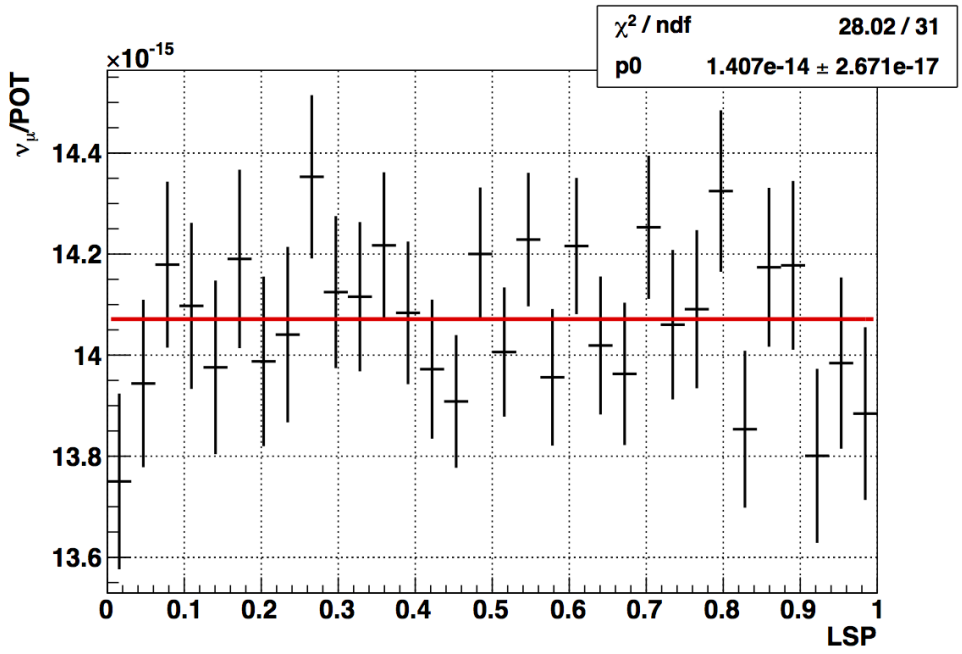

FIGURE 7.37. Number of ν_μ per POT distributions versus LSP in INGRID for T2K Run 1.

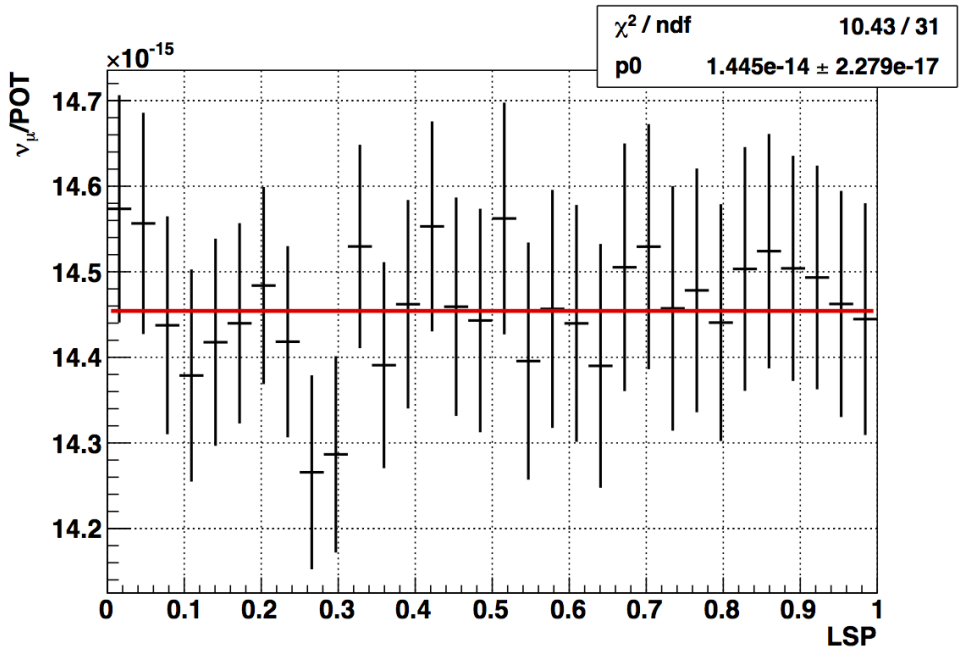

FIGURE 7.38. Number of ν_μ per POT distributions versus LSP in INGRID for T2K Run 2.

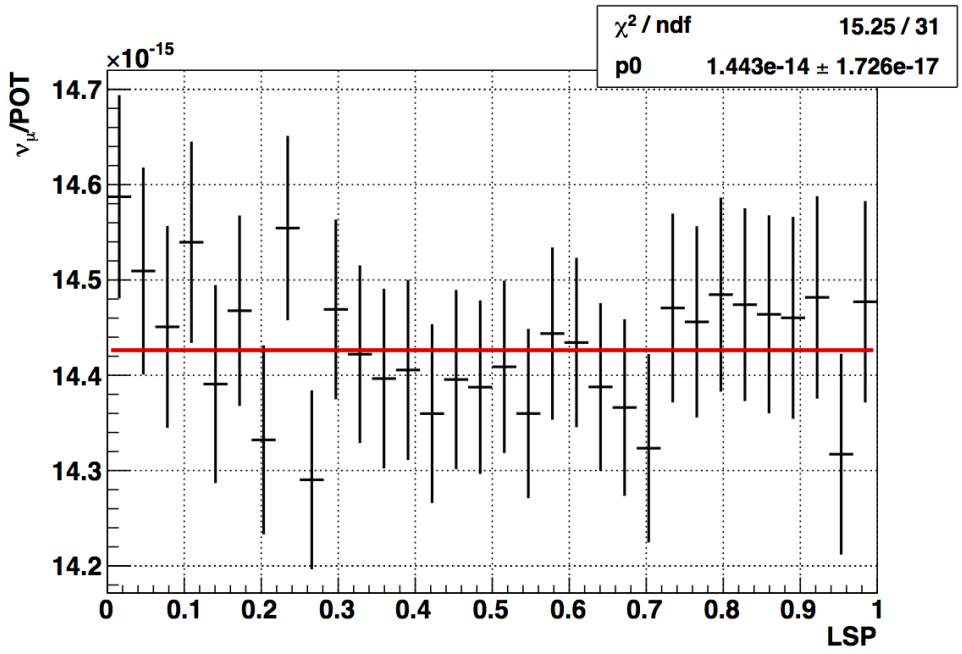

FIGURE 7.39. Number of ν_μ per POT distributions versus LSP in INGRID for T2K Run 3.

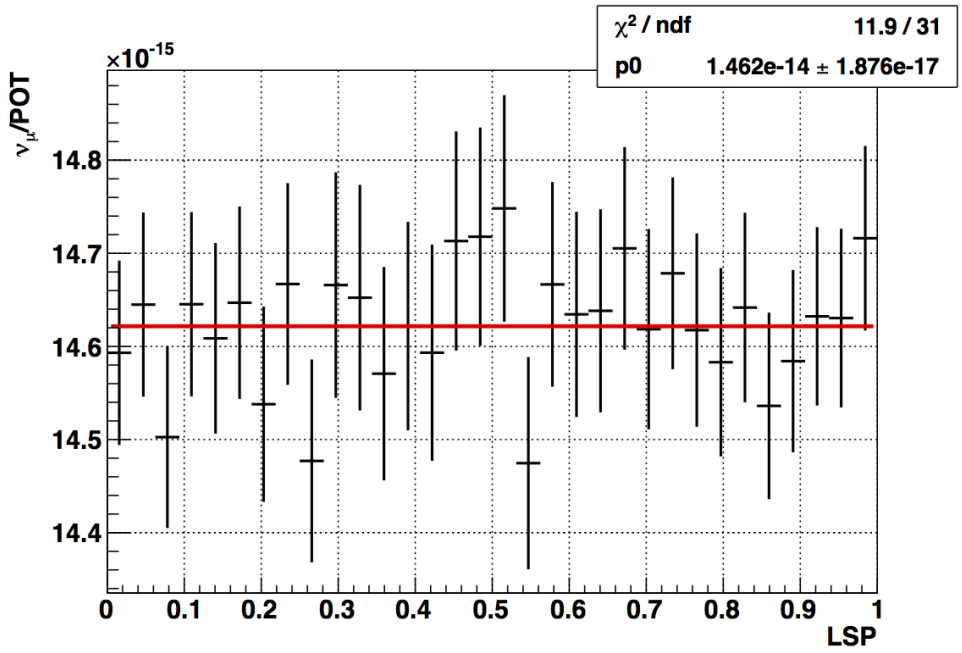

FIGURE 7.40. Number of ν_μ per POT distributions versus LSP in INGRID for T2K Run 4 2012.

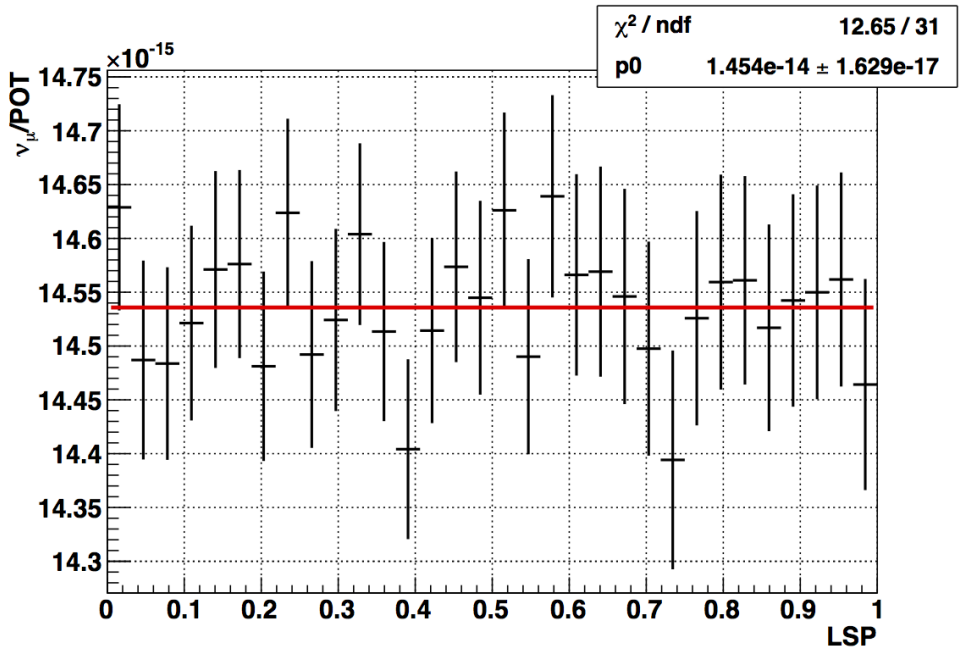

FIGURE 7.41. Number of ν_μ per POT distributions versus LSP in INGRID for T2K Run 4 2013.

Each run correction is shown in Table 7.6. A difference between Run 4 2012 and Run 4 2013 is observed due to changes in running conditions after the end of the year shutdown.

TABLE 7.6. Correction factor to apply to each event according to its run number, due to event rate variations between runs. The $\pm 1\sigma$ error is shown, taking into account error on Run 4 2013 event rate.

T2K run	Run 1	Run 2	Run 3	Run 4 2012	Run 4 2013
Correction	1.033 ± 0.003	1.006 ± 0.003	1.007 ± 0.003	0.995 ± 0.004	1.

Figure 7.42 shows the relative correction. A 0.3% increase in the event rate can be observed as Run 4 2013 has a higher event rate compared to most of the other runs (except for Run 4 2012). This correction does not impact the shape study of this analysis. Additionally, a 0.2% correction that does affect the shape is observed. This is due to the fact that most of the spills populating the LSP distribution between 0.2 and 0.8 come from Run 4 2013 whereas the remaining LSP bins are populated by other runs containing a lower event rate.

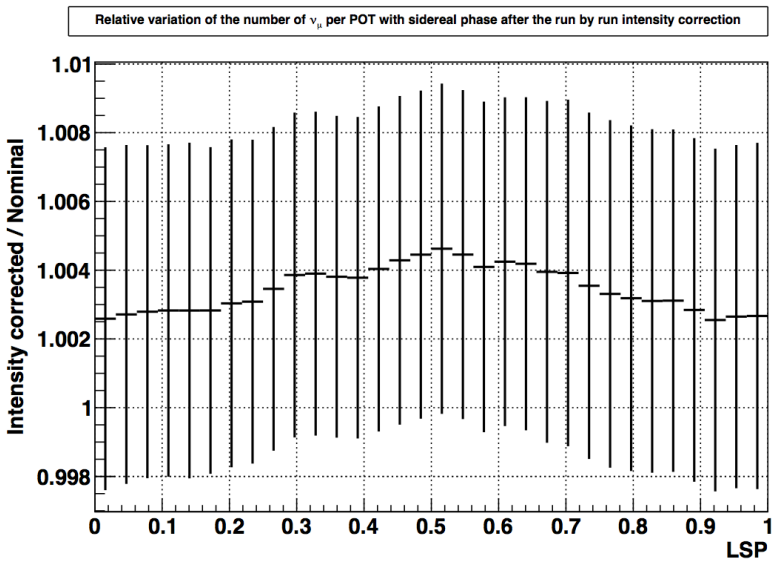

FIGURE 7.42. Relative correction coming from run per run event rate correction in INGRID.

The systematic error associated with this correction is taken as the statistical uncertainty coming from the correction c_{Run}. The $+1\sigma$ error estimation is defined as the highest possible correction. This is obtained by maximizing each correction shown in Table 7.6 except for Run 4 2012. Run 4 2012 should be minimized to increase the difference between it and Run 4 2013. Figure 7.43 shows the $\pm 1\sigma$ corrections.

The relative error on the shape correction varies from 1.0002 to 1.0007 for the $+1\sigma$. A 0.05% systematic error is found and, thus, is neglected.

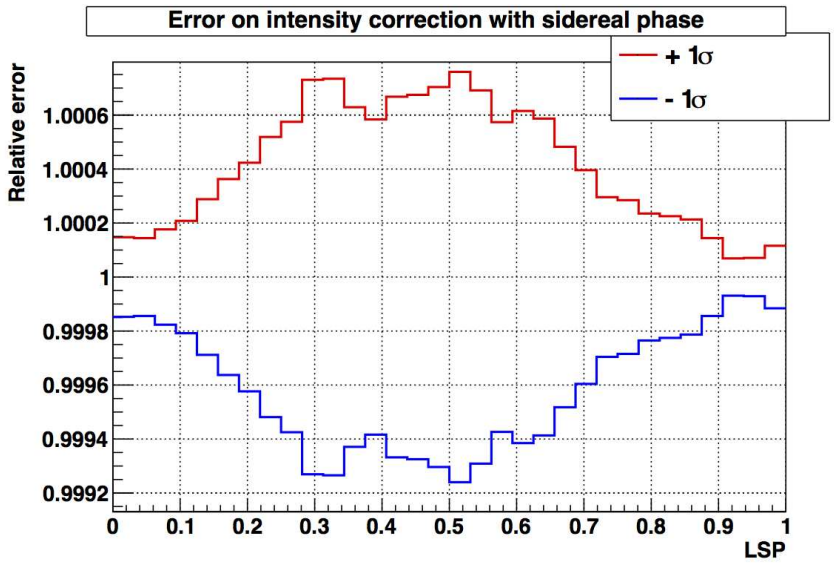

FIGURE 7.43. Relative variation of the run per run event rate correction in INGRID due to $\pm 1\sigma$ systematic error.

7.2.7. RESIDUAL RATE CORRECTION IN ND280. The residual rate correction in ND280 was calculated almost exactly the same as in INGRID. The procedure is outlined below:

(1) The POT is plotted as a function of LSP.

(2) The POT distributions are fitted with a constant $\langle \mathrm{POT} \rangle_{\mathrm{Run}}$. For each LSP bin i and run r the ratio with the average run POT is calculated as $d_r^i = \mathrm{POT}_r^i / \langle \mathrm{POT} \rangle_r$.

(3) The ν_μ/POT are reweighted event by event by the factor $w_r^i = 1/d_r^i$ to simulate a flat POT coverage in LSP.

The correction is evaluated run by run in the following way:

(1) The event rate distribution versus LSP is fitted by a constant. This constant represents the average event rate for a given run: $\langle \frac{\nu_\mu}{POT} \rangle_{\mathrm{Run}}$.

(2) The correction factor is taken as the ratio between a reference event rate and the run average event rate depending on the configuration of the P0D:

$$c_{\mathrm{Run}} = \frac{\langle \frac{\nu_\mu}{POT} \rangle_{Run42013water,air}}{\langle \frac{\nu_\mu}{POT} \rangle_{\mathrm{Run}}}. \tag{7.10}$$

(3) Data are reprocessed and the correction factor c_{Run} is applied event by event on the number of ν_μ.

The residual rate corrections for ND280 samples are provided below:

TABLE 7.7. Correction factor to apply to each event according to its run number, due to event rate variations between runs for water-in.

T2K run	Run1 Water	Run2 Water	Run4 2012 Water	Run4 2013 Water
Correction	1.08229 ± 0.022	1.006 ± 0.017	1.011 ± 0.014	1

TABLE 7.8. Correction factor to apply to each event according to its run number, due to event rate variations between runs for water-out.

T2K run	Run2 Air	Run3 Air	Run4 2013 Air
Correction	1.096 ± 0.022	1.012 ± 0.013	1

7.3. SUMMARY OF SYSTEMATIC ERRORS

The ν_μ event rate versus LSP for INGRID after having applied all corrections is shown in Figure 7.44. As the systematic error coming from each correction is negligible, only the statistical error is relevant. The evaluations on the systematic error sources are shown in Table 7.9.

TABLE 7.9. Summary of systematic uncertainties coming from time-dependent effects, to be compared with a statistical uncertainty of 0.3%.

Source	Systematic uncertainty (%)
Pile-up	0.01
MPPC dark noise	0.01
MPPC gain variation	0.06
Beam position	0.03
Rate correction	0.05
Total systematic	0.08

The ν_μ event rate versus LSP for ND280 water-in and water-out after having applied the residual rate correction is shown in Figures 7.45 and 7.46. As the systematic error coming

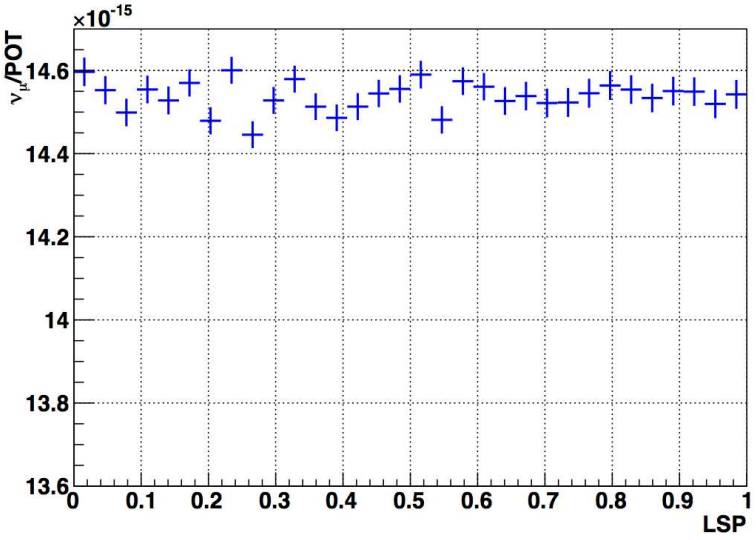

FIGURE 7.44. Corrected ν_μ event rate versus LSP in INGRID.

from each source is negligible, only the statistical error is relevant. The evaluations on the systematic error sources are shown in Table 7.10.

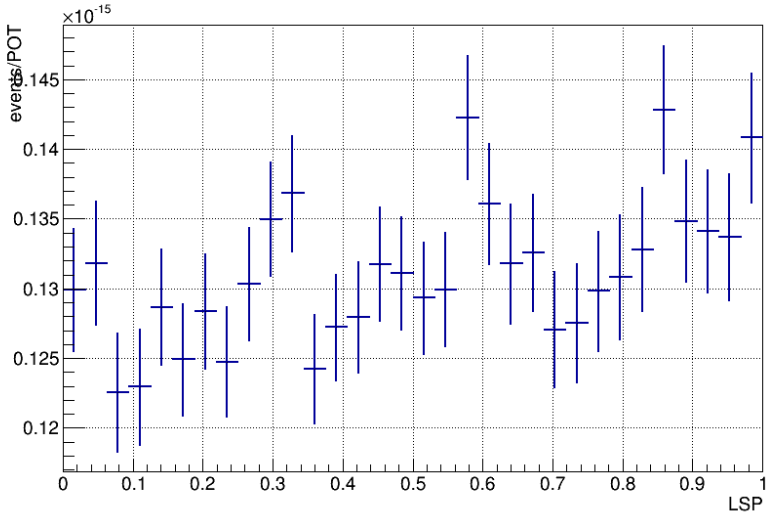

FIGURE 7.45. Corrected ν_μ event rate versus LSP for ND280 water-in.

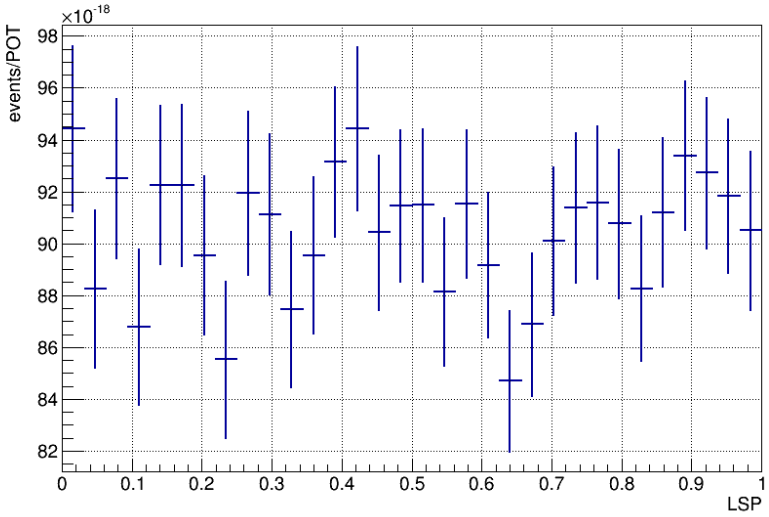

FIGURE 7.46. Corrected ν_μ event rate versus LSP for ND280 water-out.

TABLE 7.10. Summary of systematic uncertainties coming from time-dependent effects, to be compared with a statistical uncertainty of 4% for both ND280 samples.

Source	Systematic uncertainty (%)
Pile-up	0.005
MPPC dark noise	-
MPPC gain variation	-
Beam position	0.07
Rate correction	-
Total systematic	0.07

CHAPTER 8

T2K LV Analysis

This chapter describes the following:

(1) The data samples

(2) The POT normailzed neutrino event LSP distributions

(3) How a set of 10,000 toy MC with no LV signal are generated

(4) A Fast Fourier Transform method that is used for each data set to search for sidereal variations

(5) The importance of correlations between different SME coefficients and how these correlations affect T2K's sensitivity to LV

(6) A Binned Likelihood fit method that is only used on the INGRID sample

The FFT method is performed on the ND280 and INGRID data samples. Note, because of the high degree of correlation between SME coefficients a binned likelihood fit method is developed to extract information about the $(\mathcal{C})_{ab}$, $(\mathcal{A}_s)_{ab}$, $(\mathcal{A}_c)_{ab}$, $(\mathcal{B}_s)_{ab}$, and $(\mathcal{B}_c)_{ab}$ combinations. This fit is only performed on the INGRID data set as INGRID provides the largest statistical sample.

8.1. Data Samples

The INGRID data sample consists of T2K runs 1 - 4, while the ND280 data samples are broken up into water-in and water-out samples. The INGRID data samples are shown in Table 8.1:

TABLE 8.1. INGRID data samples

Data Set	Run Period	POT	Events
Run 1	Jan. 2010 - June 2010	3.26×10^{19}	430768
Run 2	Nov. 2010 - March 2011	1.12×10^{20}	910296
Run 3	April 2012 - June 2012	1.59×10^{20}	1724430
Run 4	Jan. 2010 - June 2010	3.55×10^{20}	3822209

and the ND280 data samples are shown in Table 8.2

TABLE 8.2. ND280 data samples

Data Set	Run Period	POT	Events
Run 1 water-in	Jan. 2010 - June 2010	2.94×10^{19}	3733
Run 2 water-in	Nov. 2010 - Feb. 2011	4.29×10^{19}	3024
Run 2 water-out	Feb. 2011 - March 2012	3.55×10^{19}	5583
Run 3 water-out	April 2012 - June 2012	13.48×10^{19}	12162
Run 4 water-in	Oct. 2012 - Feb. 2013	16.24×10^{19}	20934
Run 4 water-out	Feb. 2013 - Aug. 2013	15.86×10^{19}	14127

8.2. LOCAL SIDERAL TIME DISTRIBUTIONS

The Local Sidereal Time (LST) distributions are created from data for each T2K near detector - see [20] for the definition. The LST distributions are then converted to Local Sidereal Phase (LSP) distributions. LSP is given by:

$$LSP = \mathrm{mod}\Big(\frac{T_{\oplus}\omega_{\oplus}}{2\pi}\Big) = \mathrm{mod}\Big(\frac{T_{\oplus}}{23^h56^m4.0916^s}\Big) \tag{8.1}$$

Thus, LSP is the modulus of the fraction of a mean sidereal day for the time of a neutrino event or integrated POT when converted to LST. The LSP histograms are used to perform the LV search and to create a set of 10,000 Toy MC for each T2K near detector in order to study the sensitivity to a sidereal variation. The T2K LV LSP distributions use official CC-inclusive selection methods for T2K Runs 1 - 4. The details of how the necessary information

is obtained is different for each near detector and is outlined in the following subsections. Here, a brief overview is given:

(1) Obtain a list of ν_μ candidate events for Runs 1 - 4 from detector ntuples.

(2) Obtain a list of corresponding spill POT for Runs 1 - 4 from detector ntuples.

(3) Obtain the timestamps for each quantity and convert to LST [20], then to LSP distributions.

(4) On a bin by bin basis, apply a solar time correction to the LSP distributions.

(5) On a bin by bin basis, divide the two histograms to obtain the POT normalized ν_μ candidate event rates as a function of LSP with 32 bins.

This calculation is performed for every event and associated POT in a given spill for all spills in Runs 1 - 4. The POT information comes from beam counters, and is provided by the T2K beam group in the Beam Summary Data (BSD). For each spill, the beam group provides the number of protons impinging on the T2K graphite target. The BSD relative to a given spill are added to the INGRID and ND280 data streams during data processing. When analyzing T2K data, for each spill during which the near detectors were active, the number of POT hitting the target is retrieved. It is therefore possible to know exactly the number of POT delivered at any given time, and produce the above mentioned LSP distributions.

8.3. Toy MC Experiments

Using the corresponding 63,397,992 beam spills from T2K runs 1- 4, a total of 10,000 Toy MC experiments are created from the data LST distributions for each detector by shuffling the LSP bins of all spills using the Durstenfed version of the Fisher-Yates shuffle method described below:

(1) Generate a random sequence of integers from 0 to the total number of spills with no repetition using the Fisher-Yates Durstenfeld method [21].

(2) For each spill, reassign the spill POT and number of candidate events from the corresponding randomly generated spill number.

(3) Convert the times associated with the two quantities to LST, then to LSP.

(4) Histogram the shuffled results with 32 bins in LSP.

(5) Divide the two histograms $\left(\frac{\nu_\mu(LSP)}{POT(LSP)}\right)$.

(6) Repeat 10,000 times.

A binning of 32 bins is chosen for the Toy MC since the FFT is optimized to transform data sets of length 2^l where $l \in \mathbb{N}$. The binning was also chosen to be comparable to previous results from different experiments. This binning corresponds to 44.877 minutes in local sidereal time. Any coarser binning can result in aliasing effects in the LSP distributions which will greatly affect T2Ks sensitivity to LV. For each near detector, the Toy MC are rescaled by the inverse of their individual average event rates to avoid any computational roundoff errors that might arise when handling such naturally small numbers.

8.4. ND280 Toy MC

Beam Summary Data for T2K runs 1-4 are used. In this range of run periods there are 63,397,992 beam spills with timestamps and corresponding POT. From ND280 ntuples containing CC-inclusive events according to the tracker ν_μ selection [22], a list of good ND280 ν_μ events is produced with their timestamps. This list is compared with the Beam Summary Data and a list of T2K spills is created containing the timestamp, LSP, POT, and ND280 ν_μ event candidates. Dividing candidate events vs LSP histogram by the POT vs LSP histogram and shuffling the LSP bins using the procedure above, 10,000 Toy MC histograms are created

for ND280 with any potential LV signal removed. Figures 8.1 - 8.2 show examples of the unscaled and scaled Toy MC:

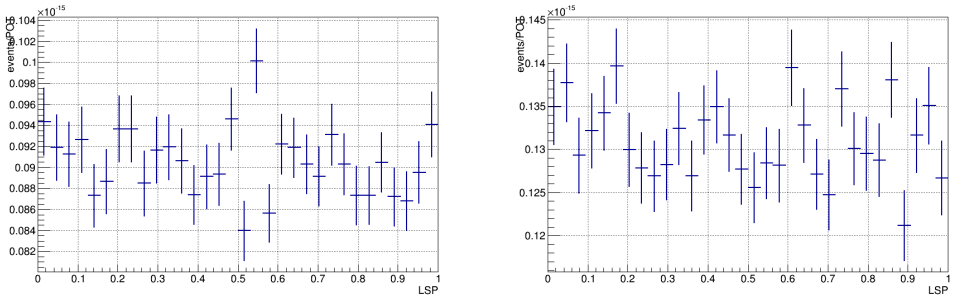

FIGURE 8.1. Examples of two unscaled ND280 flat toy MC

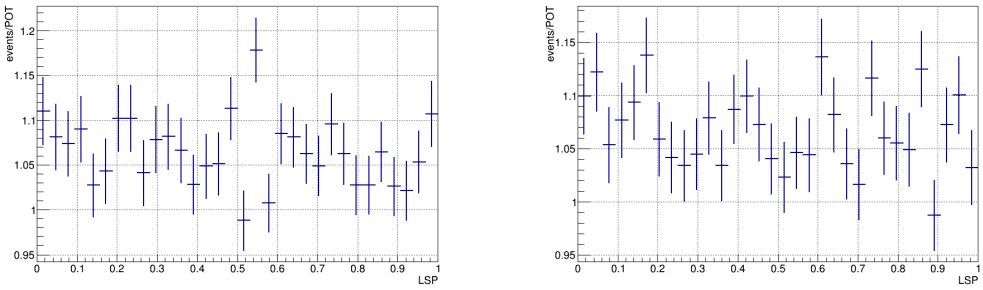

FIGURE 8.2. Examples of two ND280 flat toy MC rescaled by the inverse of the average.

For illustration purposes, random signal toys for ND280 are shown in Figure 8.3:

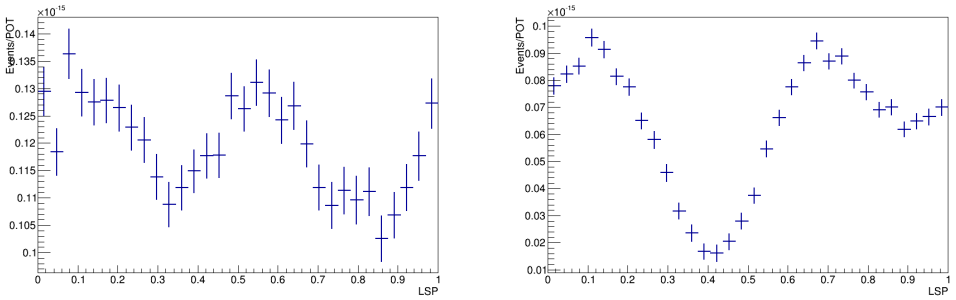

FIGURE 8.3. Examples of two ND280 signal toy MC. Random values of the SME coefficients were chosen from an appropriate Gaussian distribution.

The random values which were used to create the signal toy MC are given in Table 8.3:

TABLE 8.3. Random SME coefficients used to create ND280 signal toy MC(all values given in $\times 10^{-20}$).

Coefficient	Left Plot	Right Plot
a_L^T	7.1 GeV	-5.3 GeV
a_L^X	-5.3 GeV	10.2 GeV
a_L^Y	-8.8 GeV	5.1 GeV
a_L^Z	7.8 GeV	1.1 GeV
c_L^{TT}	16.0	6.5
c_L^{TX}	16.8	-18.3
c_L^{TY}	2.2	-28.9
c_L^{TZ}	-14.1	-7.7
c_L^{XX}	14.0	-0.45
c_L^{XY}	-5.5	0.63
c_L^{XZ}	-10.3	-7.7
c_L^{YY}	15.7	1.0
c_L^{YZ}	9.5	17.7
c_L^{ZZ}	3.1	-4.2

8.5. INGRID TOY MC

The INGRID Toy MC are created from information found in the INGRID ntuples. Using the same procedure in Section 8.3, 10,000 Toy MC histograms are created for INGRID with any potential LV signal removed. Examples and the scaled and unscaled Toy MC are shown in Figures 8.4 - 8.5:

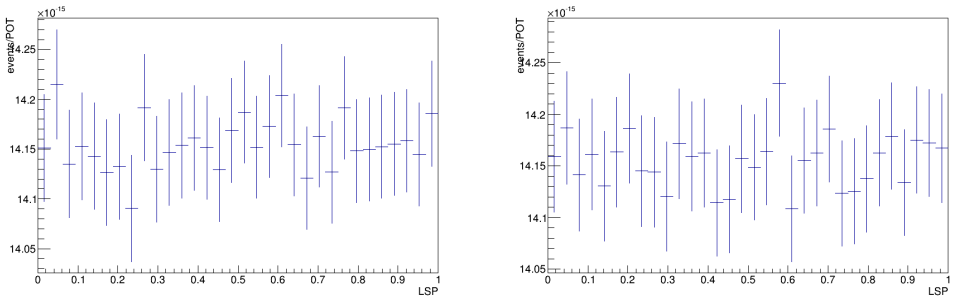

FIGURE 8.4. Examples of two unscaled INGRID flat toy MC

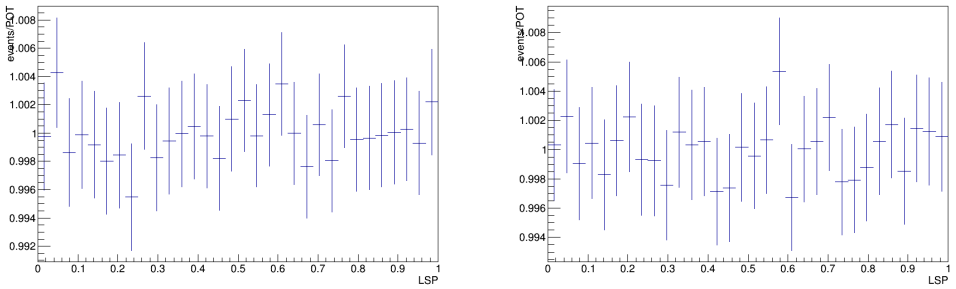

FIGURE 8.5. Examples of two INGRID flat toy MC rescaled by the inverse of the average.

For illustration purposes, two examples of random signal toys for INGRID are shown in Figure 8.6:

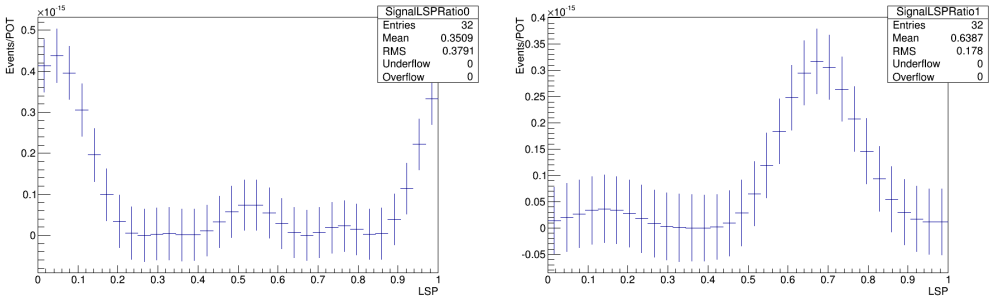

FIGURE 8.6. Examples of two INGRID signal toy MC. Random values of the SME coefficients were chosen from an appropriate Gaussian distribution.

The random values which were used to create the signal toy MC are given in Table 8.4:

TABLE 8.4. Random SME coefficients used to create INGRID signal toy MC(all values given in $\times 10^{-20}$).

Coefficient	Left Plot	Right Plot
a_L^T	7.1 GeV	-5.3 GeV
a_L^X	-5.3 GeV	10.2 GeV
a_L^Y	-8.8 GeV	5.1 GeV
a_L^Z	7.8 GeV	1.1 GeV
c_L^{TT}	16.0	6.5
c_L^{TX}	16.8	-18.3
c_L^{TY}	2.2	-28.9
c_L^{TZ}	-14.1	-7.7
c_L^{XX}	14.0	-0.45
c_L^{XY}	-5.5	0.63
c_L^{XZ}	-10.3	-7.7
c_L^{YY}	15.7	1.0
c_L^{YZ}	9.5	17.7
c_L^{ZZ}	3.1	-4.2

8.6. Fast Fourier Transform Method

The Fast Fourier Transform (FFT) is a numerical algorithm that is optimized to calculate the discrete Fourier transform (DFT) more efficiently than computing the DFT directly. Calculating the DFT of N points using the definition directly takes $\mathcal{O}(N^2)$ operations, whereas the FFT requires $\mathcal{O}(N\log_2 N)$ operations to calculate the same DFT [23]. The FFT computes the DFT in an optimized fashion and returns the same result as the direct evaluation of the DFT. The equation of the DFT is given by:

$$F[n] = F_{Re}[n] + iF_{Im}[n] = \sum_{k=0}^{N-1} f[k] e^{\frac{-2\pi i k n}{N}} \tag{8.2}$$

In general, $f[k]$ is a set of N complex numbers that is transformed into an N-periodic sequence of N complex numbers. N is often the number of samples taken of a given signal, $k : 0 \to N-1$ and $n : 0 \to N-1$. A FFT converts a sampled signal in the time domain into its

individual frequency components in the frequency domain. In eq. (8.2), k is associated with the discretized time interval ΔT and n is associated with angular frequency ω (incidentally, $F[n]$ may also be called the n^{th} Fourier mode). The FFT is used in many applications of the Fourier analysis, specifically when obtaining information about amplitudes associated with different harmonics of a known frequency appearing in a sampled time signal. Thus, it is a natural choice, given eq.(4.37), to utilize the FFT for the T2K LV analysis.

For the T2K LV analysis, $N = 32$. Squaring out Equation 4.37 will result in a total of four relevant sidereal time harmonics. Thus, the only parts of fourier space that are interesting for this analysis are $n : 0 \rightarrow 4$. To relate 4.37 to 8.2, k is associated with the discretized sidereal time interval $\Delta T_{\oplus}$ and n is associated with Earth's sidereal angular frequency $\omega_{\oplus}$. A FFT tool was developed specifically for the T2K LV analysis. The FFT tool transforms the aforementioned scaled event rate histograms (either for data or toy MC) and outputs a histogram of the real part, imaginary part, and magnitude of the FFT for further investigation. The equation for the magnitude of the FFT is:

$$MAG = |F[n]| = \sqrt{(F_{Re}[n])^2 + (F_{Im}[n])^2} \tag{8.3}$$

Since the SME coefficients only appear in the amplitudes associated with each sidereal time harmonic in eq. (4.37), the magnitude histograms are used for the LV search. The real and imaginary histograms are also outputted as checks for the magnitude histograms. Examples of each output histogram for the scaled INGRID flat Toy MC are shown in Figures 8.7 - 8.9:

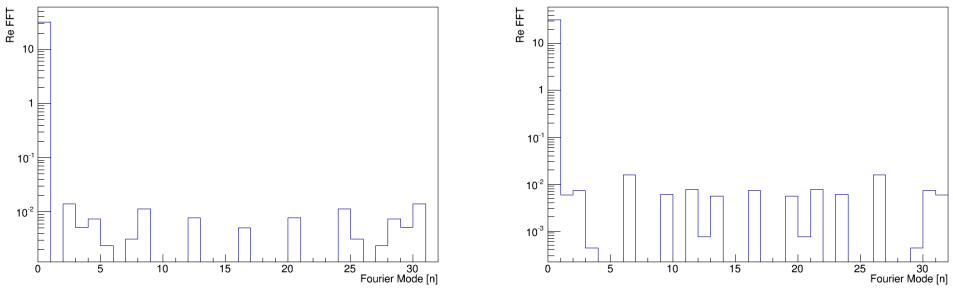

FIGURE 8.7. The real parts of the output of the FFT tool using scaled INGRID flat toy MC as input.

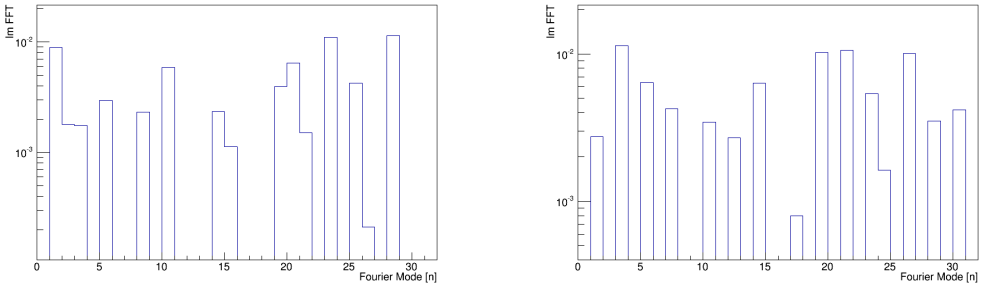

FIGURE 8.8. The imaginary parts of the output of the FFT tool using scaled INGRID flat toy MC as input.

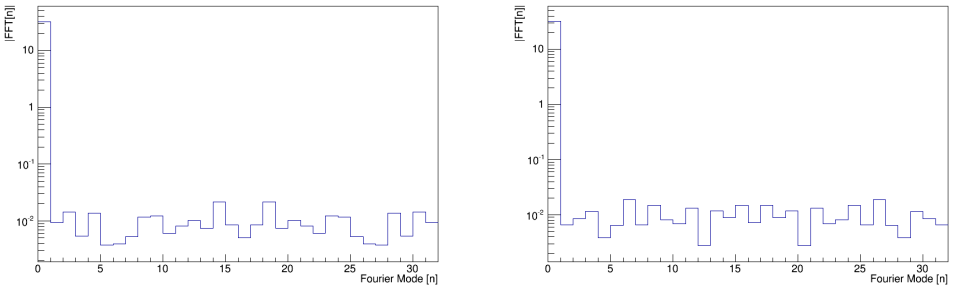

FIGURE 8.9. The magnitude of the output of the FFT tool using scaled INGRID flat toy MC as input.

Examples of each output histogram for the scaled ND280 flat Toy MC is shown in Figures 8.10 - 8.12:

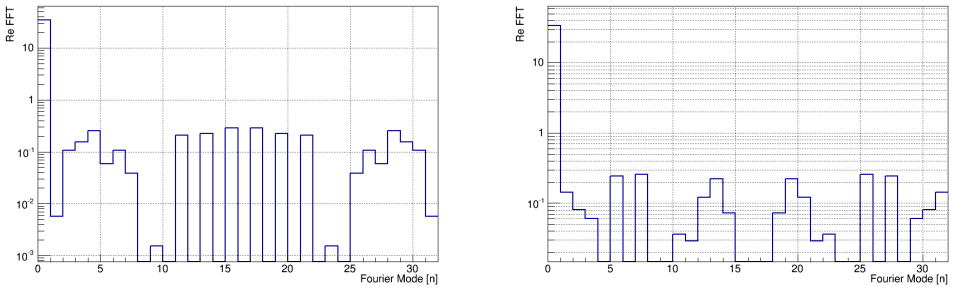

FIGURE 8.10. The real parts of the output of the FFT tool using scaled ND280 flat toy MC as input.

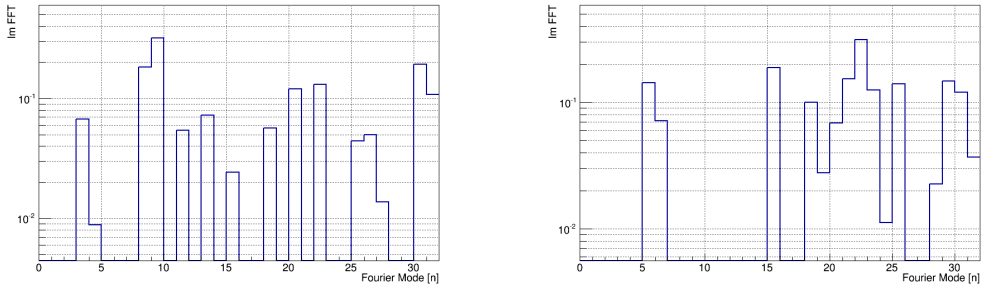

FIGURE 8.11. The imaginary parts of the output of the FFT tool using scaled ND280 flat toy MC as input.

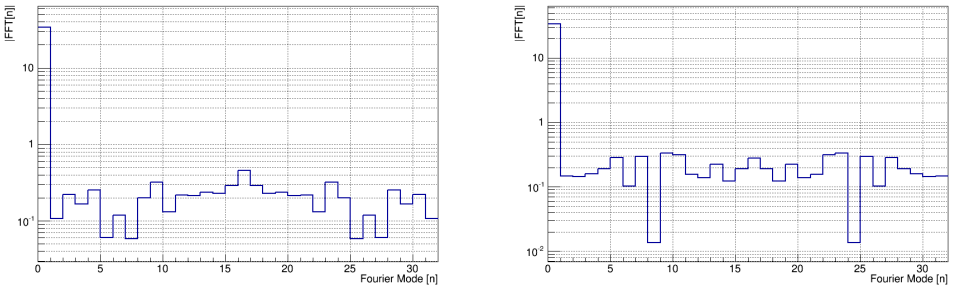

FIGURE 8.12. The magnitude of the output of the FFT tool using scaled ND280 flat toy MC as input.

8.7. Determining Significance of FFT

In order to determine the statistical significance of a particular signal Fourier mode from data, a hypothesis test is implemented. The null and alternative hypotheses are:

- H_o: For a given T2K detector, there is *no sidereal variation* in the signal Fourier modes in the data.
- H_A: For a given T2K detector, there *is a sidereal variation* in the signal Fourier modes in the data.

The significance for this search is 0.003, which corresponds to a 3σ variation in the data from the null hypothesis. For a given detector, the following procedure is performed to extract a nominal detection threshold for the signal Fourier modes (F[1], F[2], F[3], F[4]):

- Each toy MC histogram is scaled by the inverse of its own average event rate to avoid computational roundoff errors
- For each 10,000 toy MC, the amplitude of a given signal Fourier mode from a magnitude histogram is placed into a separate histogram
- The resulting distribution of signal Fourier mode amplitudes is integrated up to 99.7% of the distribution
- The corresponding value is taken as the nominal detection threshold for that particular Fourier mode

Figures 8.13 to 8.16 show the distribution of the different Fourier mode magnitudes in INGRID. Similar 3σ detection thresholds are expected as the variations in the toys are purely statistical.

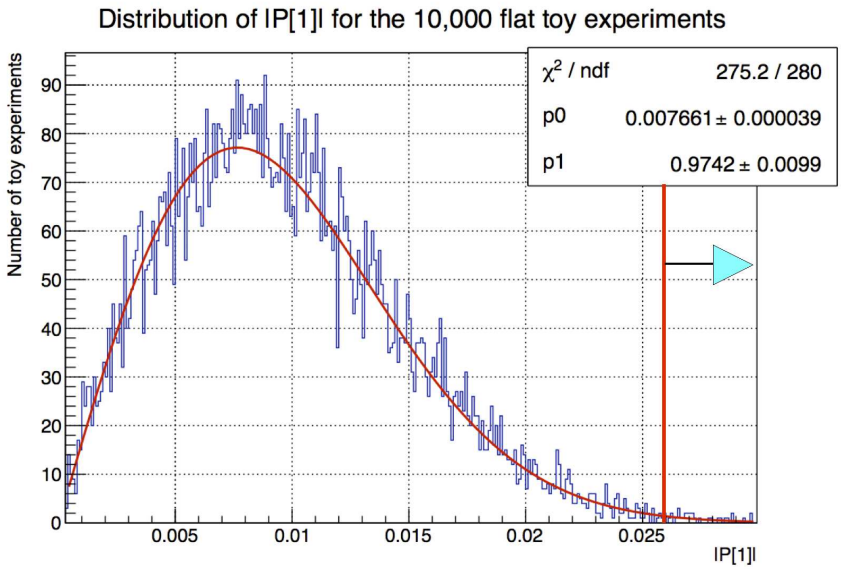

FIGURE 8.13. Distribution of the magnitude of the first Fourier mode for the 10,000 flat toy experiments of INGRID. The 3σ threshold is equal to 0.026 for this mode. The distribution is fitted with a Rayleigh function.

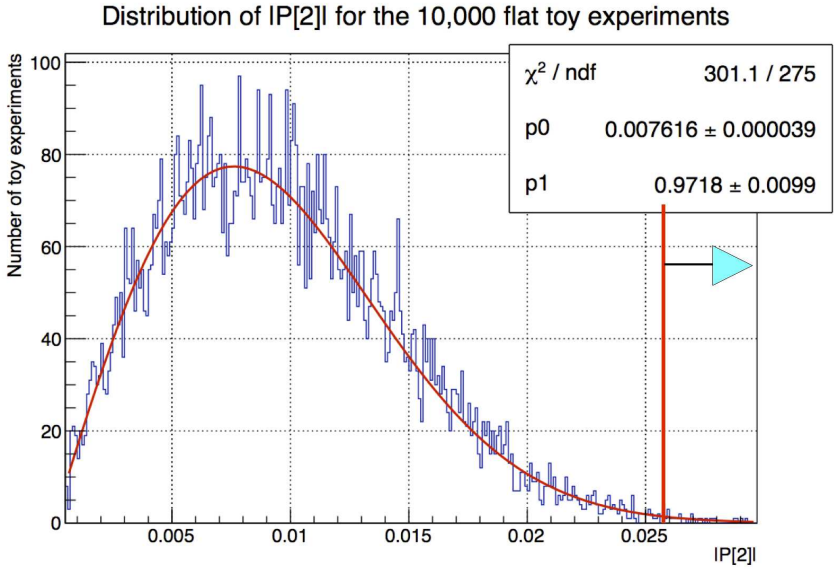

FIGURE 8.14. Distribution of the magnitude of the second Fourier mode for the 10,000 flat toy experiments of INGRID. The 3σ threshold is equal to 0.026 for this mode. The distribution is fitted with a Rayleigh function.

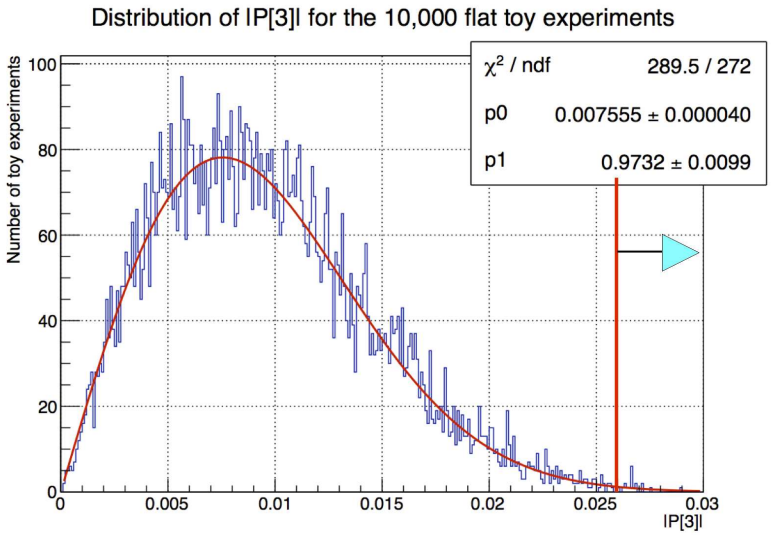

FIGURE 8.15. Distribution of the magnitude of the third Fourier mode for the 10,000 flat toy experiments of INGRID. The 3σ threshold is equal to 0.026 for this mode. The distribution is fitted with a Rayleigh function.

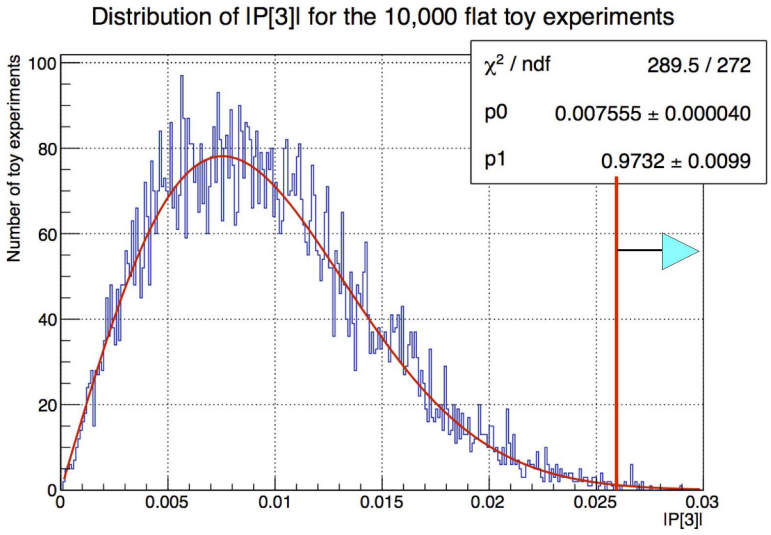

FIGURE 8.16. Distribution of the magnitude of the fourth Fourier mode for the 10,000 flat toy experiments of INGRID. The 3σ threshold is equal to 0.026 for this mode. The distribution is fitted with a Rayleigh function.

Figures 8.17 to 8.20 and Figures 8.21 to 8.24 show the distribution of the different Fourier mode magnitudes in the ND280 water-out and water-in samples respectively. Similar 3σ detection thresholds are expected as the variations in the toys are purely statistical.

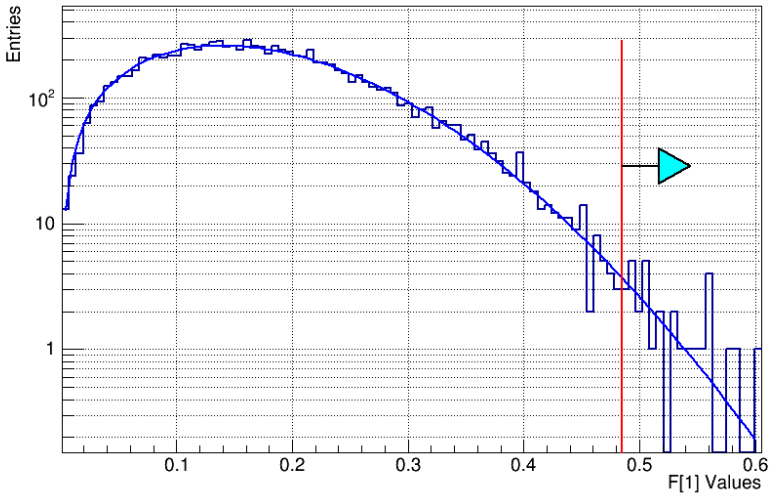

FIGURE 8.17. Distribution of the magnitude of the first Fourier mode for the 10,000 flat toy experiments for ND280 water-out. The distribution is fitted with a Rayleigh function.

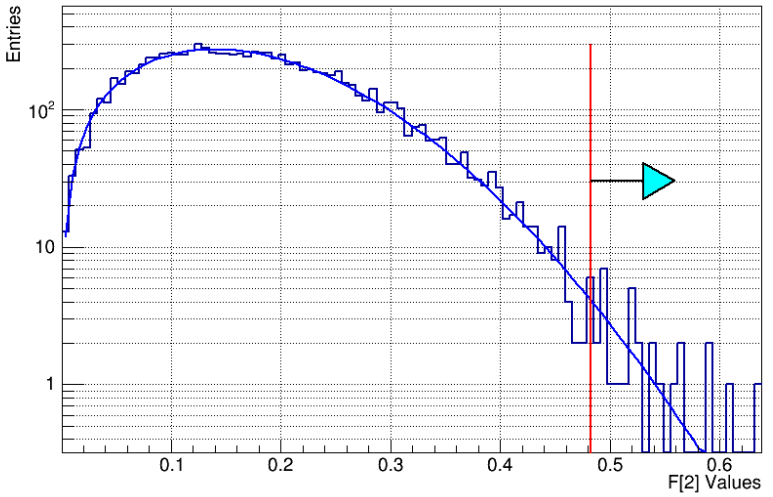

FIGURE 8.18. Distribution of the magnitude of the second Fourier mode for the 10,000 flat toy experiments for ND280 water-out. The distribution is fitted with a Rayleigh function.

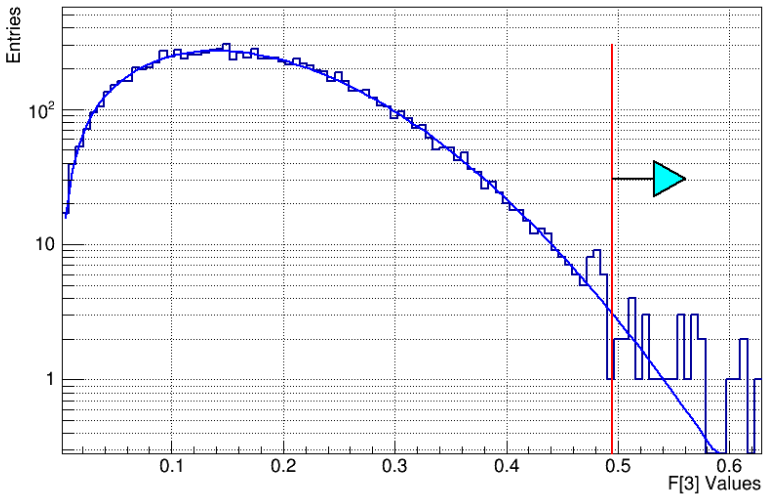

FIGURE 8.19. Distribution of the magnitude of the third Fourier mode for the 10,000 flat toy experiments for ND280 water-out. The distribution is fitted with a Rayleigh function.

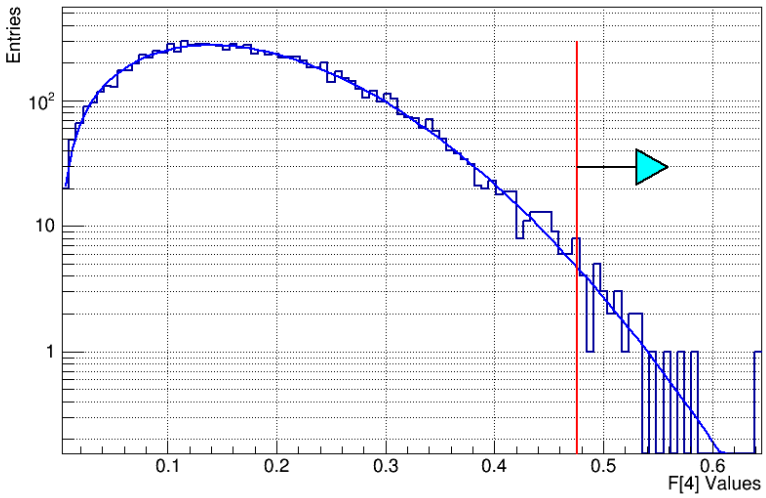

FIGURE 8.20. Distribution of the magnitude of the fourth Fourier mode for the 10,000 flat toy experiments for ND280 water-out. The distribution is fitted with a Rayleigh function.

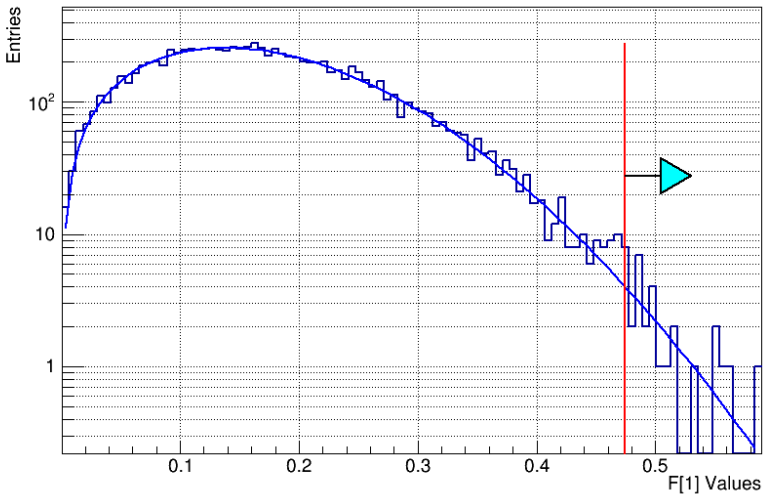

FIGURE 8.21. Distribution of the magnitude of the first Fourier mode for the 10,000 flat toy experiments for ND280 water-in. The distribution is fitted with a Rayleigh function.

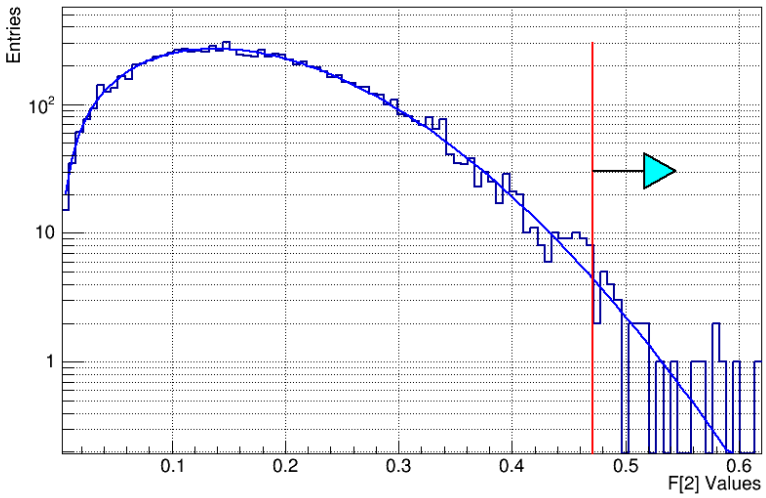

FIGURE 8.22. Distribution of the magnitude of the second Fourier mode for the 10,000 flat toy experiments for ND280 water-in. The distribution is fitted with a Rayleigh function.

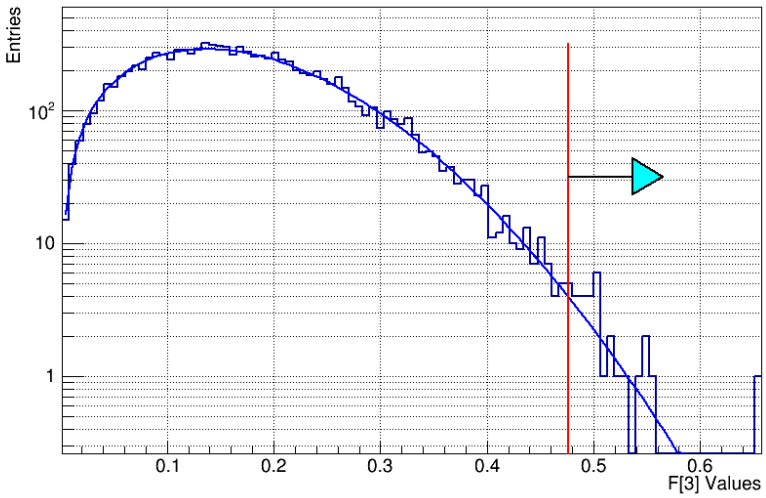

FIGURE 8.23. Distribution of the magnitude of the third Fourier mode for the 10,000 flat toy experiments for ND280 water-in. The distribution is fitted with a Rayleigh function.

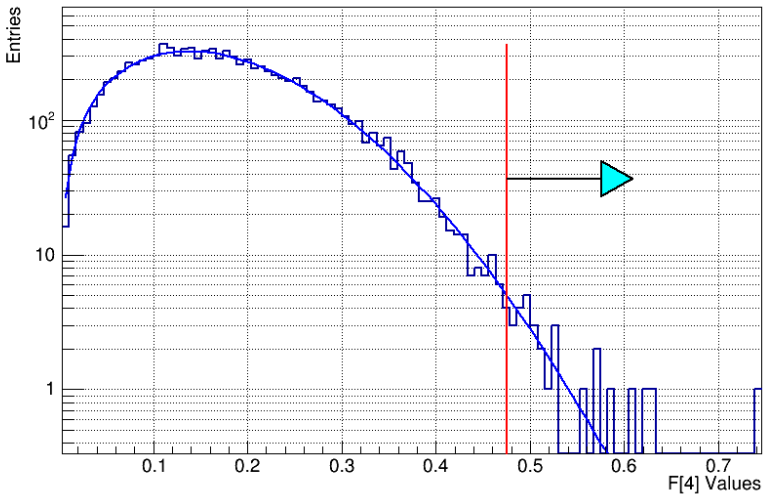

FIGURE 8.24. Distribution of the magnitude of the fourth Fourier mode for the 10,000 flat toy experiments for ND280 water-in. The distribution is fitted with a Rayleigh function.

Table 8.5 shows the nominal detection thresholds for each detector and the corresponding signal Fourier mode distributions:

TABLE 8.5. T2K near detector detection thresholds

Detector	F[1]	F[2]	F[3]	F[4]
INGRID	0.026	0.026	0.026	0.026
ND280 water-in	0.4745	0.4714	0.4765	0.4756
ND280 water-out	0.4852	0.4826	0.4946	0.4758

Thus, if an amplitude in any signal Fourier mode from data is greater than the corresponding detection threshold, the data is assumed to be inconsistent with a flat event rate (i.e. a sidereal variation is observed). This defines our detection criteria for a sidereal variation in the T2K data. A p-value is calculated to determine how likely the observed Fourier mode in data is due to a statistical fluctuation. The p-value for a given signal Fourier mode in data is given by:

$$p - value = \frac{N_{MC}^{T} \geq T_{DATA}}{\text{Total \# of Toys}} \tag{8.4}$$

Eq. (8.4) provides the probability that the observed value of a signal Fourier mode in data is due to a noise fluctuation. It is the probability of drawing a value for a particular signal Fourier mode from the parent distributions in Figure 8.13, for example, at least as large as found in the data. The numerator is the number of Fourier mode values for a given signal Fourier mode that are the same as or larger than the value found in data. The denominator is the total number of Toy MC generated (10,000 in this case).

8.8. COEFFICIENT CORRELATIONS

In previous experiments, the sensitivity to a given effect from a SME coefficient assumes the SME coefficients themselves are independent from one another. The following procedure

was implemented by previous experiments to extract 99.7%C.L. upper limits on each SME coefficient:

(1) Set all but one SME coefficient to zero

(2) Increase the size of the SME coefficient until the nominal threshold has been crossed

(3) Take the corresponding value of the coefficient as the upper limit

However, in the T2K LV analysis, dependency between SME coefficients was studied by looking for possible 2 point correlations between coefficients. The following method was used:

(1) Set all coefficients to 0

(2) Select two coefficients A and B to be studied.

(3) Increase the value of A by a given step

(4) Produce a toy MC with the effects of A and B included in the toy

(5) Apply the FFT on the obtained toy histogram and check if any nominal thresholds are crossed. If not, increase A by the same step size and repeat to Step 4

(6) If any nominal threshold is crossed, fill a 2D histogram with the values of A and B

(7) Set the value of A to 0 again and change B value by the given step size

(8) Repeat the procedure with the new values of A and B starting at step 4

The results found for two coefficients shown in Figure 8.25 indicate that the sensitivity estimation of most coefficients depends on the values of other coefficients. Though only two cases are shown, most of the coefficients behave similarly as in Figure 8.25. The larger the limit on the B coefficient ($(a_L)^Y_{ab}$) is, the lower the limit is on the A coefficient ($(a_L)^X_{ab}$). Thus, T2K's 3σ sensitivity to these coefficients is higher. A pair of coefficients that exhibit this type of dependence are said to be "anti-correlated", though the correlation only comes from the detection threshold and is in no way strictly theoretical. In this case, assuming each

coefficient is zero except for the studied pair tends to artificially increase T2K's sensitivity, allowing smaller limits to be set on the studied coefficient pair.

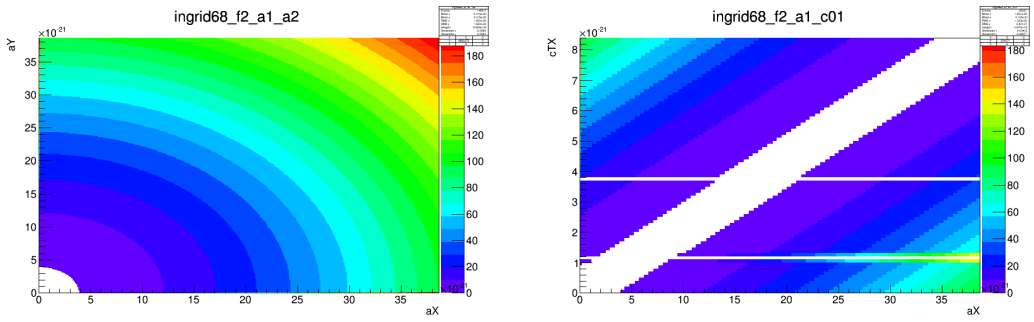

FIGURE 8.25. "Anti-correlation" (left) and "correlation" (right) plots for various SME coefficients using the procedure outlined above. The Z-axis is the ratio of a signal Fourier mode amplitude for a given pair of coefficient values and the 68 % C.L. nominal threshold.

On the other hand, for a few coefficient pairs such as $(c_L)^{TX}_{ab}$ and $(a_L)^{X}_{ab}$ (shown on Figure 8.25), the larger the B coefficient is ($(c_L)^{TX}_{ab}$ in this case), the higher the limit will be on the A coefficient ($(a_L)^{X}_{ab}$). A pair of coefficients that exhibit this type of dependence are said to be "correlated". In this case, assuming each coefficients to be 0 except for a given pair artificially under-estimates T2K's sensitivity, allowing larger limits to be set on the studied coefficient pair. Though the case of "correlated" coefficients is conservative, the case of "anti-correlated" coefficients is much more problematic. "Anti-correlation" indicates that the method outlined above for parameter estimation should not be used to accurately determine coefficient limits, even though it gives an order of magnitude estimation of the sensitivity to a given coefficient pair. Instead, a direct fit without fixing any coefficients is performed. Such a fit is presented in section 8.9.

8.9. Binned Likelihood Fit

Initially, a full fourteen-coefficient binned likelihood fit was desired to extract limits on the SME coefficients. However, due to the large degree of correlation (as shown in Section 8.8) and a large degeneracy in the fitter program, a five coefficient binned likelihood fit was developed. The five coefficients that are fit for each T2K near detector are the amplitudes associated with each sidereal time harmonic from equation 4.37. The five coefficients are:

(1) $(\mathcal{C})_{ab}$

(2) $(\mathcal{A}_s)_{ab}$

(3) $(\mathcal{A}_c)_{ab}$

(4) $(\mathcal{B}_s)_{ab}$

(5) $(\mathcal{B}_c)_{ab}$

As with the FFT method, these coefficients are assumed to be real although in general they may be complex. Although a binned likelihood fit ultimately results in loss of information in each LSP bin, the high statistical samples of INGRID negates the differences in binned and unbinned likelihood methods. In addition, the goodness of fit can easily be determined for the binned likelihood method. A binning of 32 bins in LSP was chosen for the likelihood fit, just as in the FFT method. For each LSP bin, the statistical errors are assumed to be Gaussian. From this, the likelihood may be constructed as:

$$L = \prod_{i=1}^{32} e^{-\frac{(d_i - m_i)^2}{2\sigma_i^2}} \tag{8.5}$$

Here, d_i and m_i are the POT normalized number of events in the i^{th} LSP bin and

$$\sigma_i = \frac{N_{\nu_\mu}}{N_{\mathrm{POT}}} \sqrt{\frac{\delta N_{\nu_\mu}^2}{N_{\nu_\mu}^2} + \frac{\delta N_{\mathrm{POT}}^2}{N_{\mathrm{POT}}^2}}, \tag{8.6}$$

where where N_{ν_μ} and N_{POT} are, respectively, the number of neutrino events and the number of protons on target in LSP bin i, with δN_{ν_μ} and δN_{POT} the corresponding errors.

The sections below describe tests that were taken to evaluate:

(1) That the fitter is unbiased

(2) That the error is correctly estimated

(3) That the goodness of fit is reasonable

8.9.1. One Coefficient Fit Tests. Several points in the coefficient space were selected to test if the fitter is unbiased and if the error estimation is correct. The origin of the coefficient space (0,0,0,0,0) and two other points described in Table 8.6 were selected.

A set of Toy MC were generated by setting the 5 SME coefficients to a fixed "true" value. The LV probability for ν_μ disappearance is then scaled by the average number of POT. The pull distribution is evaluated by:

(1) The $\frac{\text{events}}{\text{POT}}$ is varied within the gaussian statistical error from data in each LSP bin.

(2) In sequence, for each coefficient the associated distribution is fitted by fixing all but one coefficient to its true value.

The pull distributions are generated by repeating this procedure 10,000 times and then calculating the $\frac{\text{Fit-True}}{\text{Error}}$ distributions. The results for INGRID for each point chosen in coefficient space are shown in Figures 8.26 to 8.29, 8.30 to 8.34, and 8.35 to 8.39 and summarized in Table 8.6. The results confirm that the fitter is unbiased and that the error is correctly estimated.

Figures 8.26 to 8.29 shows the case for no LV signal. The peak around 0 is expected as the fitter is unable to fit some sine or cosine distribution with opposite phase. Additionally, no pull distribution is created for $(\mathcal{C})_{ab}$ because when all parameters are 0 except $(\mathcal{C})_{ab}$, a flat

LSP distribution is fitted and thus only a normalization difference. The fitter is normalization independent to avoid certain systematics (i.e. estimation of neutrino flux), so there is no point in fitting $(\mathcal{C})_{ab}$ for the case when all other parameters are zero. In the case of all but one coefficient set to zero, the probability becomes

$$P_{\nu_\mu \to \nu_x} = 1 - (\frac{L}{hc})^2 |A_c^{\mu\ x} \cos(\omega_\oplus T_\oplus)|^2. \tag{8.7}$$

In the event of a signal of the form $1-(\frac{L}{hc})^2|A_c^{\mu\ x}\cos(\omega_\oplus T_\oplus)|^2$, the fitter cannot find negative values of $|A_c^{\mu x}|^2$. In this case, the fitter naturally converges to zero. A depletion of events between values of 0.4 and 1.0 is also noticeable. For the fitter, the limiting factor is the normalization. The fitter hits the machine precision limitation when estimating the likelihood variations since the sensitivity to the normalization is relatively small. Because of this, the error is overestimated creating an artificial drop in the pull distributions.

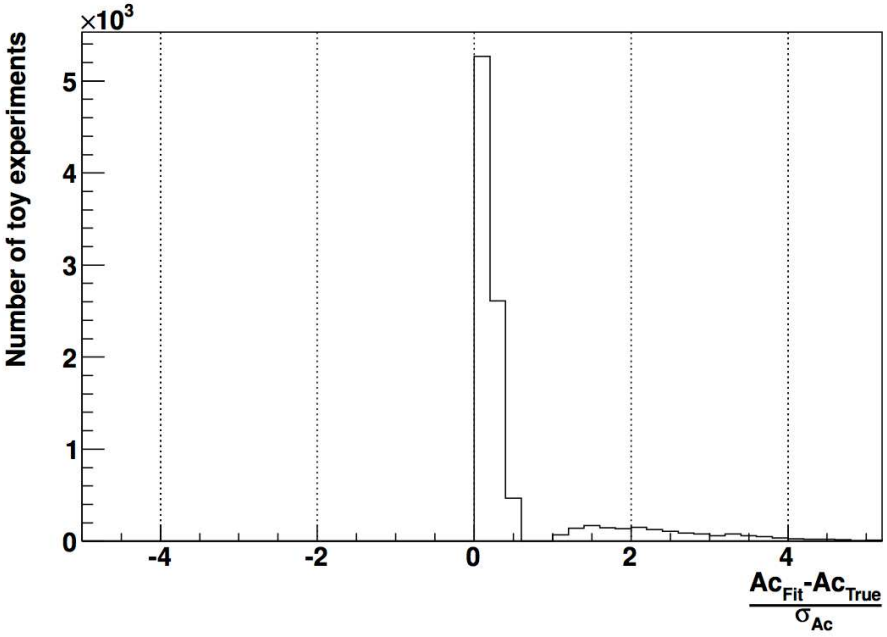

FIGURE 8.26. Pull distributions for the $\mathcal{A}_c$ coefficient in case of no LV signal in INGRID ($(\mathcal{C})_{ab}=0$, $(\mathcal{A}_c)_{ab}=0$, $(\mathcal{A}_s)_{ab}=0$, $(\mathcal{B}_c)_{ab}=0$, $(\mathcal{B}_s)_{ab}=0$).

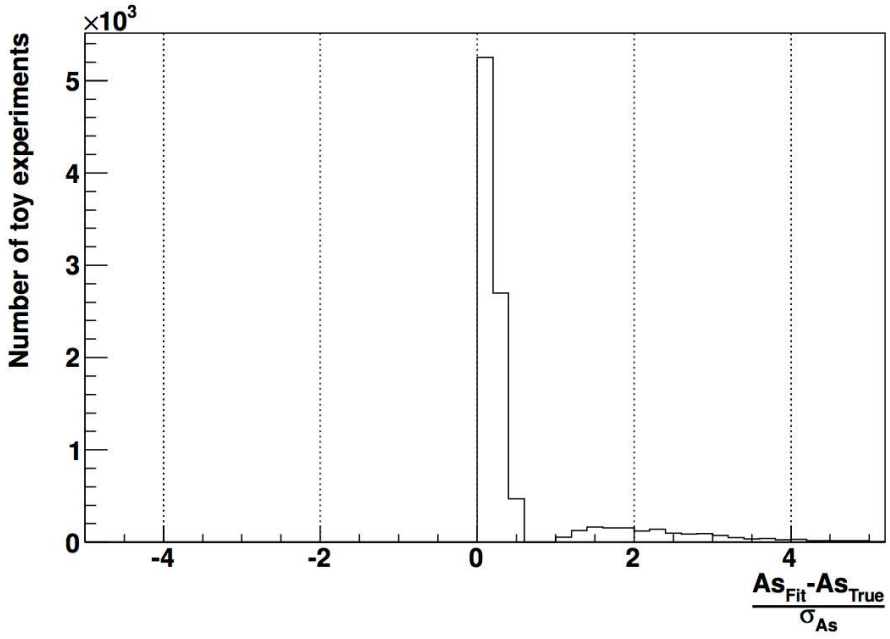

FIGURE 8.27. Pull distributions for the $\mathcal{A}_s$ coefficient in case of no LV signal in INGRID ($(\mathcal{C})_{ab} = 0$, $(\mathcal{A}_c)_{ab} = 0$, $(\mathcal{A}_s)_{ab} = 0$, $(\mathcal{B}_c)_{ab} = 0$, $(\mathcal{B}_s)_{ab} = 0$).

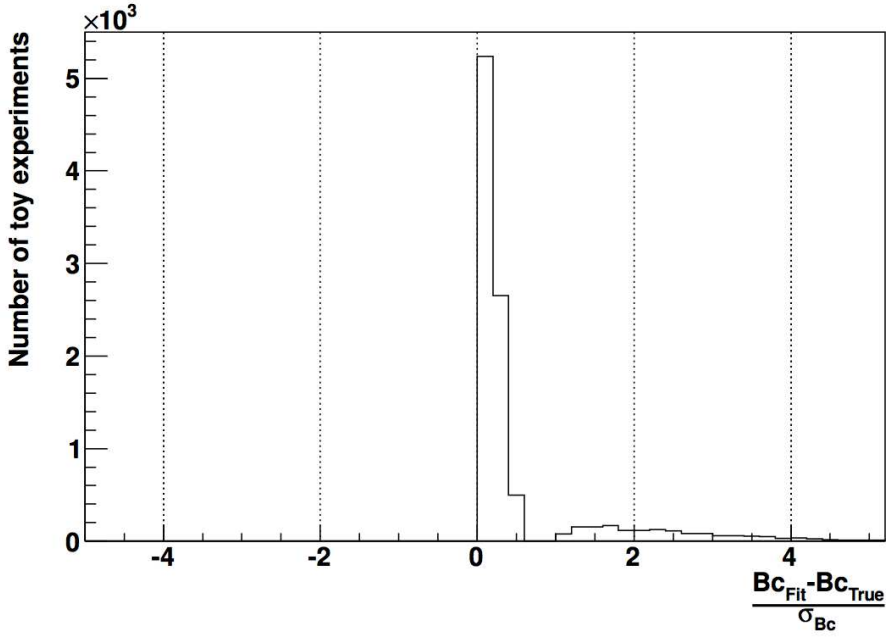

FIGURE 8.28. Pull distributions for the $\mathcal{B}_c$ coefficient in case of no LV signal in INGRID ($(\mathcal{C})_{ab} = 0$, $(\mathcal{A}_c)_{ab} = 0$, $(\mathcal{A}_s)_{ab} = 0$, $(\mathcal{B}_c)_{ab} = 0$, $(\mathcal{B}_s)_{ab} = 0$).

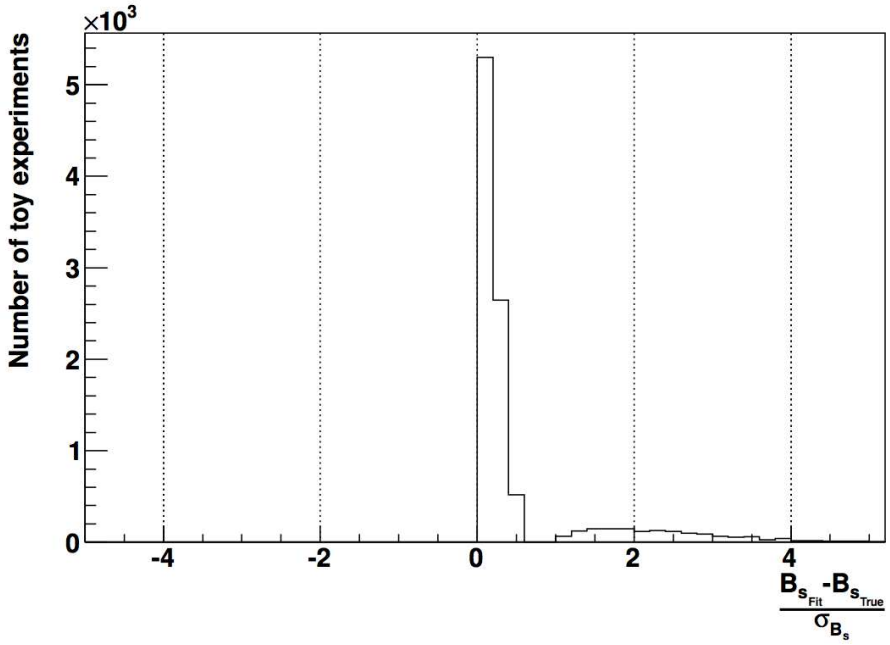

FIGURE 8.29. Pull distributions for the $\mathcal{B}_s$ coefficient in case of no LV signal in INGRID ($(\mathcal{C})_{ab} = 0$, $(\mathcal{A}_c)_{ab} = 0$, $(\mathcal{A}_s)_{ab} = 0$, $(\mathcal{B}_c)_{ab} = 0$, $(\mathcal{B}_s)_{ab} = 0$).

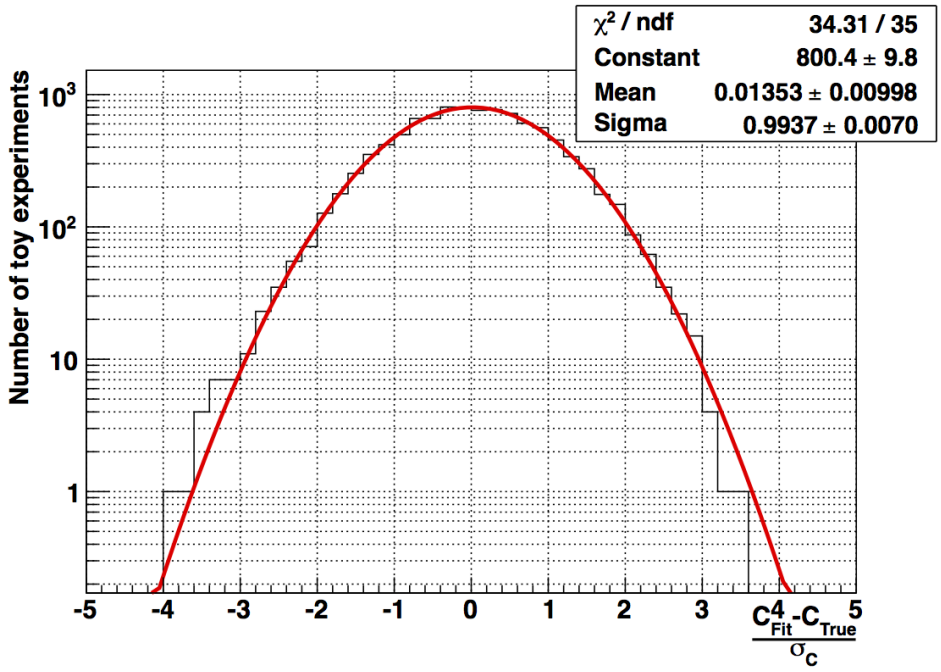

FIGURE 8.30. INGRID pull distributions for the fit of the $\mathcal{C}$ coefficient, with $(\mathcal{C})_{ab} = 10^{-20}$, $(\mathcal{A}_c)_{ab} = 10^{-21}$, $(\mathcal{A}_s)_{ab} = 10^{-20}$, $(\mathcal{B}_c)_{ab} = 10^{-20}$, $(\mathcal{B}_s)_{ab} = 10^{-20}$.

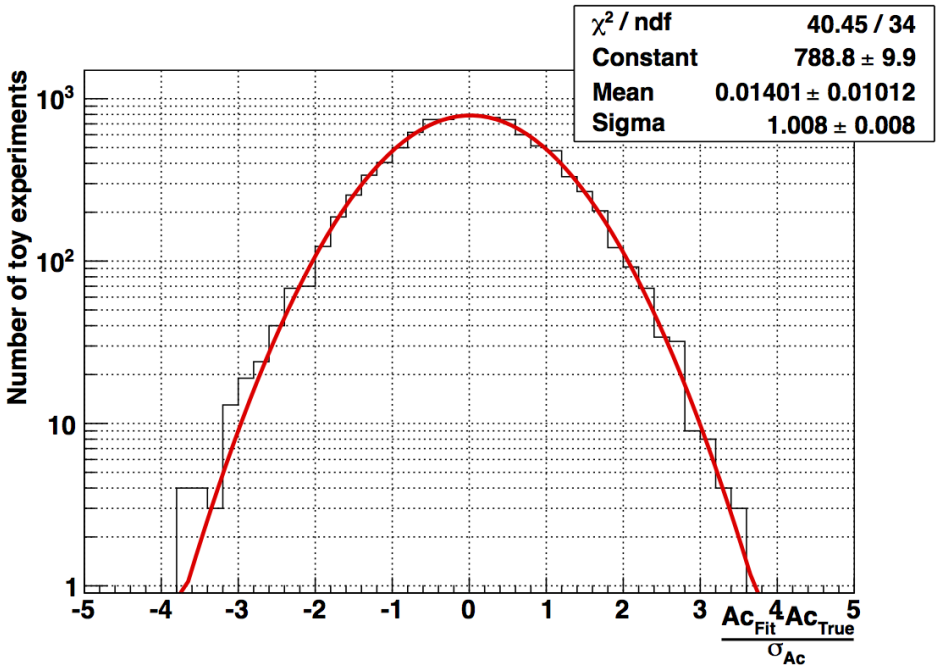

FIGURE 8.31. INGRID pull distributions for the fit of the $\mathcal{A}_c$ coefficient, with $(\mathcal{C})_{ab} = 10^{-20}$, $(\mathcal{A}_c)_{ab} = 10^{-21}$, $(\mathcal{A}_s)_{ab} = 10^{-20}$, $(\mathcal{B}_c)_{ab} = 10^{-20}$, $(\mathcal{B}_s)_{ab} = 10^{-20}$.

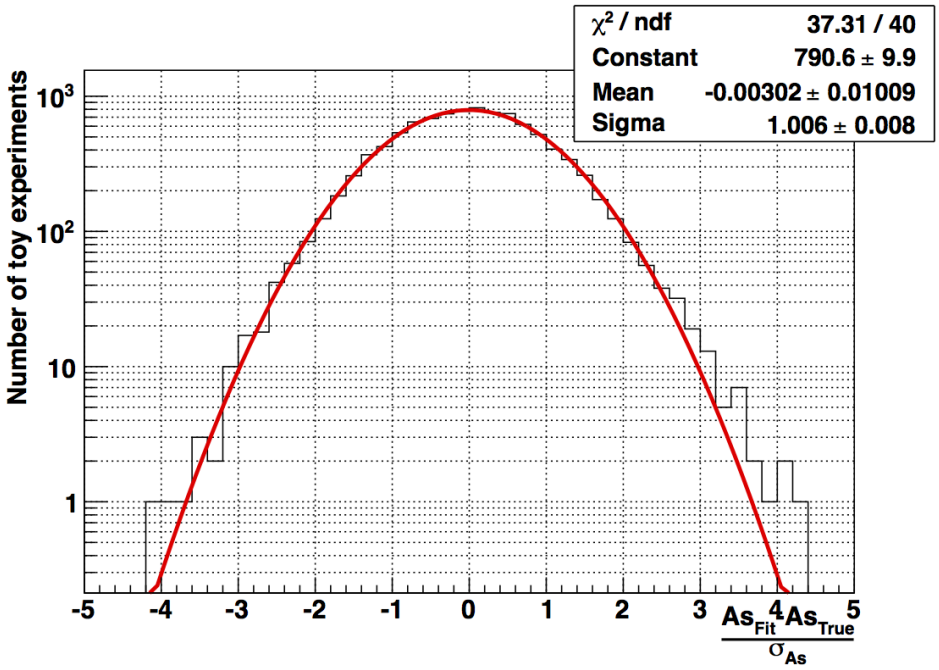

FIGURE 8.32. INGRID pull distributions for the fit of the $\mathcal{A}_s$ coefficient, with $(\mathcal{C})_{ab} = 10^{-20}$, $(\mathcal{A}_c)_{ab} = 10^{-21}$, $(\mathcal{A}_s)_{ab} = 10^{-20}$, $(\mathcal{B}_c)_{ab} = 10^{-20}$, $(\mathcal{B}_s)_{ab} = 10^{-20}$.

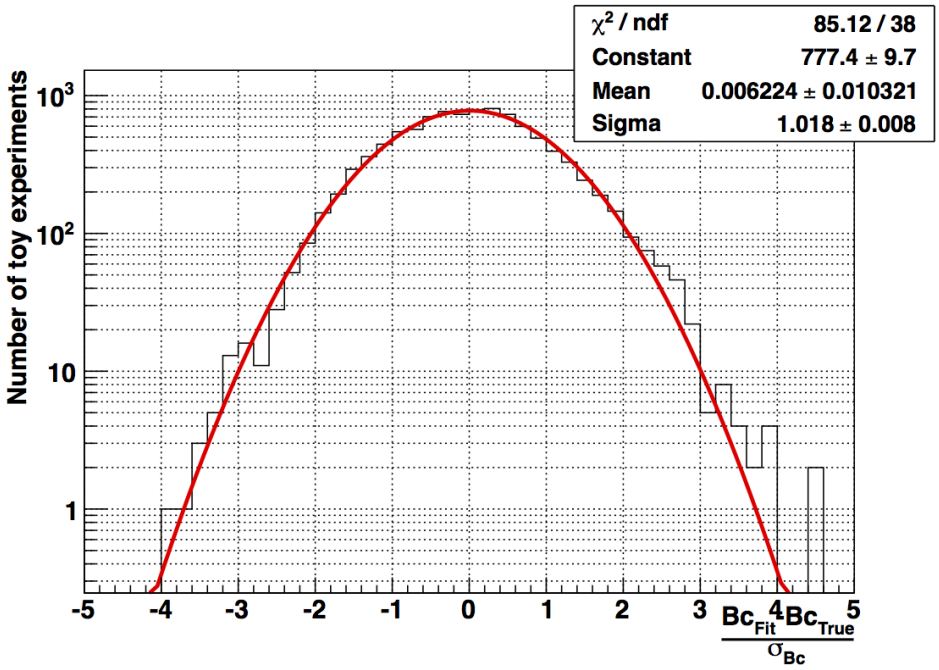

FIGURE 8.33. INGRID pull distributions for the fit of the $\mathcal{B}_c$ coefficient, with $(\mathcal{C})_{ab} = 10^{-20}$, $(\mathcal{A}_c)_{ab} = 10^{-21}$, $(\mathcal{A}_s)_{ab} = 10^{-20}$, $(\mathcal{B}_c)_{ab} = 10^{-20}$, $(\mathcal{B}_s)_{ab} = 10^{-20}$.

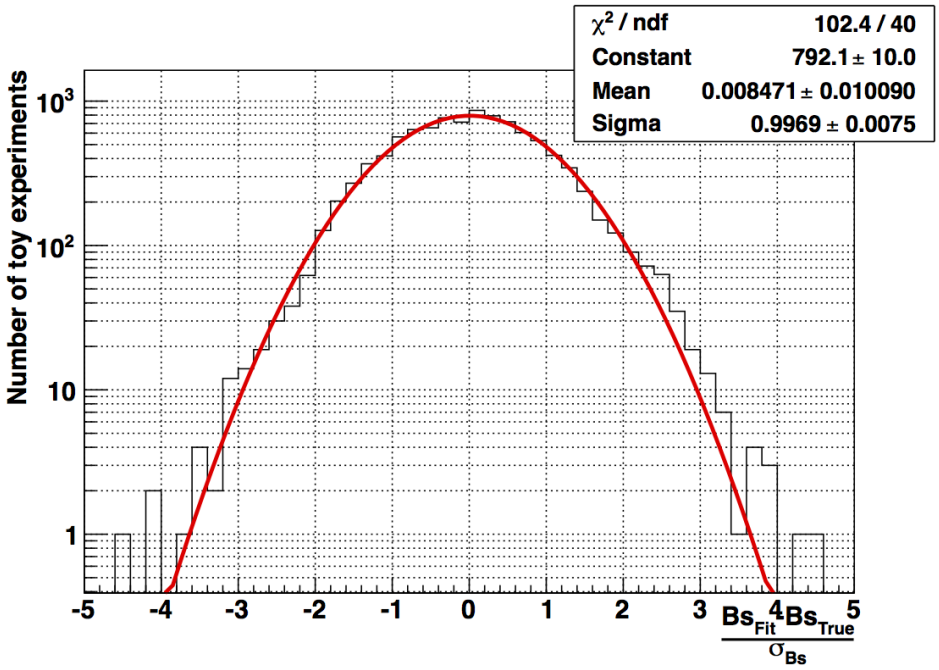

FIGURE 8.34. INGRID pull distributions for the fit of the $\mathcal{B}_s$ coefficient, with $(\mathcal{C})_{ab} = 10^{-20}$, $(\mathcal{A}_c)_{ab} = 10^{-21}$, $(\mathcal{A}_s)_{ab} = 10^{-20}$, $(\mathcal{B}_c)_{ab} = 10^{-20}$, $(\mathcal{B}_s)_{ab} = 10^{-20}$.

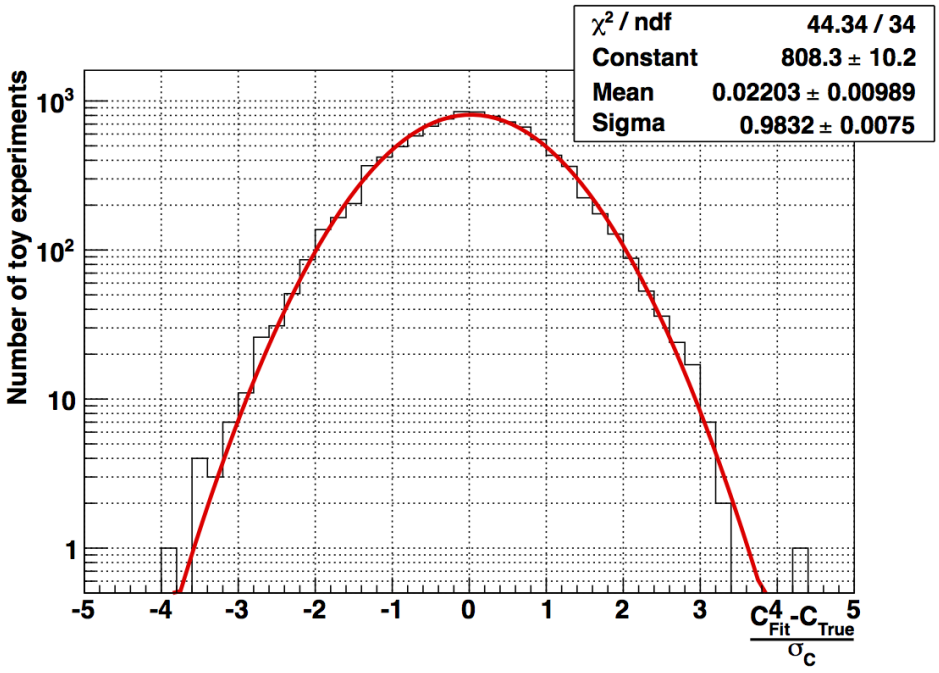

FIGURE 8.35. INGRID pull distributions for the $\mathcal{C}$ coefficient, with $(\mathcal{C})_{ab} = 5.10^{-21}$, $(\mathcal{A}_c)_{ab} = 6.10^{-21}$, $(\mathcal{A}_s)_{ab} = 7.10^{-21}$, $(\mathcal{B}_c)_{ab} = 8.10^{-21}$, $(\mathcal{B}_s)_{ab} = 9.10^{-21}$.

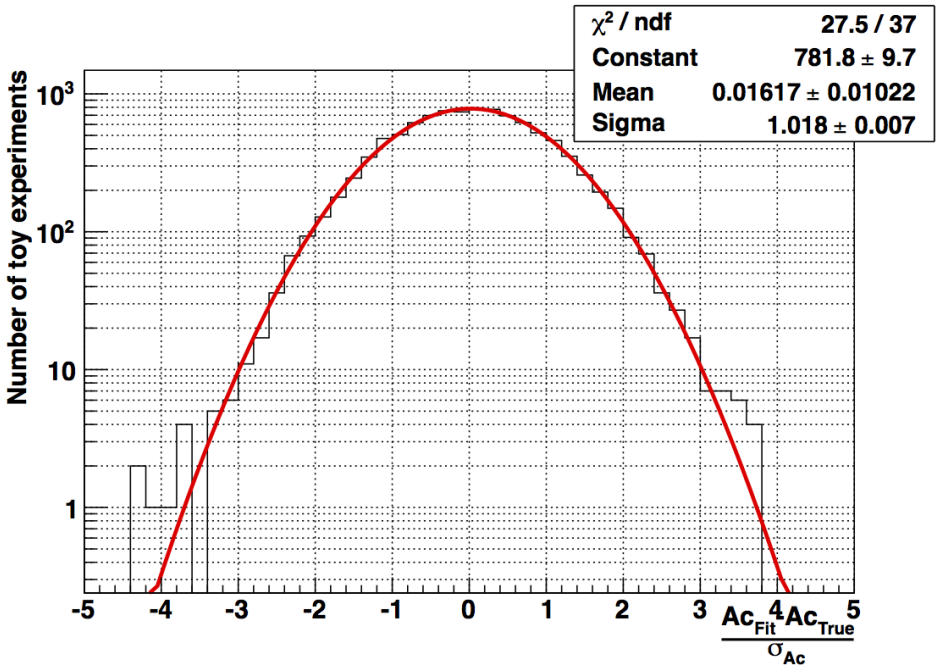

FIGURE 8.36. INGRID pull distributions for the $\mathcal{A}_c$ coefficient, with $(\mathcal{C})_{ab} = 5.10^{-21}$, $(\mathcal{A}_c)_{ab} = 6.10^{-21}$, $(\mathcal{A}_s)_{ab} = 7.10^{-21}$, $(\mathcal{B}_c)_{ab} = 8.10^{-21}$, $(\mathcal{B}_s)_{ab} = 9.10^{-21}$.

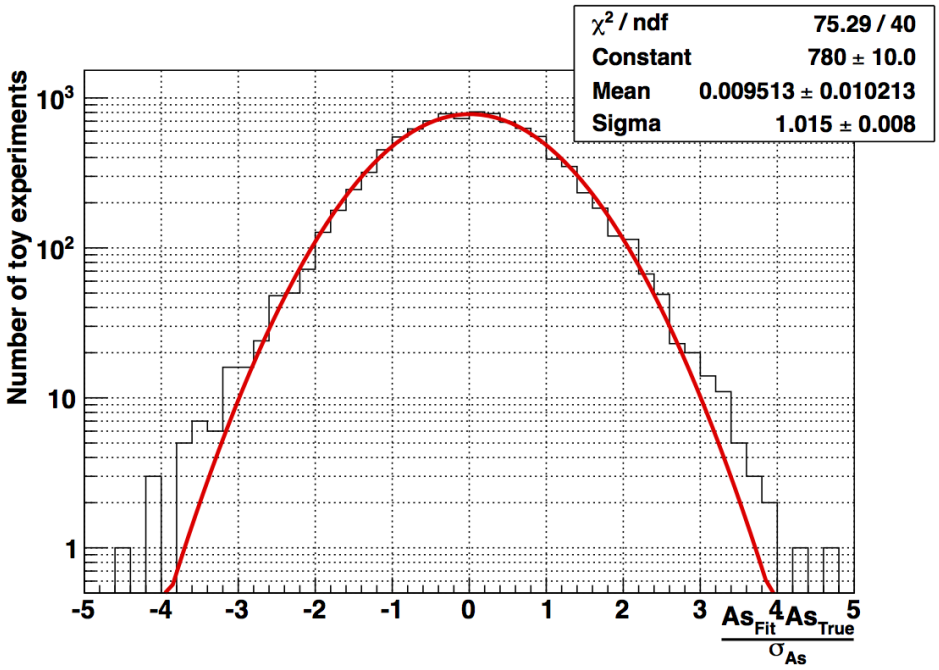

FIGURE 8.37. INGRID pull distributions for the $\mathcal{A}_s$ coefficient, with $(\mathcal{C})_{ab} = 5.10^{-21}$, $(\mathcal{A}_c)_{ab} = 6.10^{-21}$, $(\mathcal{A}_s)_{ab} = 7.10^{-21}$, $(\mathcal{B}_c)_{ab} = 8.10^{-21}$, $(\mathcal{B}_s)_{ab} = 9.10^{-21}$.

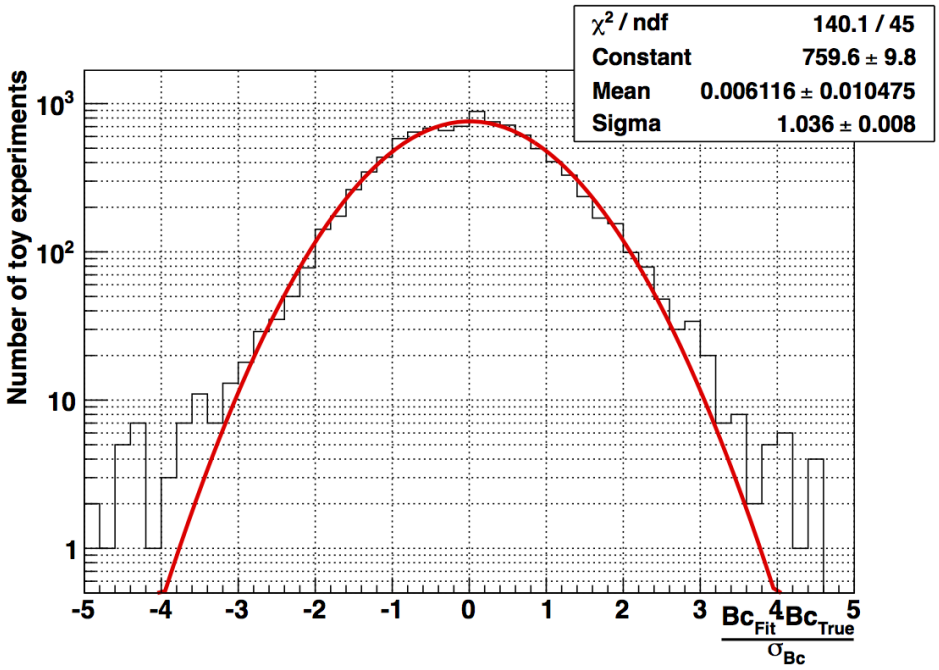

FIGURE 8.38. INGRID pull distributions for the $\mathcal{B}_c$ coefficient, with $(\mathcal{C})_{ab} = 5.10^{-21}$, $(\mathcal{A}_c)_{ab} = 6.10^{-21}$, $(\mathcal{A}_s)_{ab} = 7.10^{-21}$, $(\mathcal{B}_c)_{ab} = 8.10^{-21}$, $(\mathcal{B}_s)_{ab} = 9.10^{-21}$.

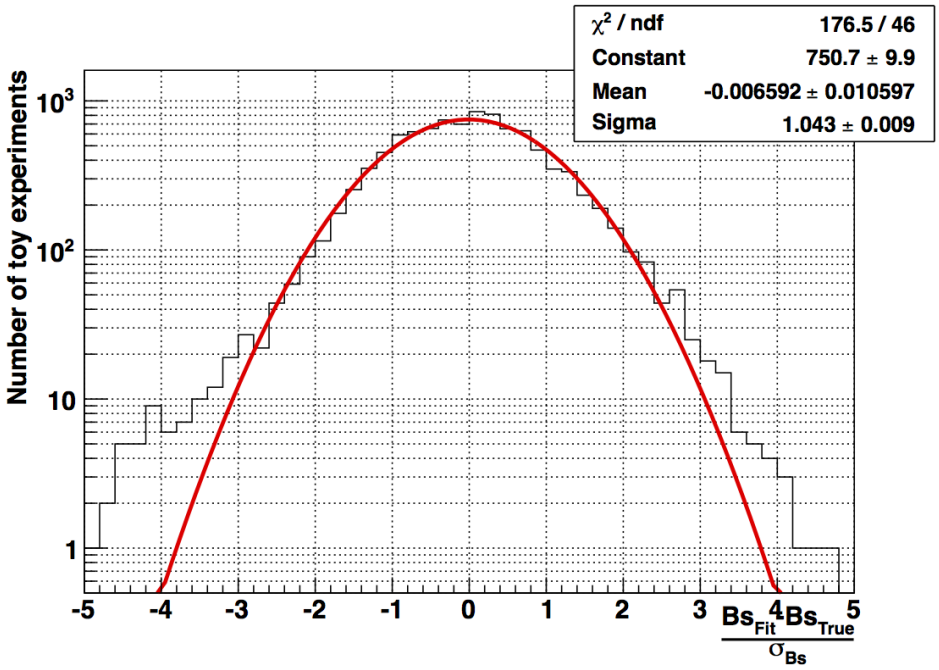

FIGURE 8.39. INGRID pull distributions for the $\mathcal{B}_s$ coefficient, with $(\mathcal{C})_{ab} = 5.10^{-21}$, $(\mathcal{A}_c)_{ab} = 6.10^{-21}$, $(\mathcal{A}_s)_{ab} = 7.10^{-21}$, $(\mathcal{B}_c)_{ab} = 8.10^{-21}$, $(\mathcal{B}_s)_{ab} = 9.10^{-21}$.

TABLE 8.6. INGRID pull distributions bias of the mean (compatibility with 0) and error estimation (compatibility with 1) by the fitter.

$(C,\ A_c,\ A_s,\ B_c,\ B_s)$ value	Mean compatibility (in σ)	1σ error compatibility (in σ)
$(10, 1, 10, 10, 10) \times 10^{-20}$	$(0.4, 0.9, 0.2, 0.1, 0.6)$	$(0.1, 2.0, 0.8, 0.1, 0.1)$
$(5, 6, 7, 8, 9) \times 10^{-21}$	$(0.5, 1.2, 0.2, 0.7, 0.7)$	$(1.4, 2.5, 0.8, 1.0, 0.4)$

8.9.2. FIVE COEFFICIENT FIT TESTS. 10,000 signal toy experiments for each detector were built to test the 5-coefficient fitter in order to determine its robustness and error estimation. These toys were built by inserting a random LV signal based upon random values of the 5 coefficients into the flat toys.

The robustness of the fitter was tested by using various toy experiments with different LV signals and a statistical error fluctuation according to data. Figures 8.40 to 8.44 shows the results for these 10,000 toys. The coefficients were varied randomly over the range $0 \rightarrow 5 \times 10^{-20}$. The robustness of the fitter is confirmed by the general agreement between the fitted and trues values. In addition to this, the agreement does not depend on the true

value of the coefficient. However, there does exist single points where the fitted and the true values for not correspond. This is most likely due to the high degree of correlation between the coefficients. Despite this, the fitter error covers these differences.

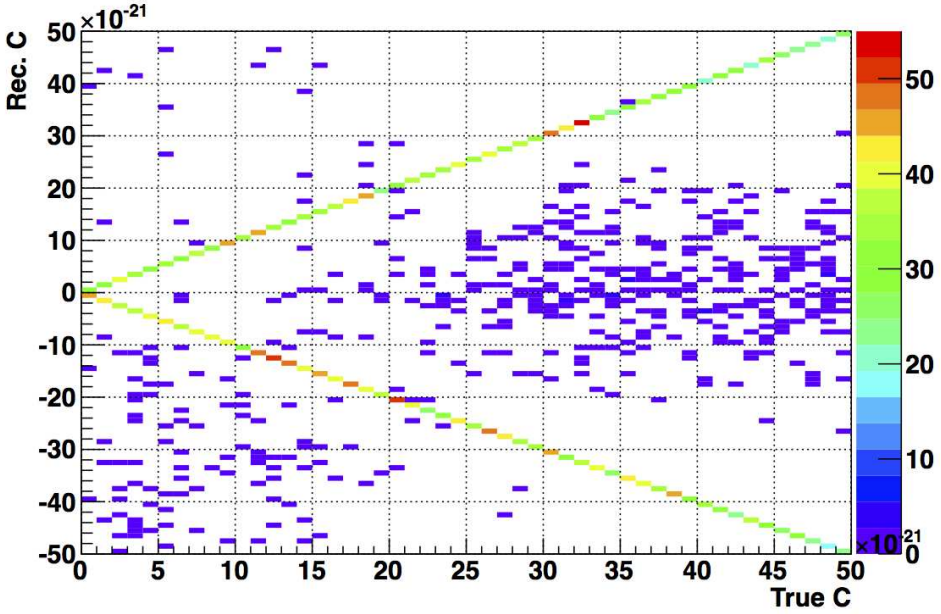

FIGURE 8.40. Fitted value versus true value of the coefficient $\mathcal{C}$, using the 5-coefficient fit for various LV signals.

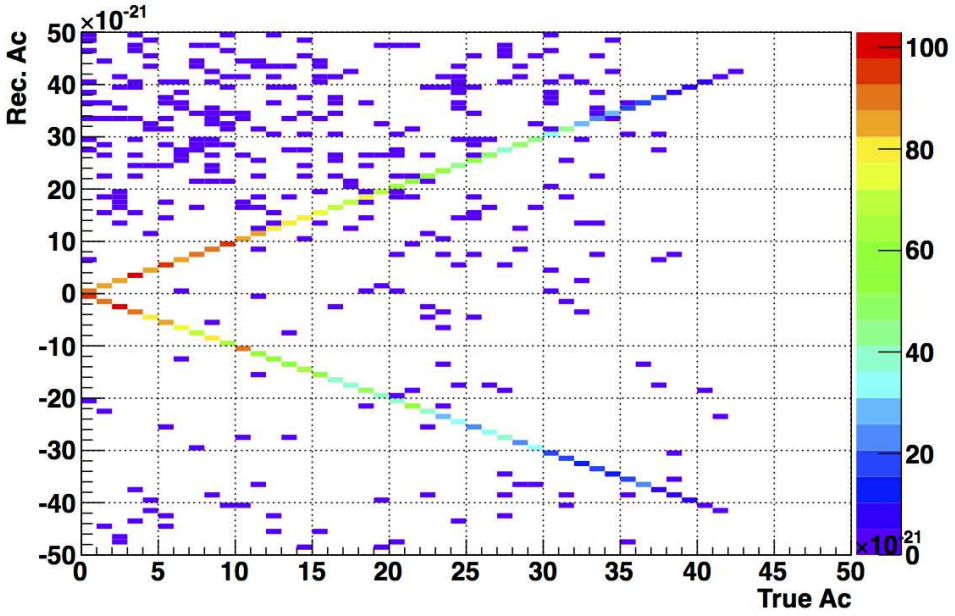

FIGURE 8.41. Fitted value versus true value of the coefficient $\mathcal{A}_c$, using the 5-coefficient fit for various LV signals.

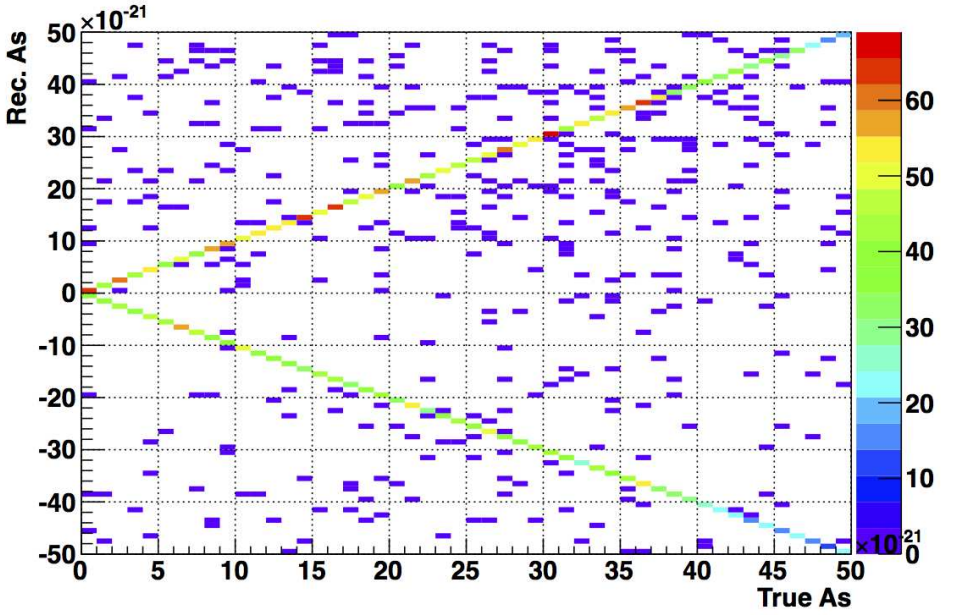

FIGURE 8.42. Fitted value versus true value of the coefficient $\mathcal{A}_s$, using the 5-coefficient fit for various LV signals.

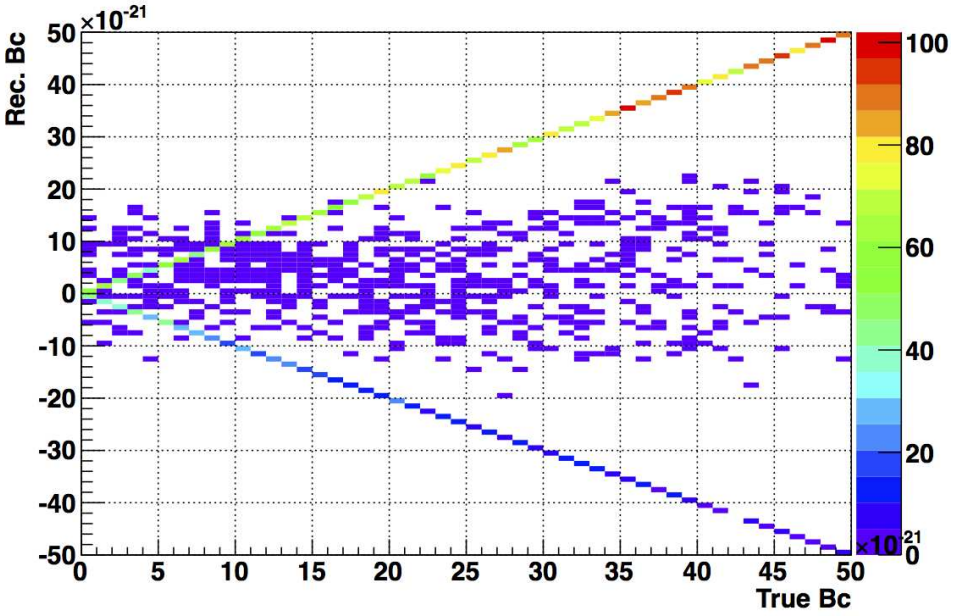

FIGURE 8.43. Fitted value versus true value of the coefficient $\mathcal{B}_c$, using the 5-coefficient fit for various LV signals.

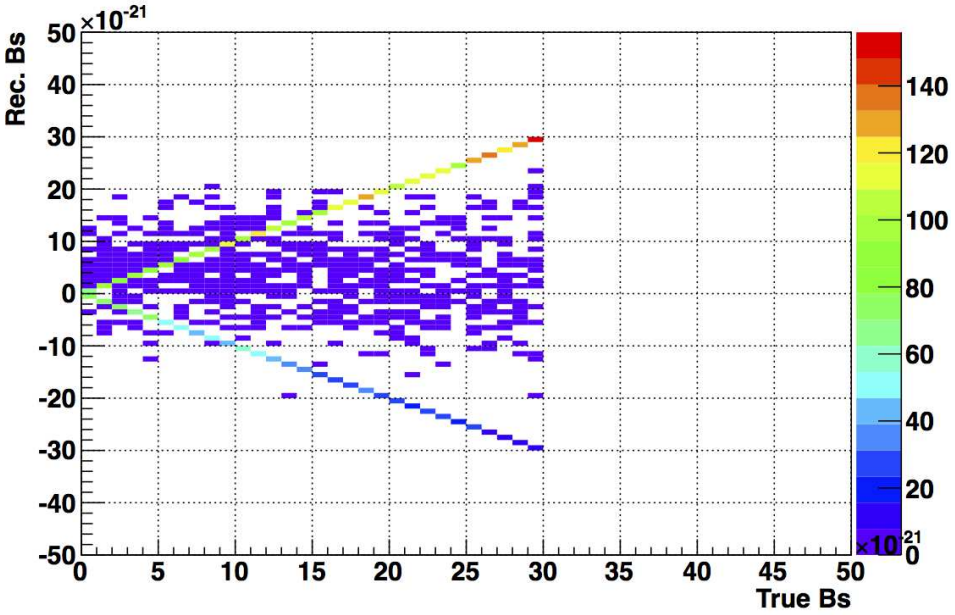

FIGURE 8.44. Fitted value versus true value of the coefficient $\mathcal{B}_s$, using the 5-coefficient fit for various LV signals.

8.10. INGRID Results

8.10.1. INGRID FFT Results. The corrected INGRID ν_μ event rate as a function of LSP was analyzed with the method described in Section 8.6. The results of the FFT analysis can be seen in Figure 8.45 and in Table 9.3. The Fourier modes of interest to this analysis are below the 3σ detection thresholds that were set in Section 8.7.

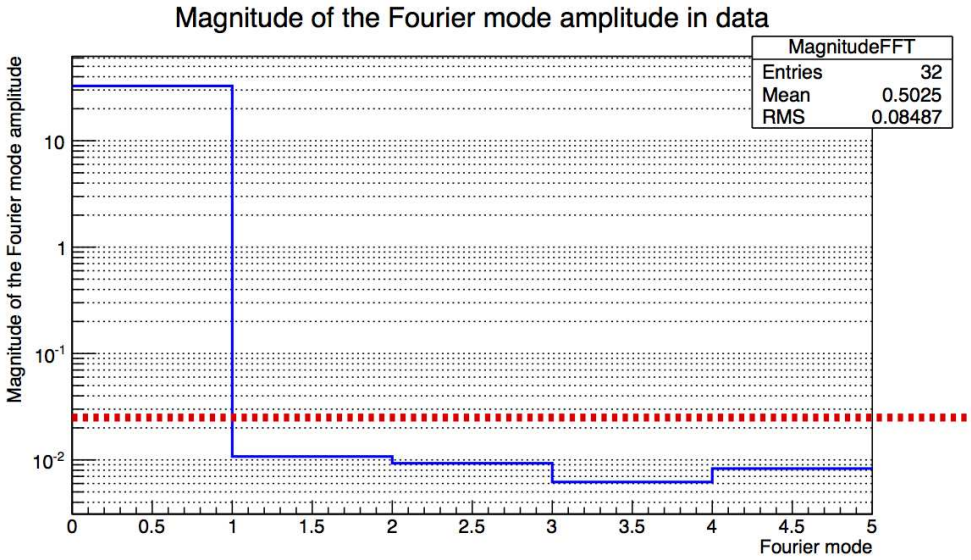

Figure 8.45. Magnitude of each Fourier mode in case of INGRID data after all corrections detailed in Section 7.3. The red horizontal line corresponds to the 3σ detection threshold.

The FFT magnitudes for the four Fourier modes are 0.01076, 0.00930, 0.00620, and 0.00893; these correspond to p-values of 0.35, 0.48, 0.69, and 0.51 respectively.

Table 8.7. FFT results.

Fourier Mode	Threshold	Magnitude	p-value
1	0.026	0.01076	0.35
2	0.026	0.00930	0.48
3	0.026	0.00620	0.69
4	0.026	0.00893	0.51

Figures 8.46 - 8.49 show where the data values fall on their parent distributions assuming no LV signal.

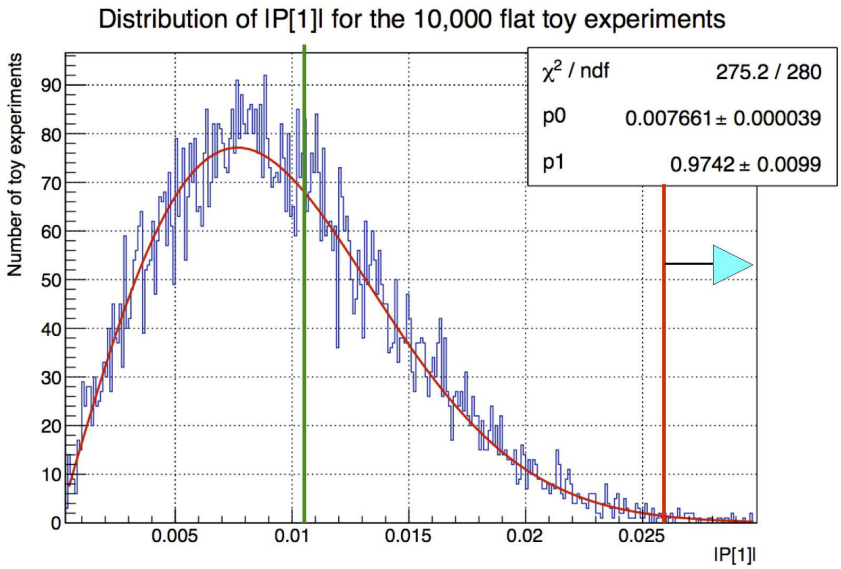

FIGURE 8.46. The parent distribution assuming no LV with the data value marked in green for F[1] in INGRID with a p-value of 0.35.

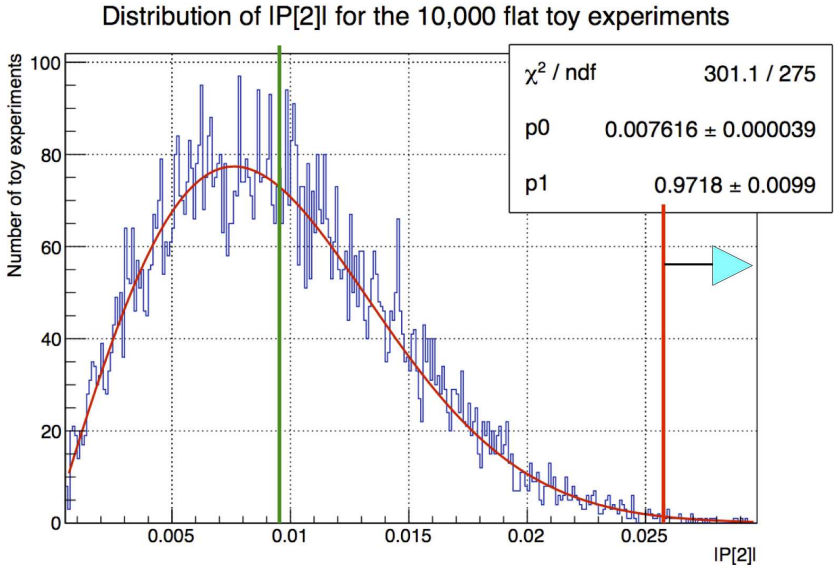

FIGURE 8.47. The parent distribution assuming no LV with the data value marked in green for F[2] in INGRID with a p-value of 0.48.

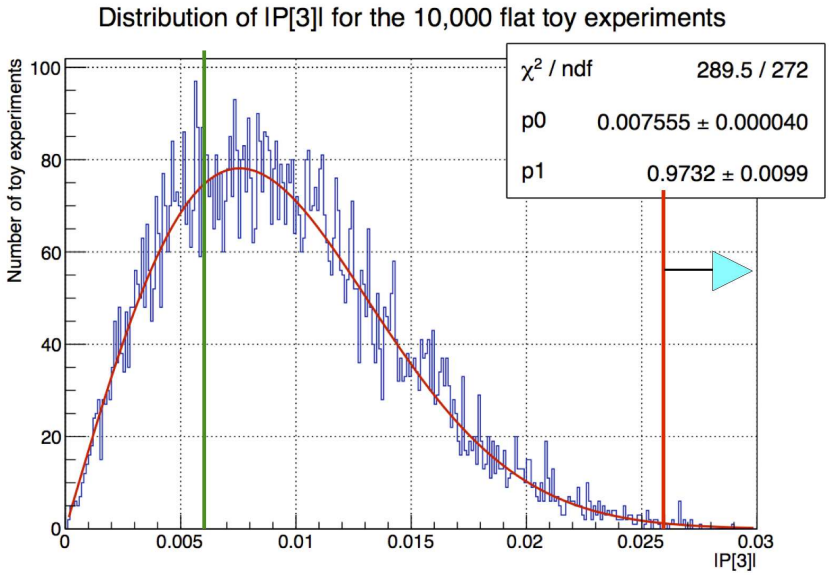

FIGURE 8.48. The parent distribution assuming no LV with the data value marked in green for F[3] in INGRID with a p-value of 0.69.

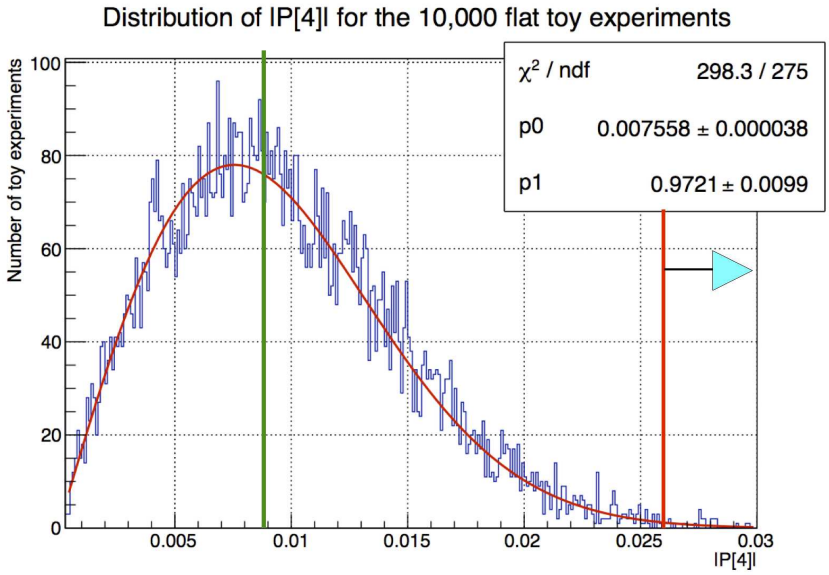

FIGURE 8.49. The parent distribution assuming no LV with the data value marked in green for F[4] in INGRID with a p-value of 0.51.

Thus, it is concluded that the INGRID data is consistent with no sidereal variation in the relevant Fourier modes using the FFT analysis method. Limits on the SME coefficients may be extracted for the INGRID sample utilizing the procedure outlined in Section 8.8. Below are the results.

TABLE 8.8. Standard Model Extension 3σ upper limits on SME coefficients related to $\nu_\mu \to \nu_e$ oscillation, for INGRID (all values given in $\times 10^{-20}$).

Coefficient	INGRID
a_L^T	-
a_L^X	4.8 GeV
a_L^Y	4.8 GeV
a_L^Z	-
c_L^{TT}	-
c_L^{TX}	0.9
c_L^{TY}	0.9
c_L^{TZ}	-
c_L^{XX}	3.8
c_L^{XY}	1.6
c_L^{XZ}	3.1
c_L^{YY}	3.8
c_L^{YZ}	3.1
c_L^{ZZ}	-

8.10.2. INGRID LIKELIHOOD FIT RESULTS. The fitter was run over the corrected INGRID data. Table 9.8 shows the best fit values for each coefficient.

TABLE 8.9. Best fit values with 1σ errors, and 2σ upper limit values on the different Standard Model Extension coefficients using the likelihood method.

	C	A_c	A_s	B_c	B_s
Best fit (10^{-20} GeV)	$-0.61^{+2.63}_{1.41}$	$0.38^{+1.83}_{-2.60}$	$-1.55^{+4.55}_{-1.44}$	$0.06^{+0.87}_{-1.00}$	$0.38^{+0.80}_{-1.57}$
2σ upper limit (10^{-20} GeV)	1.9	2.6	2.7	1.1	1.1

Below is a comparison between the INGRID and MiniBooNE Fit results.

All limits set by INGRID are consistent with zero (i.e. no LV) to 1σ. $(\mathcal{A}_c)_{ab}$ and $(\mathcal{A}_s)_{ab}$ INGRID results are compatible with MiniBooNE ones, however there is tension in the $(\mathcal{C})_{ab}$ result between the two experiments. $(\mathcal{B}_c)_{ab}$ and $(\mathcal{B}_s)_{ab}$ have now been constrained in INGRID as they previously were not.

The sensitivity of this analysis is $\sim 10^{-20}$ GeV. This shows that INGRID is able to measure possible suppressed LV effects that occur at the Planck scale. This method's sensitivity is compatible with the FFT results while accounting for the high degree of correlation

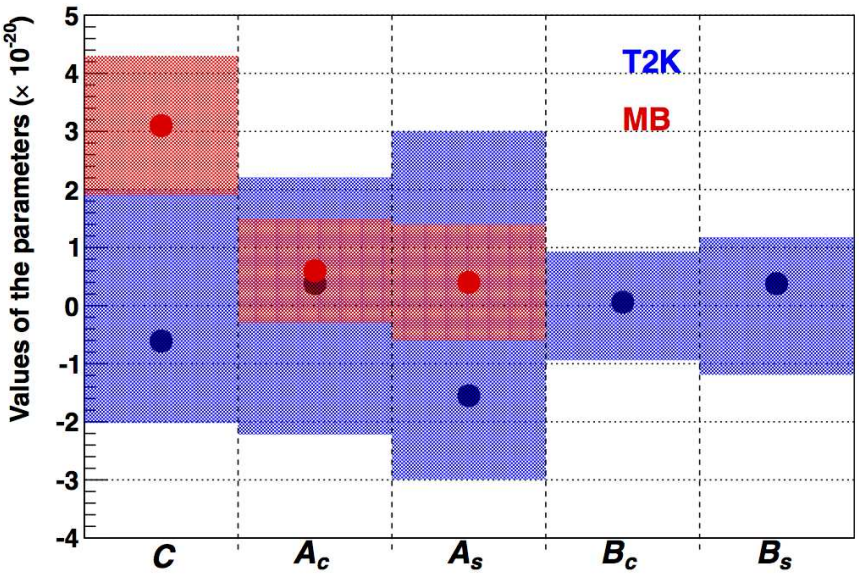

FIGURE 8.50. Comparison between the T2K (blue) and MiniBooNE (red) best fit values and 1σ limits.

between coefficients. In the T2K energy range, none of the coefficients show a deviation from the Standard Model above 1σ. Thus, the INGRID data is compatible with no Lorentz Violation in the energy range of $> 10^{-20}$ GeV.

8.11. ND280 RESULTS

8.11.1. ND280 FFT RESULTS. The corrected ND280 ν_μ event rate as a function of LSP for water-in and water-out was analyzed with the method described in Section 8.6. The results of the FFT analysis can be seen in Figure 8.51, Figure 8.52 and in Table 8.10 and Table 8.11. The Fourier modes of interest to this analysis are below the 3σ detection thresholds that were set in Section 8.7.

The FFT magnitudes for the four Fourier modes for each sample are provided below:

Figures 8.53 - 8.56 show where the data values fall on their parent distributions assuming no LV signal for the ND280 Water-in sample:

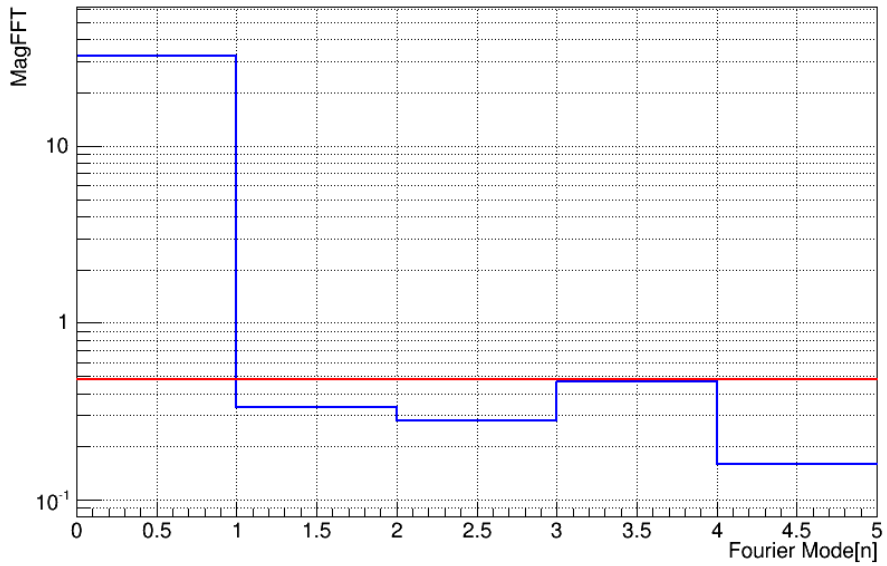

FIGURE 8.51. Magnitude of each Fourier mode in case of ND280 water-in data after all corrections detailed in Section 7.3. The red horizontal line corresponds to the 3σ detection threshold.

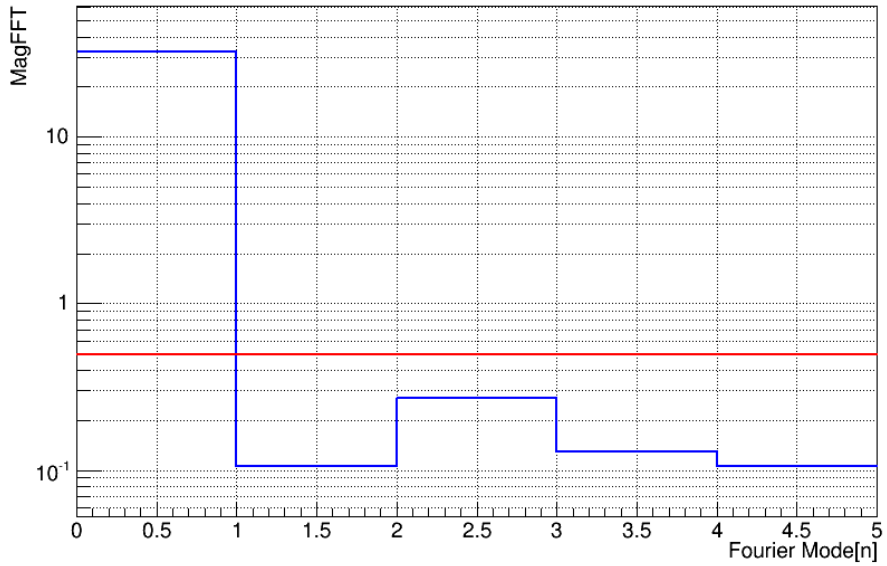

FIGURE 8.52. Magnitude of each Fourier mode in case of ND280 water-out data after all corrections detailed in Section 7.3. The red horizontal line corresponds to the 3σ detection threshold.

TABLE 8.10. FFT results for ND280 water-in.

Fourier Mode	Threshold	Magnitude	p-value
1	0.4765	0.33537	0.055
2	0.4765	0.28221	0.126
3	0.4765	0.46355	0.004
4	0.4765	0.15999	0.511

TABLE 8.11. FFT results for ND280 water-out.

Fourier Mode	Threshold	Magnitude	p-value
1	0.4947	0.10501	0.765
2	0.4947	0.26948	0.162
3	0.4947	0.12856	0.659
4	0.4947	0.10649	0.751

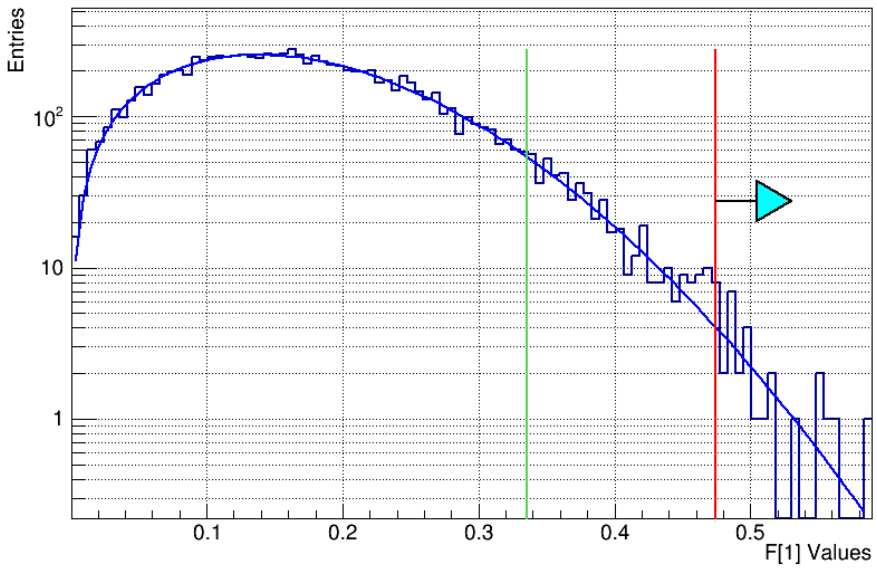

FIGURE 8.53. The parent distribution assuming no LV with the data value marked in green for F[1] in ND280 water-in.

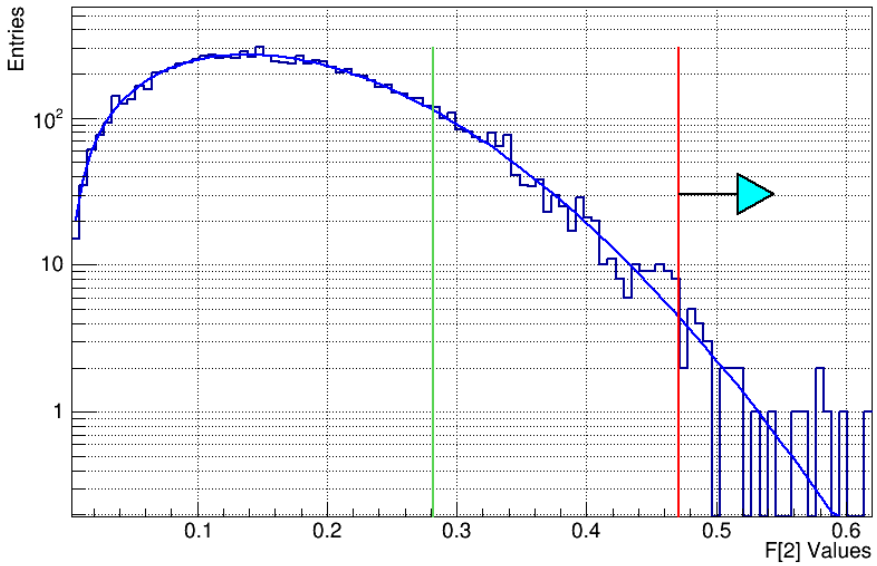

FIGURE 8.54. The parent distribution assuming no LV with the data value marked in green for F[2] in ND280 water-in.

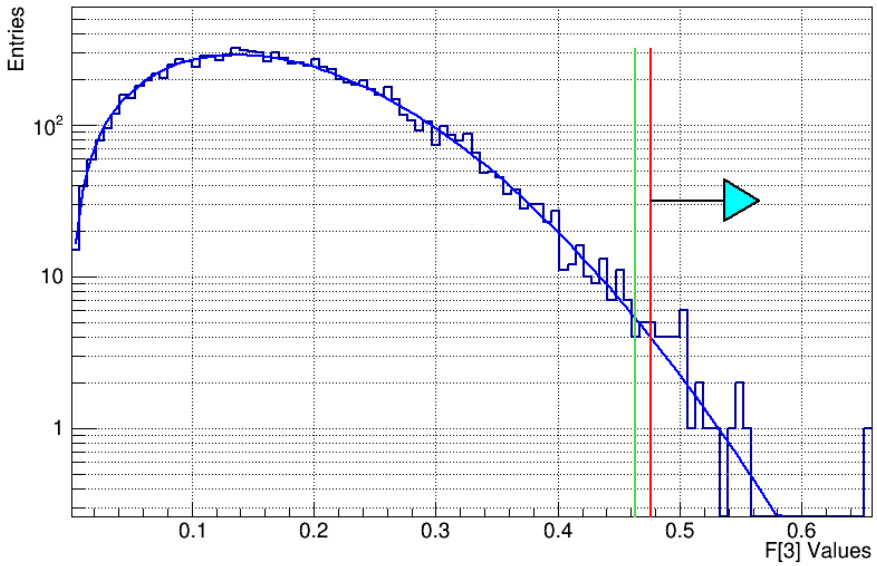

FIGURE 8.55. The parent distribution assuming no LV with the data value marked in green for F[3] in ND280 water-in.

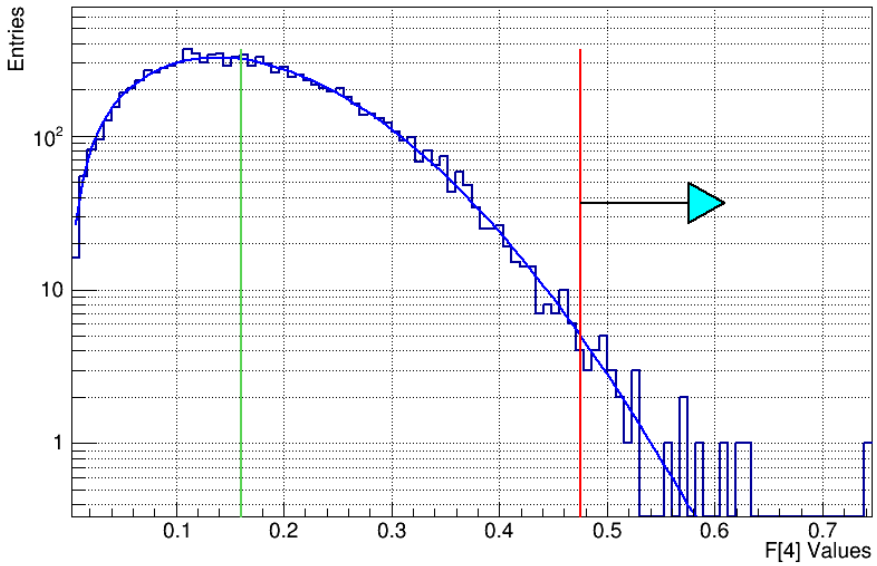

FIGURE 8.56. The parent distribution assuming no LV with the data value marked in green for F[4] in ND280 water-in.

Similarly, Figures 8.57 - 8.60 show where the data values fall on their parent distributions assuming no LV signal for the ND280 Water-out sample:

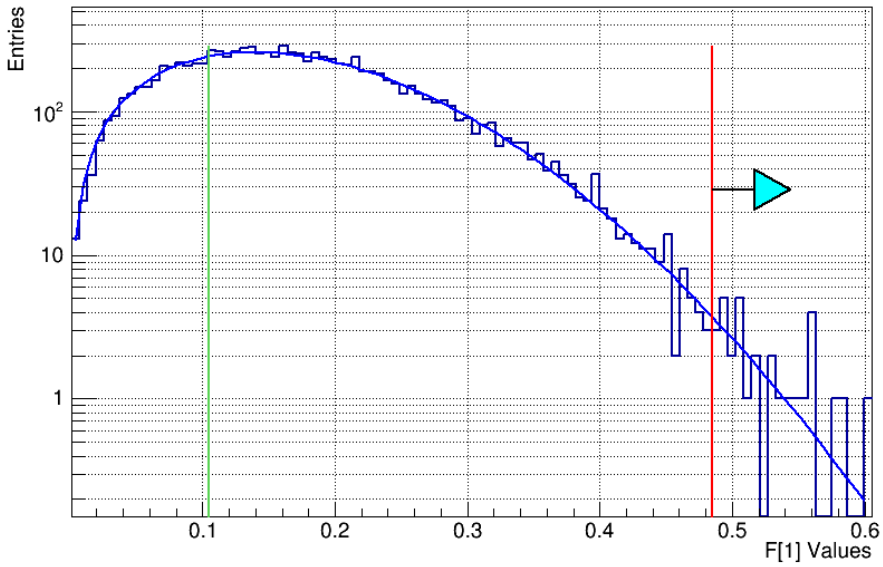

FIGURE 8.57. The parent distribution assuming no LV with the data value marked in green for F[1] in ND280 water-out.

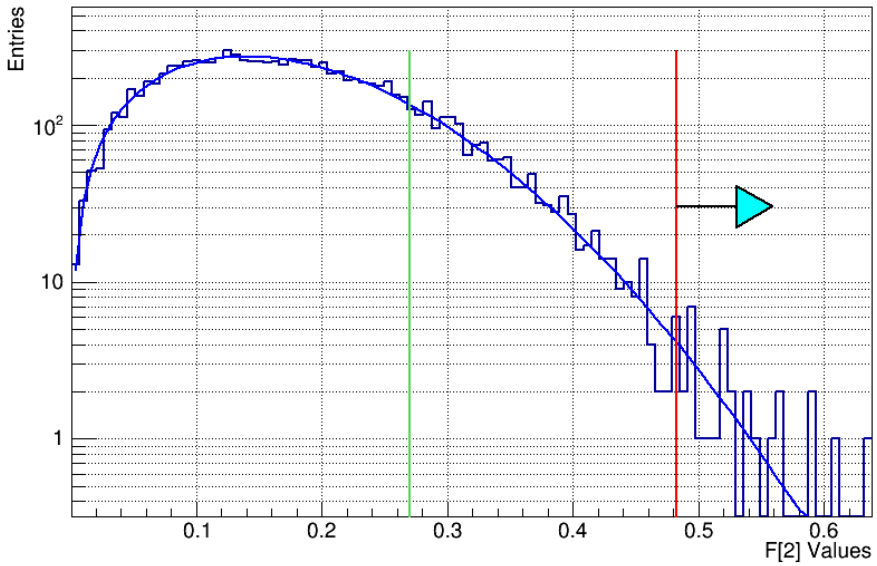

FIGURE 8.58. The parent distribution assuming no LV with the data value marked in green for F[2] in ND280 water-put.

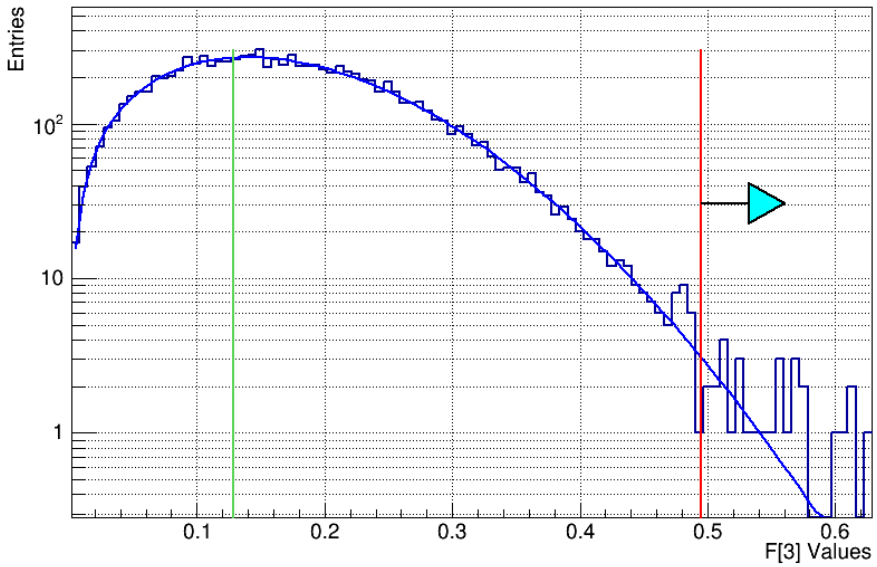

FIGURE 8.59. The parent distribution assuming no LV with the data value marked in green for F[3] in ND280 water-out.

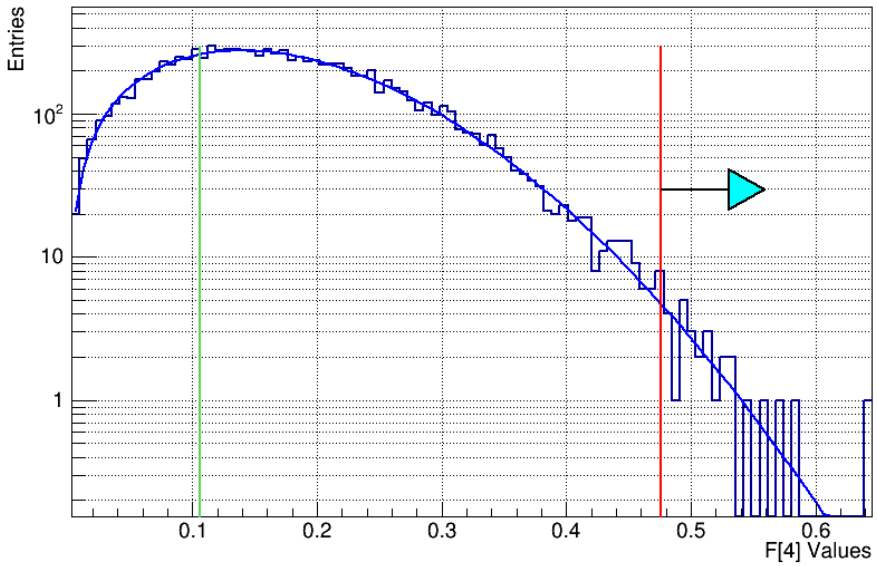

FIGURE 8.60. The parent distribution assuming no LV with the data value marked in green for F[4] in ND280 water-out.

Thus, it is concluded that the ND280 water-in and water-out data is consistent with no sidereal variation in the relevant Fourier modes using the FFT analysis method. Limits on the SME coefficients may be extracted for the ND280 samples utilizing the procedure outlined in Section 8.8. Below are the results:

TABLE 8.12. Standard Model Extension 3σ upper limits on SME coefficients related to $\nu_\mu \rightarrow \nu_e$ oscillation, for ND280 water-in and water-out (all values given in $\times 10^{-20}$).

Coefficient	ND280 Water-in	ND280 Water-out
a_L^T	-	-
a_L^X	15.7 GeV	15.4GeV
a_L^Y	16.3 GeV	17.4GeV
a_L^Z	-	-
c_L^{TT}	-	-
c_L^{TX}	13.9	10.8
c_L^{TY}	13.9	13.0
c_L^{TZ}	-	-
c_L^{XX}	54.0	57.0
c_L^{XY}	25.0	25.0
c_L^{XZ}	-	-
c_L^{YY}	54.0	57.0
c_L^{YZ}	-	-
c_L^{ZZ}	-	-

CHAPTER 9

Summary, Outlook, Conclusion

This chapter details the results of the FFT method and the binned liklihood method for each data set. All three data samples are consistent with no sidereal variation and upper bounds on the appropriate SME coefficients are extracted. Next, a summary of the entire analysis and the results is provided. A short study was performed to determine T2K's sensitivity with full statistics. Additionally, other LV searches that could be performed in T2K are detailed. Finally, a conclusion of the whole dissertation is given.

9.1. Summary

The near detectors of T2K were used to search for indications of LV in the neutrino data. The two methods utilized (FFT method and binned likelihood fit) show that all data sets used are consistent with the null hypothesis, namely, no sidereal variations.

Figure 9.1 compares the results using the FFT method of INGRID and ND280 with MiniBooNE and MINOS.

	Upper limits (10^{-20})				
SME Coeff.	MiniBoonE	MINOS	INGRID	ND280 Water-in	ND280 Water-out
a_L^T	4.2 GeV	-	-	-	-
a_L^X	6.0 GeV	2.2 GeV	4.8 GeV	15.7 GeV	15.4 GeV
a_L^Y	5.0 GeV	2.2 GeV	4.8 GeV	16.3 GeV	17.4 GeV
a_L^Z	5.6 GeV	-	-	-	-
c_L^{TT}	9.6	-	-	-	
c_L^{TX}	8.4	0.009	0.9	13.9	10.8
c_L^{TY}	6.9	0.009	0.9	13.9	13.0
c_L^{TZ}	7.8	-	-	-	-
c_L^{XX}	-	0.46	3.8	54.0	57.0
c_L^{XY}	-	0.22	1.6	25.0	25.0
c_L^{XZ}	11	0.11	3.1	-	-
c_L^{YY}	-	0.45	3.8	54.0	57.0
c_L^{YZ}	9.2	0.11	3.1	-	-
c_L^{ZZ}	34	-	-	-	-

Figure 9.1. Comparison of SME Coefficients associated with ν_e appearance INGRID and ND280 with other experiments.

Table 9.1 and Figure 9.2 compare the results of the likelihood method for INGRID and MiniBooNE:

TABLE 9.1. Best fit values with 1σ errors, and 2σ upper limit values on the different Standard Model Extension coefficients using the likelihood method.

	C	A_c	A_s	B_c	B_s
Best fit (10^{-20} GeV)	$-0.61^{+2.63}_{1.41}$	$0.38^{+1.83}_{-2.60}$	$-1.55^{+4.55}_{-1.44}$	$0.06^{+0.87}_{-1.00}$	$0.38^{+0.80}_{-1.57}$
2σ upper limit (10^{-20} GeV)	1.9	2.6	2.7	1.1	1.1

Below is a comparison between the INGRID and MiniBooNE Fit results.

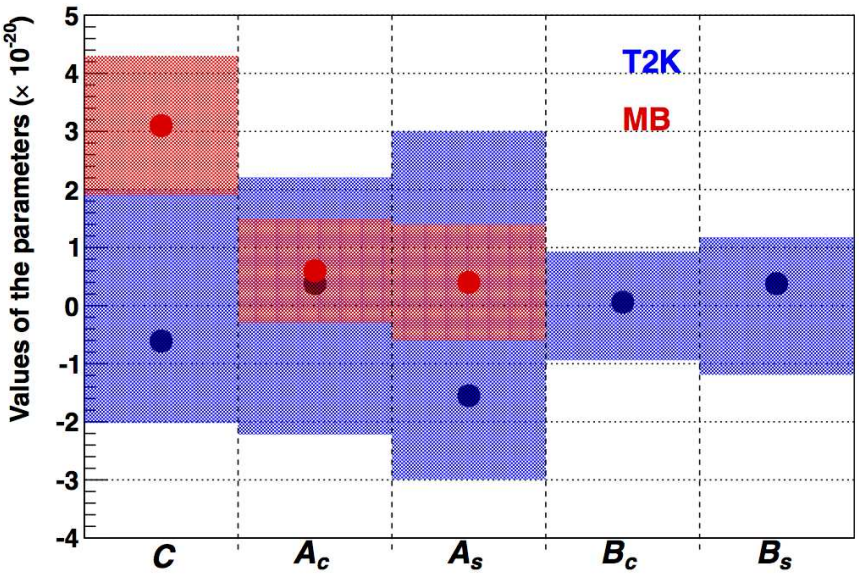

FIGURE 9.2. Comparison between the T2K (blue) and MiniBooNE (red) best fit values and 1σ limits.

9.2. Outlook for Future Searches

Future LV searches may be performed using T2K data. First, as long as T2K neutrino data continues to be taken, the analysis detailed above can be repeated for higher statistical samples. Estimated limits on the SME coefficients in INGRID using the FFT method may be

extracted assuming T2K full statistics in two different scenarios. The full statistical sample corresponds to 7.8×10^{21} POT. The two scenarios are:

(1) All POT are collected in neutrino mode

(2) 50% of data are taken in neutrino mode and the remainder in antineutrino mode

It is assumed that the systematic uncertainties are still negligible and only statistical uncertainty will dominate. The results of this study are provided in Table 9.2. The SME

TABLE 9.2. Standard Model Extension 3σ sensitivity to SME coefficients related to $\nu_\mu \rightarrow \nu_e$ oscillation, for various experiments and T2K. The T2K sensitivity is evaluated in two possible scenarios. Scenario 1: all T2K data are collected in neutrino mode; scenario 2: 50% of T2K data are collected in neutrino mode, the rest in antineutrino mode. All values given in $\times 10^{-20}$

Coefficient	MiniBooNE	Double Chooz	MINOS	T2K sc. 1	T2K sc. 2
a_L^T	4.2 GeV	-	-	-	-
a_L^X	6.0 GeV	1.6 GeV	2.2 GeV	2.5 GeV	3.0 GeV
a_L^Y	5.0 GeV	6.1 GeV	2.2 GeV	2.5 GeV	3.0 GeV
a_L^Z	5.6 GeV	-	-	-	-
c_L^{TT}	9.6	-	-	-	-
c_L^{TX}	8.4	-	0.009	0.5	0.6
c_L^{TY}	6.9	-	0.009	0.5	0.6
c_L^{TZ}	7.8	-	-	-	-
c_L^{XX}	-	-	0.46	2.0	2.3
c_L^{XY}	-	-	0.22	1.0	1.2
c_L^{XZ}	11	-	0.11	1.6	2.9
c_L^{YY}	-	-	0.45	2.0	2.3
c_L^{YZ}	9.2	-	0.11	2.0	2.3
c_L^{ZZ}	34	-	-	-	-

coefficients relevant to T2K have limits in the range $10^{-19} - 10^{-21}$. With 7.8×10^{21} POT, T2K can do better than MiniBooNE, and can reach a sensitivity that is comparable with MINOS for the a_L coefficients, but is still an order of magnitude worse for the c_L coefficients, due to the lower neutrino energy.

A reemphasis on the fact that this level of precision is still very valuable to theorists must be made. T2K probes a different direction in the Sun-centered reference frame, and thus

samples a different portion of the coefficient space. This information helps theorist improve their theories so that experimentalists may continue to test them.

Other LV analysis that may be performed are

- LV Analysis at Far Detector
- LV Neutrino Time of Flight (TOF)
- Antineutrino LV analyses

9.2.1. LV Analysis at Far Detector. The LV analysis at SK is, more or less, the same as for the near detector. The probability of oscillation at longer baselines in the SME becomes substantially different than at short baselines. For baselines which are not small compared to the neutrino oscillations lengths, 4.22 may be expanded to first order to study LV effects at long baselines. The probability of oscillation at first order for ν_μ is:

$$P_{\nu_\mu \to \nu_x} = P^{(0)}_{\nu_\mu \to \nu_x} + P^{(1)}_{\nu_\mu \to \nu_x} \tag{9.1}$$

In 9.1, $P^{(0)}_{\nu_\mu \to \nu_x}$ is the conventional three-flavor mass-driven oscillation probability and $P^{(1)}_{\nu_\mu \to \nu_x}$ is the probability of neutrino oscillation including LV effects. Using a similar spherical harmonic decomposition of the SME coefficients as was found in section 4.0.4, the LV portion of the long baseline oscillation probability is:

$$P^{(1)}_{\nu_\mu \to \nu_x} = \frac{2L}{\hbar c}\Big[(P^{(1)}_{(\mathcal{C})_{ab}})_{\mu x} + (P^{(1)}_{(\mathcal{A}_s)_{ab}})_{\mu x}\sin(\omega_\oplus T_\oplus) + (P^{(1)}_{(\mathcal{A}_c)_{ab}})_{\mu x}\cos(\omega_\oplus T_\oplus) \tag{9.2}$$

$$+ (P^{(1)}_{(\mathcal{B}_s)_{ab}})_{\mu x}\sin(2\omega_\oplus T_\oplus) + (P^{(1)}_{(\mathcal{B}_c)_{ab}})_{\mu x}\cos(2\omega_\oplus T_\oplus)\Big] \tag{9.3}$$

In 9.2, the oscillation probability depends on the *Local Sidereal Time* of the neutrino event ($T_\oplus$) and the sidereal frequency of the Earth ($\omega_\oplus$). The baseline-energy dependence goes as LE, and the expression depends on Δm^2, the conventional neutrino mixing angles, and δ_{CP}.

The combinations of the $(a_L)^{\alpha}_{ab}, (c_L)^{\alpha\beta}_{ab}$ SME coefficients $\big((P^{(1)}_{(\mathcal{C})_{ab}})_{\mu x}$, $(P^{(1)}_{(\mathcal{A}_s)_{ab}})_{\mu x}, (P^{(1)}_{(\mathcal{A}_c)_{ab}})_{\mu x}$, $(P^{(1)}_{(\mathcal{B}_s)_{ab}})_{\mu x}, (P^{(1)}_{(\mathcal{B}_c)_{ab}})_{\mu x}\big)$ are the amplitudes of the various harmonics of the Earth's sidereal frequency. The amplitudes will not be written out explicitly here, but they share a similar structure to the amplitudes that were written for the short baseline probability expression (4.38) - 4.50). These particular amplitudes for the long baseline probability expression may be found in [8].

There is an increase in sensitivity of a given coefficient at the far detector for a given statistical sample size. This is mostly due to the longer baseline. The increase in sensitivity can be estimated, for all but the (a_L) being set to zero, as:

$$\frac{(a_L)_{FD}}{(a_L)_{ND}} = \sqrt{3}\frac{(N_{ND})^{1/4}}{(N_{FD})^{1/2}} \times \frac{L_{ND}}{2L_{FD}} \times \Big[\frac{1}{2}\sin\Big(\frac{2.534\Delta m^{23} L_{FD}}{E}\Big)\Big]^{-1} \tag{9.4}$$

where:

(9.5) $(a_L)_{FD}$ is the SME coefficient at the far detector

(9.6) $(a_L)_{ND}$ is the SME coefficient at the near detetector

(9.7) (N_{ND}) is the number of neutrino events at the near detector

(9.8) (N_{FD}) is the number of neutrino events at the far detector

(9.9) L_{ND} is the baseline of the near detector

(9.10) L_{FD} is the baseline of the far detector

9.2.2. Antineutrino LV Analyses. With an antineutrino sample, a near and far detector LV analysis may be performed as described above. In the SME, the penalty for changing from neutrinos to antineutrinos is a simple change in sign of the SME coefficients.

For neutrino oscillations between flavors a and b[9]:

$$(a_L)^{\alpha}_{ab} = \mathcal{R}e(a_L)^{\alpha}_{ab} + i\mathcal{I}m(a_L)^{\alpha}_{ab} \tag{9.11}$$

$$(c_L)^{\alpha\beta}_{ab} = \mathcal{R}e(c_L)^{\alpha\beta}_{ab} + i\mathcal{I}m(c_L)^{\alpha\beta}_{ab} \tag{9.12}$$

and for antineutrinos is:

$$(a_R)^{\alpha}_{\bar{a}\bar{b}} = -\mathcal{R}e(a_L)^{\alpha}_{ab} + i\mathcal{I}m(a_L)^{\alpha}_{ab} \tag{9.13}$$

$$(c_R)^{\alpha\beta}_{\bar{a}\bar{b}} = \mathcal{R}e(c_L)^{\alpha\beta}_{ab} - i\mathcal{I}m(c_L)^{\alpha\beta}_{ab} \tag{9.14}$$

Thus, an antineutrino sample for the far and near detectors would be sensitive to the exact same SME coefficients that a neutrino sample would be.

9.2.3. LV Neutrino Time of Flight. Measurements of the neutrino time of flight may also exhibit LV effects[10]. What is even more interesting, is that the coefficients associated with LV TOF measurements have no overlap with the oscillation coefficients that have been studied in this dissertation. The limit for which this occurs is a flavor-blind limit which assumes that the mass-squared matrix and LV affect all flavors in the same way[10]. The downside to this limit, however, is that these effects are typically even more suppressed than oscillations as no interfermetry is involved.

Attention is restricted to coefficients that do not cause any neutrino mixing. By starting with a flavor-blind model [10], oscillation-free models may be constructed assuming vanishing neutrino-antineutrino mixing. Denoting the neutrino energy in oscillation-free models as E^{of}_{ν},

the dispersion relation becomes[10]:

$$E_\nu^{\rm of} = |\mathbf{p}| + \frac{|m_l|^2}{2|\mathbf{p}|} \tag{9.15}$$

$$+ \sum_{djm} |\mathbf{p}|^{d-3} \mathrm{Y}_{jm}(\hat{p}) \left[\left(a_{\rm of}^{(d)} \right)_{jm} \right] - \left(c_{\rm of}^{(d)} \right)_{jm} \Big] \tag{9.16}$$

For antineutrinos, a change in the sign of $\left(a_{\rm of}^{(d)} \right)_{jm}$ is required. The LV effects for neutrino TOF measurement can be calculated from the group velocity:

$$\nu^{\rm of} = \frac{\partial E_\nu^{\rm of}}{\partial |\mathbf{p}|} \tag{9.17}$$

and thus the group velocity becomes:

$$v^{of} = 1 - \frac{|m_l|^2}{2\mathbf{p}^2} + \sum_{djm} (d-3) |\mathbf{p}|^{d-4} e^{im\omega_\oplus T_\oplus} {}_0\mathcal{N}_{jm} \left[(a_{of}^d)_{jm} - (c_{of}^d)_{jm} \right] \tag{9.18}$$

Here, it can be seen that the group velocity depends on a conventional piece in addition to a LV piece. This LV piece consists of SME coefficients that do not enter into the LV oscillation formulas. There is, additionally, a sidereal time dependence as in the LV neutrino oscillation formulas.

9.3. Conclusion

To conclude, neutrinos are a particle with a very interesting history. From first being hypothesized in what seemed to be a dire situation, to their initial detection in 1956. Two major anomalies, the solar and atmospheric neutrino anomalies, provided a problem for physicists to solve and put the spotlight on neutrino physics. As physicist often do, over the course of several years those who pioneered in neutrino physics worked very hard to solve these anomalies. The birth of neutrino oscillations came to be through the efforts

and dedication of many physicsts. Conventionally, neutrinos oscillate to their different and non-zero masses. A parameterization of the PMNS matrix allows experiments to measure the mixing matrix parameters θ_{12}, θ_{23}, and θ_{13}. With these mixing angles all being non-zero, the holy grail of neutrino oscillation experiments is the measurement of δ_{CP}.

T2K is a neutrino oscillation experiment optimized for ν_e appearance. The main physics goals of T2K fall into conventional categories, but despite this T2K may be used for more exotic physics. Predictions in the SME range from an unconventional energy dependence to sidereal variations in the neutrino event rate. With the crisp theoretical outlines of the SME, T2K can be used to look for sidereal variations in the neutrino event rate at each of the near detectors to search for Lorentz Violation. A statistically significant signal would not only change the way we look at modern physics and its fundamental symmetries, but would also be the first signal at the the Planck energy scale. This would also be a major step towards developing more sensible theories of quantum gravity.

Utilizing T2K runs 1 - 4, a search for Lorentz violation via sidereal variations in the neutrino event rate in three of T2K's near detector samples was developed. ν_μ event selections were applied to data, sources of systematic uncertainties were found to be negligible, and two analysis methods were developed:

(1) An FFT method

(2) A binned likelihood fit

These two methods are complimentary. The likelihood fit was only applied to INGRID because of its statistical power. POT normalized neutrino event rates as a function of LSP were created and run through an FFT tool. This procedure allows for the checking of data samples with flat distributions created from removing potential LV effects in data. A

hypothesis test is performed to determine the significance of the FFT results to 3σ. The results for INGRID and ND280 are shown below:

TABLE 9.3. FFT results for INGRID.

Fourier Mode	Threshold	Magnitude	p-value
1	0.026	0.01076	0.35
2	0.026	0.00930	0.48
3	0.026	0.00620	0.69
4	0.026	0.00893	0.51

TABLE 9.4. FFT results for ND280 water-in.

Fourier Mode	Threshold	Magnitude	p-value
1	0.4765	0.33537	0.055
2	0.4765	0.28221	0.126
3	0.4765	0.46355	0.004
4	0.4765	0.15999	0.511

TABLE 9.5. FFT results for ND280 water-out.

Fourier Mode	Threshold	Magnitude	p-value
1	0.4947	0.10501	0.765
2	0.4947	0.26948	0.162
3	0.4947	0.12856	0.659
4	0.4947	0.10649	0.751

Upper limits on the SME coefficients were extracted from each sample using the method described in Section 8.8. Below are the tables of upper limits for INGRID and ND280:

Because INGRID is a much larger statistical sample than ND280, a 5-coefficient binned likelihood fit was performed to extract upper limits on the amplitudes from Equation 4.37.

TABLE 9.6. Standard Model Extension 3σ upper limits on SME coefficients related to $\nu_\mu \rightarrow \nu_e$ oscillation, for INGRID (all values given in $\times 10^{-20}$).

Coefficient	INGRID
a_L^T	-
a_L^X	4.8 GeV
a_L^Y	4.8 GeV
a_L^Z	-
c_L^{TT}	-
c_L^{TX}	0.9
c_L^{TY}	0.9
c_L^{TZ}	-
c_L^{XX}	3.8
c_L^{XY}	1.6
c_L^{XZ}	3.1
c_L^{YY}	3.8
c_L^{YZ}	3.1
c_L^{ZZ}	-

TABLE 9.7. Standard Model Extension 3σ upper limits on SME coefficients related to $\nu_\mu \rightarrow \nu_e$ oscillation, for ND280 water-in and water-out (all values given in $\times 10^{-20}$).

Coefficient	ND280 Water-in	ND280 Water-out
a_L^T	-	-
a_L^X	15.7 GeV	15.4GeV
a_L^Y	16.3 GeV	17.4GeV
a_L^Z	-	-
c_L^{TT}	-	-
c_L^{TX}	13.9	10.8
c_L^{TY}	13.9	13.0
c_L^{TZ}	-	-
c_L^{XX}	54.0	57.0
c_L^{XY}	25.0	25.0
c_L^{XZ}	-	-
c_L^{YY}	54.0	57.0
c_L^{YZ}	-	-
c_L^{ZZ}	-	-

All results for the T2K samples are consistent with no sidereal variations. Thus, T2K observes no indications of Lorentz violation in the near detector data. While this analysis has resulted in a null measurement, it must be emphasized that these limits allow theorist

TABLE 9.8. Best fit values with 1σ errors, and 2σ upper limit values on the different Standard Model Extension coefficients using the likelihood method.

	$(\mathcal{C})_{ab}$	$(\mathcal{A}_c)_{ab}$	$(\mathcal{A}_s)_{ab}$	$(\mathcal{B}_c)_{ab}$	$(\mathcal{B}_s)_{ab}$
Best fit (10^{-20} GeV)	$-0.61^{+2.63}_{1.41}$	$0.38^{+1.83}_{-2.60}$	$-1.55^{+4.55}_{-1.44}$	$0.06^{+0.87}_{-1.00}$	$0.38^{+0.80}_{-1.57}$
2σ upper limit (10^{-20} GeV)	1.9	2.6	2.7	1.1	1.1

to continue developing their theories for experimentalists to test. This is a highly important relationship in any science and shows that even null measurements can provide useful information. Future studies in T2K may be done which concern:

- LV Analysis at Far Detector
- LV Neutrino Time of Flight (TOF)
- Antineutrino LV analyses

The first and the third analyses would continue to probe the SME coefficients related to oscillations, while the second analysis would probe a completely new set of SME coefficients unrelated to oscillations. I hope, that with continued data taking, members of T2K will continue to develop these analysis methods and continue probing signals at the Planck scale.

Bibliography

[1] K. O. et al. (Particle Data Group), "The review of particle physics," *Chinese Physics C*, vol. 38, 2014.

[2] T.Kikawa, "Ingrid new analysis technique," *T2K Internal Document*, vol. 000, 2013.

[3] F. Close, *Neutrino*. Oxford University Press, 2010.

[4] S. Bilenky, "Neutrino. history of a unique particle." arXiv.org submission, 2012.

[5] A. K. D. Colladay, "Lorentz-violating extension of the standard model," *Physical Review D*, vol. 58, p. 116002, 1998.

[6] *Sensitivity of Atmospheric Neutrinos in Super-Kamiokande to Lorentz Violation*, Proceedings of the Sixth Meeting on CPT and Lorentz Symmetry (CPT13), 2013.

[7] M. M. A. Kostelecky, "Lorentz and cpt violation in neutrinos," *Physical Review D*, vol. 69, p. 016005, 2003.

[8] M. M. J. Diaz, A. Kostelecky, "Perturbative lorentz and cpt violation for neutrino and antineutrino oscillations," *Physical Review D*, vol. 80, p. 076007, 2009.

[9] M. M. A. Kostelecky, "Lorentz violation and short-baseline neutrino experiments," *Physical Review D*, vol. 70, p. 076002, 2004.

[10] M. M. A. Kostelecky, "Neutrinos with lorentz-violating operators of arbitrary dimension," *Physical Review D*, vol. 85, p. 096005, 2012.

[11] N. R. A. Kostelecky, "Data tables for lorentz and cpt violation," *Review of Modern Physics*, vol. 83, 2011.

[12] e. a. K. Abe, "The t2k experiment," *Nuclear Instruments and Methods in Physics*, vol. 69, 2011.

[13] *Overview of the T2K long baseline neutrino oscillation experiment*, Proceedings of the DPF-2009 Conference, 2009.

[14] e. a. S. Assylbekov, "The t2k nd280 off-axis pi-zero detector," *Nuclear Instrumentations and Methods in Physics*, vol. 686, 2012.

[15] e. a. N. Abgrall, "Time projection chambers for the t2k near detectors," *Nuclear Instrumentations and Methods in Physics*, vol. 000, 2010.

[16] e. a. S. Aoki, "The t2k side muon range detector (smrd)," *Nuclear Instrumentations and Methods in Physics*, vol. 698, 2013.

[17] e. T. Camplbell, "Analysis of awesome charged current inclusive events in the p0d in runs $1 + 2 + 3 + 4$," *T2K Internal Document*, vol. 000, 2010.

[18] e. a. A.Hillairet, "Nd280 reconstruction," *T2K Internal Document*, vol. 000, 2010.

[19] K.Suzuki, "Measurement of the muon beam direction and muon flux for the t2k neutrino experiment," *PTEP*, vol. 053, 2014.

[20] U. S. N. O. A. S. Time, "United states naval observatory. approximate sidereal time," *internet*, 2011.

[21] R. Dursetnfeld, "Algorithm 235: Random permutation," *Communications of the ACM 7*, vol. 7, p. 42, 1964.

[22] e. C.Bojechko, "Cc-multiple-pion ν_μ events selections in the nd280 tracker using run $1 + 2 + 3 + 4$ data," *T2K Internal Document*, 2012.

[23] e. a. W.H. Press, *Numerical Recipes in C.* Cambridge University Press, 1900.